UNIVERSIDAD NACIONAL AUTÓNOMA DE MÉXICO

POSGRADO EN CIENCIAS FÍSICAS

IMPACT OF DARK ENERGY ON THE LARGE-SCALE STRUCTURE OF THE UNIVERSE

TESIS

QUE PARA OPTAR POR EL GRADO DE:

DOCTOR EN CIENCIAS (FÍSICA)

PRESENTA

DANTE VIRGILIO GOMEZ NAVARRO

TUTORES PRINCIPALES

DR. AXEL RICARDO DE LA MACORRA PETTERSSON MORIEL (IF)

DR. ALEJANDRO AVILÉS CERVANTES (ININ-CONACYT)

MIEMBROS DEL COMITÉ TUTOR

DR. JOSÉ OCTAVIO VALENZUELA TIJERINO (IA)

DR. MYRIAM MONDRAGÓN CEBALLOS (IF)

CIUDAD UNIVERSITARIA, CDMX, DICIEMBRE 2022

UNIVERSIDAD NACIONAL

AUTÓNOMA DE MÉXICO

POSGRADO EN CIENCIAS FÍSICAS

Impact of Dark Energy on the Large-Scale Structure of the Universe

Doctoral Thesis

to obtain the degree

PhD in Physical Sciences

PRESENT

Dante Virgilio Gomez Navarro

SUPERVISORS

Dr. Axel Ricardo De la Macorra Pettersson Moriel (IF)

Dr. Alejandro Avilés Cervantes (ININ-CONACyT)

TUTOR COMMITTEE

Dr. José Octavio Valenzuela Tijerino (IA)

Dr. Myriam Mondragón Ceballos (IF)

Ciudad Universitaria, CDMX, December 2022

PUBLICATIONS

Those parts of this dissertation which have been published or in preparation for publication are as follow:

1. *Impact of cosmological signatures in two-point statistics beyond the linear regime.* D. V. Gomez-Navarro, A J Mead, A Aviles, A de la Macorra, Monthly Notices of the Royal Astronomical Society, Volume 504, Issue 3, July 2021, Pages 3284–3297, https://doi.org/10.1093/mnras/staa3393.

2. *Cosmological signatures of a rapid diluted energy density.* Axel de la Macorra, Dante V. Gomez-Navarro, Jorge Mastache, Alejandro Aviles, Mariana Jaber, and Erick Almaraz. Phys. Rev. D 104, 023529 – Published 28 July 2021.

3. *Impact of cosmological features in the halo mass function.* D. V. Gomez-Navarro, A Aviles, A de la Macorra, In preparation.

4. *Modelando el espectro de potencia de la encuesta espectroscópica de galaxias eBOSS.* D. V. Gomez-Navarro, Memorias de la Reunión Nacional Académica de Física y Matemática, Número 27, Año 27, pgs. 213-217, Agosto 2022, ISSN: 2594-1011, https://www.esfm.ipn.mx/memorias.html

5. *Estudiando las estructuras a gran escala del Universo con la teoría de perturbaciones no lineal.* D. V. Gomez-Navarro, Memorias de la Reunión Nacional Académica de Física y Matemática, Número 27, Año 27, pgs. 213-217, Agosto 2022, ISSN: 2594-1011, https://www.esfm.ipn.mx/memorias.html

RESUMEN

En este trabajo estudiamos modelos más allá de ΛCDM que se caracterizan por tener una densidad de energía extra del sector oscuro, ρ_{ex}, que se diluye rápidamente dejando un bulto en el espectro de potencia cuando se compara con ΛCDM. Los modelos considerados cuentan con una densidad de energía extra que se diluye rápidamente, más rápido que la radiación, en tres diferentes etapas de la evolución cósmica: época dominada por radiación, por materia y por la energía oscura. La transición ocurre en un factor de escala a_c con un modo correspondiente $k_c = a_c H(a_c)$ que cruzan el horizonte en ese tiempo. Al igual que las partículas fundamentales como los quarks se unen con los gluones para formar protones y neutrones, el modelo Bound Dark Energy (BDE) está basada en este tipo de transiciones de fase. La rápida dilución ρ_{ex} deja rastros en el Universo no solo en la expansión cósmica con un impacto en la escala acústica $r_s(a_c)$ y en la distancia angular $D_A(a)$, sino también en el espectro de potencia de materia y temperatura. La rápida dilución de la densidad de energía (RDED por sus siglas en inglés) genera huellas considerables que pueden ser observadas con los datos cosmológicos actuales y futuros. En particular, encontramos un bulto en el espectro de materia comparado con el modelo estándar ΛCDM. Sugerimos que las características del bulto, amplitud, ancho y la escala del bulto, es consecuencia de las propiedades físicas de la transición. Estudiamos estos efectos con teoría lineal y técnicas perturbativas, así como el impacto sobre las distancias cosmológicas.

Además, estudiamos la evolución no lineal de los efectos de tener dicha transición en el espectro de materia en el espacio real y en el espacio del corrimiento al rojo utilizando simulaciones de N-cuerpos, teoría perturbaciones no lineal y el modelo de halo. Nos concentramos en modelar la función respuesta, calculado como la razón de las estadísticas entre el modelo que contiene el bulto y otro sin él. En lugar de trabajar con un modelo teórico específico, incluimos una familia paramétrica de funciones gaussianas en un espectro de ΛCDM. Encontramos que cuando el bulto primordial es localizado en escalas lineales, las no linealidades tienden a producir un segundo bulto en escalas pequeñas. Este efecto puede ser entendido dentro del esquema de halos debido a la formación eficiente de halos. Por otra parte, estas huellas son borradas parcialmente debido al amortiguamiento a lo largo de la línea de visión producido por el movimiento no aleatorio de las galaxias en escalas pequeñas. En el espacio de configuraciones, el bulto modula la función de correlación reflejándose como oscilaciones en la respuesta como queda claro en la teoría lineal. Sin embargo, las oscilaciones son amor-

tiguadas porque los flujos de grande escala tienden a ocupar regiones más empobrecidas de partículas. Este mecanismo es explicado dentro de la teoría de perturbación lagrangiano y es bien capturado por las simulaciones.

ABSTRACT

We study the cosmological signatures of having extra energy density, ρ_{ex}, beyond the ΛCDM model that dilutes rapidly, faster than radiation, at a scale factor a_c with a corresponding mode $k_c = a_c H(a_c)$ crossing the horizon at that time. These types of models are motivated by phase transitions of the underlying elementary particles, for example the creation of protons and neutrons from almost massless quarks or the recently proposed Bound Dark Energy model. The rapidly dilution of ρ_{ex} leaves distinctive imprints in the Universe not only in the expansion history with a clear impact on the acoustic scale, $r_s(a_c)$, and angular distances, $D_A(a)$, but also in the matter and CMB power spectra. The rapidly diluted energy density ρ_{ex}, (RDED) generates characteristic signatures that can be observed with current and future precision cosmological data. In particular, we find a bump in the matter power spectrum compared to the standard ΛCDM. We identify the amplitude, width, and time scale of the bump to the physical properties of the transition. We study these effects with linear theory, standard perturbation theory, and the correlated impact on cosmological distances, allowing for independent measurements of these extensions of the standard ΛCDM model. To generate the bumps we use different models that work at early times well inside the radiation domination epoch, during matter domination or at late times when dark energy is the main component.

Some beyond ΛCDM cosmological models have dark-sector energy densities that suffer phase transitions. Fluctuations entering the horizon during such a transition can receive enhancements that ultimately show up as a distinctive bump in the power spectrum relative to a model with no phase transition. In this work, we study the non-linear evolution of such signatures in the matter power spectrum and correlation function using N-body simulations, perturbation theory and HMCODE- a halo-model based method. We focus on modelling the response, computed as the ratio of statistics between a model containing a bump and one without it, rather than in the statistics themselves. Instead of working with a specific theoretical model, we inject a parametric family of Gaussian bumps into otherwise standard ΛCDM spectra. We find that even when the primordial bump is located at linear scales, non-linearities tend to produce a second bump at smaller scales. This effect is understood within the halo model due to a more efficient halo formation. In redshift space these nonlinear signatures are partially erased because of the damping along the line-of-sight direction produced by non-coherent motions of particles at small scales. In configuration space, the bump modulates

the correlation function reflecting as oscillations in the response, as it is clear in linear Eulerian theory; however, they become damped because large scale coherent flows have some tendency to occupy regions more depleted of particles. This mechanism is explained within Lagrangian Perturbation Theory and well captured by our simulations.

Dedication

A mi madre. A mis abuelos.

MIL GRACIAS

Acknowledge

I wish to thank my supervisors, Prof. Axel de la Macorra and Alejandro Avilés, for guiding me in the preparation of this thesis. I am grateful to Prof. Mariana Vargas and Prof. Sebastien Fromenteau for the time and the efforts spent helping and hosting me during my PhD in their working group. Thank you.

Gracias a los sinodales que revisaron este trabajo y lo enriquecieron con sus comentarios: Jorge, Octavio, Alberto, Mariana y Sebastien.

A la Universidad Nacional Autónoma de México por generar las condiciones para el desarrollo de investigación científica. A CONACYT por la beca de doctorado, gracias a la cual pude realizar mis estudios.

Gracias a mi mamá con la que siempre conté. Gracias a mi familia y amigos por su apoyo para la elaboración de este trabajo.

Gracias a los que de una forma u otra me han ayudado a la realización de este trabajo.

Contents

Chapter1

OVERVIEW AND BACKGROUND

In 1998 a new epoch in the history of study of Cosmos started: the observation of redsfhift-distance relations of Supernovae type Ia showed that the Universe is currently accelerating (Riess et al., 1998; Perlmutter et al., 1999). A phenomenon that somebody did not suspect, since according to the Big Bang model at some point the objects in the sky will be approaching each other, i.e. they would be holding back due to gravitational attraction. However, studies indicate that galaxies are moving away faster and faster and the responsible, according to experts, is a new type of energy present in the vast space called dark energy. Several cosmological observations confirm that the geometry of the Observable Universe is closely flat, and that about 95% of the Universe is composed of dark energy (DE) and cold dark matter (CDM) (Planck Collaboration, 2018a).

What are the observations to infer the cosmological information given by scientists? The large-scale structure of the Universe, the Cosmic Microwave Background (CMB), Supernovae (Sn), Big-Bang Nucleosynthesis (BBN), reionization, Gravitational Waves signal, Galaxy surveys, among others, are powerful independents probes to extract cosmological information and to increase our understanding about the Universe. Our primary aim is to focus on the cosmological analysis of the Large Scale Structure (LSS) of the Universe on the high and low density regions. For this reason, in this chapter we describe briefly the equations of motion in an expanding Universe and the probes of the LSS in order to understand the accelerated expansion of the Universe, modified gravity and others cosmological paradigms.

One of the key issues in cosmology is to understand the cosmic large-scale structure. In this scenario, galaxies and galaxy clusters are merely atoms in the large Universe. To establish the dynamics of these small-scale structures, in the context of the cosmological picture, we need General Relativity and the Standard Model of particle physics. Based on these theories and the hypothesis that the measurements of the Cosmos don't depend of the point and direction where the observer is located, we can describe the history and evolution of the Universe. That is, the current standard cosmological model, which describes from primordial

big bang nucleosynthesis to today spanning a range between 10^{-3}s to 13.7 Gyrs, rely mostly on a theory of gravity, a physical theory that describes the matter contained in the Universe and their non-gravitational interactions and on symmetries hypotheses on large scales, that is, the Cosmological Principle, that stays that the Universe is homogeneous and isotropic. The mathematical representation of our Universe is known as ΛCDM model, also called the standard model of Cosmology.

1.1 The Large-Scale Distribution of Galaxies: The Cosmic Web

Large cosmological surveys have shown that galaxies and clusters of galaxies are not distributed randomly. Instead, they are coherently distributed, forming structures on large scales surrounded by elongated filaments, sheetlike walls and enormous underdense regions well-known as voids. This set of structures make up the LSS of the Universe, known as the cosmic web (Bond et al., 1996).

According to the inflation paradigm, the large scale structures were originated gravitationally from primordial fluctuations in the matter density. Due to gravitational instabilities the structures collapse and generate peculiar velocities, $\delta\mathbf{v}$, which distort the uniform Hubble expansion. In galaxy surveys it is measured the redshift, which combines Hubble's law with the radial component of these peculiar velocities $cz \approx H_0 r + \delta\mathbf{v} \cdot \hat{r}$. Later we will see these peculiar velocities leave a characteristic form in the galaxy distribution.

The structure formation has a hierarchical character: small fluctuations grow first to generate galaxies and cluster of galaxies form later via mergers or accretion. In other words, small galaxies progressively merge to form larger galaxies with time (Einasto et al., 2011).

Cosmological observables: BAO and RSD

Studying the Large-Scale Structure (LSS) is fundamental in observational cosmology since it opens the possibility of understanding the primordial fluctuations, the expansion history, the growth rate of the perturbations as well as to test the theory of General Relativity at large scales: one way to reveal them is by measuring the Universe's size at different epochs.

In order to infer statistical properties of the LSS of the Universe we can use the data provided by galaxy surveys, such as DESI (Collaboration, 2016), Euclid (Collaboration, 2013), LSST (Zhan and Tyson, 2018) and WFIRST (Spergel et al., 2015), by measuring the Baryon Acoustic Oscillations (BAO) and Redshift Space Distortions (RSD). The former is the characteristic pattern in the galaxy distribution due to coupling between baryons and photons at early times before recombination. Meanwhile, RSD is imprinted on the observed spatial distribution due to peculiar velocities of galaxies with respect to the Hubble flow. These two observables can be tested to extract cosmological information about our universe, and especially about the nature of the dark energy.

Previous studies of galaxy surveys have observed the BAO feature, which shows up as a bump in the correlation function at $\sim 100h^{-1}$Mpc separation (Eisenstein et al., 2005). Since 2005 measurements of the acoustic peak, in the matter distribution, provide a standard ruler to constrain the cosmological parameters (the angular diameter distance and the Hubble parameter) (Bassett and Hlozek, 2009), though hints had been seen in (Percival et al., 2001). The beauty of BAO is that they provide estimations for both $d_A(z)$ and $H(z)$ using linear physics phenomena, which means we can ignore nonlinear effects to a good approximation. If we take into account nonlinear effects then the Baryon Acoustic Peak in the correlation function is shifted and broaden (Bassett and Hlozek, 2009). However, in order to visualize the acoustic features in the matter correlation function, we need large survey volumes because of the BAO signal is weak and shows up on large scales, so its signal to noise is dominated by sample variance in small surveys.

The redshift-space distortions measured in galaxy redshift surveys is an attractive method in order to provide information on how structures formed in the Universe, and how gravity behaves on large scales (Percival and White, 2009; Raccanelli et al., 2013). The reason for that these distortions are a promising way to study the pattern and the evolution of the large-scale structure is due to the motion of the galaxies are induced by the structure growth. Thereby, the rate at which structures grow from the primordial fluctuations allows testing theories of gravity. In that context, the observations of the peculiar velocities of galaxies in the surveys are sensitive to the growth rate of structures, which depends on the matter density of the Universe, and its measurements allow to test General Relativity (see Peacock et al., 2001; Acquaviva et al., 2008; Gil-Marín et al., 2017).

Next-generation of galaxy surveys

We are now into the age of mapping the cosmic history and gravity with modern galaxy surveys, which will measure millions of spectra and billions of photos of them extending to $z \sim 10$. Future LSS surveys, such that the Javalambre-Physics of the Accelerated Universe Astrophysical Survey (J-PAS) (Collaboration, 2014), the Dark Energy Spectroscopic Survey (DESI) (Collaboration, 2016), the Vera Rubin Observatory (LSST) (Zhan and Tyson, 2018), Euclid (Collaboration, 2013), RST (WFIRST) (Spergel et al., 2015) and the SKA observatory (Weltman et al., 2020).

LSS surveys are important because they will be able to map the distribution of galaxy by probing its evolution from initial density field and the pattern of light distortion from weak lensing. These two probes are complemented by additional cosmological probes, such as the cross correlation between the cosmic microwave background and large-scale structures, distance luminosity via supernova, analysis of galaxy clusters and strong lensing.

For instance, the next generation ground-based CMB experiments, like CMB S-4 (Abazajian et al., 2019) and the Simons Observatory (SO) (Ade et al., 2019), will improve the measurements of microwave polarization light across most of the sky (70%) by a factor of 5, with an order of magnitude more detectors than the precursor observations, allowing us to detect

the primordial gravitational waves. CMB S-4 will include maps in nine wavelengths, meanwhile the SO in six frequencies band. Both surveys will provide a powerful complement to the LSS surveys, which will be available in other colours.

Experiments mapping the CMB will be not competitive themselves with LSS surveys. However, the combination of both surveys will be useful to break degeneracies between cosmological and modified gravity parameters (see (Martinelli and Casas, 2021)).

1.2 Perturbative and numerical methods in LSS

In order to predict properties of the Large-Scale Structure (LSS) of the Universe we need to develop analytical theories and numerical tools according to the scales that we wish to analyse. The LSS can be roughly divided in three regions: (Dodelson et al., 2016)

- **Very large scales** refer to linear scales (above $\lambda \sim 130\,h^{-1}$Mpc) $\rightarrow$ linear approximation in the density field $\delta^{(1)}(\mathbf{x},t)$.
- **Intermediate scales** are quasi-linear scales or regions where the non-linear is weak (between $20-130h^{-1}Mpc$) $\rightarrow$ extending perturbation theory beyond linear order.
- **Small scales** are scales where non-linearity emerges (below $\lambda \sim 10h^{-1}Mpc$) $\rightarrow$ described by numerical simulations or effective field theories.

In this work, the aim is to consider a perturbative theory in order to predict the properties of cosmological fluids, at late times the relevant cosmological fluid is the matter fluid, and to compare these predictions with the numerical simulations for a variety of models. These models can be of modified gravity, dark energy, as well as alternatives to dark matter.

The way to find perturbative solutions is through Standard Perturbation Theory (SPT) (Peebles, 1980) and Lagrangian Perturbation Theory (LPT) (Zel'Dovich, 1970). SPT consists of studying the evolution of the density and velocity field over a fixed space and expanding these quantities to find perturbative solutions (Bernardeau et al., 2002a). While LPT investigates the evolution of a fluid element through time, that is, the displacement vector of this fluid element is expanded (Sugiyama, 2014; Vlah et al., 2015a; Matsubara, 2015). At the weakly nonlinear scales the perturbation theory improves over linear theory. For example, LPT has been applied to the shift and broad of the peak acoustic (Tassev and Zaldarriaga, 2012), to examine higher order statistics (Tassev, 2014b), (Mohammed and Seljak, 2014) and as the base for a new version of the halo model (Seljak and Vlah, 2015). Also, in previous works have found a generalization to modify gravity models for the Lagrangian displacement field up to third order in perturbation theory (Aviles and Cervantes-Cota, 2017). However, when the nonlinear effects are important the perturbation series do not converge; the higher-order terms become larger than lower-order coefficients. Instead of expanding the perturbative terms to higher-order to avoid this inconsistency, is needed resume the series. In LPT there are several schemes to resumme the displacement vector expansion, among them Convolution

Lagrangian Perturbation Theory (CLPT) (Carlson et al., 2012a) and Lagrangian Resummation Theory (LRT) (Matsubara, 2008b,a).

As non-linear effects appear, density perturbations require numerical calculations to follow the evolution during the cosmic time. Cosmologists and astrophysicists have developed different numerical techniques to simulate the evolution of the large scale structures in the Universe. The main goal of the N-body numerical simulations is following the evolution of particles under gravity. However, to reproduce precisely the cosmic structures and dynamics of the observed galaxies in the Cosmos is essential that the N-body simulation contains billions of particles and their volumes to be colossal (Springel et al., 2005).

Finally, other approaches to follow the evolution of dark matter density perturbations beyond the linear regime are the spherical collapse (Gunn and Gott, 1972) and ellipsoidal collapse (Sheth et al., 2001), which incorporate simplified assumptions for the growth, turnaround, collapse and virialization of isolated perturbations. The evolution of dark matter density perturbations starts with the growth due to gravitational attraction. After that the perturbations decouple from the expansion of the Universe; this stage is called as the turnaround. As the perturbations grow and merge, the gravitational collapse of the dark matter overdense regions is inexorable. Finally, the formation of a gravitational self-bounded structure is established. This structure is known as the dark matter halo and the final equilibrium configuration is called virialization.

In summary, our work is focused on studying statistical properties and making predictions, using analytical theories and numerical simulations tools, of the large-scale structure of the Universe:

$$\text{Large-Scale Structure} = \begin{cases} \text{the halo model,} \\ \text{analytical theories as SPT and LPT,} \\ \text{n-body simulations.} \end{cases}$$

1.3 The expanding universe

General relativity has become the foundation for today's understanding of the cosmos. In this framework, where the gravity is a mere geometric effect based on the Equivalence Principle (EP), is possible to explain the late-time acceleration expansion of the Universe through the cosmological constant.

In General Relativity the curvature provide information about the dynamic of the energy distribution. The equations that set up the equivalence between matter and curvature is given by

$$R_{\mu\nu} - \frac{1}{2} g_{\mu\nu} R = 8\pi G T_{\mu\nu}, \tag{1.1}$$

where $R_{\mu\nu}$ is the curvature tensor, $g_{\mu\nu}$ is the metric tensor, R is the scalar curvature, $T_{\mu\nu}$ is the tensor of momentum-energy and G is the gravitational constant. Moreover, to describe

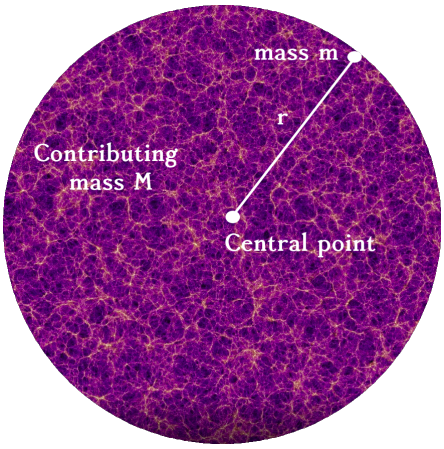

Figure 1.1: General relativity is an adequate description of gravity as long as, roughly speaking, the mass M of the system is approximately equal to the size, $R \sim 1$. Adapted image from the Millennium Simulation (obtained from https://wwwmpa.mpa-garching.mpg.de/galform/millennium/).

the content of matter-energy in the Universe, we can identify the tensor of momentum-energy as a fluid perfect

$$T_{\mu\nu} = (\rho + P)u_\mu u_\nu + P g_{\mu\nu}, \tag{1.2}$$

with ρ, P and u^μ is the energy density, pressure and four-vector of fluid, respectively. In Comoving coordinates $u^\mu = (-1,0,0,0)$.

The test of GR have been performed within and without the Solar System (Will, 2014; Ishak, 2018; Psaltis, 2019). The former have been reached high precision and tested during the last century. The latter have been tested recently and represent a probe fundamental for a underlying theory of gravity. For instance, the measurements at large scales such as the strongest gravitational fields of neutron stars and stellar-mass black holes (Psaltis, 2008; Berti et al., 2015), the weakest gravitational fields probed by cosmological phenomena (Koyama, 2016) and gravitational waves (Mukherjee et al., 2021) represent promise probes to yield constraints on modified gravity parameters at cosmological scales.

We can also use Newtonian Theory of gravity to study the large-scale structure of the Universe as we will see later. So when can we use General Relativity? When can we use the Newtonian theory? To inquire it we consider a spherically-symmetric distribution of matter which represent the cosmological volume. We calculate the ratio between the energy due to Gravitational potential energy derived from Newtonian theory of gravity and the famous relationship for energy

$$E = mc^2. \tag{1.3}$$

The particle of mass m, or a galaxy from cosmological picture, at radius r only feels gravitational attraction from an object of mass M. The forced exerted means there is a gravitational

potential energy (see Figure (1.1))

$$V = -\frac{GMm}{r}, \tag{1.4}$$

where r is the distance between the objects and G is the gravitational constant. From the viewpoint of General Relativity, the energy associated with the particle of mass m can be obtained from Eq. (1.3). Hence, the ratio of energies is written as

$$R = \frac{|V|}{E} = \frac{GM}{rc^2}. \tag{1.5}$$

If $V << E$ (or $R << 1$), so Newtonian theory is an adequate description of gravity. In other words, if the mass M of a system is small compared to the size R, from view point of geometrized units (Schutz, 2009), we can use the Newtonian scheme. In geometrized units $G = c = 1$ and for this reason we can compare the mass M of the system with the size r. When $V \approx E$ (or $R \approx 1$) we must replace Newtonian theory with General Relativity. We examine some systems to explore when we can use GR. Each galaxy contain some 10^{11} stars in a radius of about $15kpc$. In this case $M \approx 2 \times 10^{41} kg$ and $R \approx 45 \times 10^{19} m$. For this system, $R \sim 10^{-6}$, similar to that for the Sun itself. We use $G = 6.67 \times 10^{-11} m^3 s^{-2} kg^{-1}$, $1pc = 3 \times 10^{16} m$. To study the cosmological volume, the observable Universe, we consider the density of mass-energy is given by $\rho \sim 10^{-26} kgm^{-3}$ and $R \sim 10Gpc$. The mass can be obtained by $M = 4\pi\rho R^3/3$, where ρ is the density. In this case, we obtain $R \sim 1$. For this reason, we study the dynamics of the Universe via General Relativity. On large scales, General Relativity is a essential framework to understand the Universe.

1.4 The standard model of cosmology

Our Universe possesses two important properties, homogeneity and isotropic on large scales. It is the called cosmological principle. These assumptions suggest that the law of physics have the same form in all points and all directions that we observe. Finally, with the term large scale we refer on scales about $100h^{-1}Mpc$ ($1Mpc = 10^6 pc$, $1pc$=$3 \times 10^{16} m$), which is the distance at which the cosmological principle is a good approximation (Hunt and Sarkar, 2009). Just to give you a sense scale, the distance to the next closest galaxy, Andromeda, is about $765kpc$.

Under the cosmological principle we write the metric for a space-time that describes homogeneity and isotropic

$$ds^2 = -dt^2 + a(t)^2 \left[\frac{dr^2}{1 - Kr^2} + r^2 d\Omega^2 \right], \tag{1.6}$$

where K is the curvature, which for a homogeneity and isotropic Universe can be take values $(+1, -1, 0)$, $d\Omega^2 = d\theta^2 + sen^2\theta d\phi^2$ and $a(t)$ is the scale factor. The variable t represent the

proper cosmological time and it defines the time measure by an observer that see the expanding Universe to be homogeneous and isotropic. (r,θ,ϕ) are called comoving coordinates, while the scale factor $a(t)$ measures the expansion or contraction of spatial dimensions.

The metric of Eq. (1.6) is called the Friedmann–Lemaitre-Robertson-Walker metric (FLRW). The combination of ideas therefore about expanding universes along with the geometry of homogeneous and isotropic spacetime produce the so-called FLRW models, which describe the background cosmological evolution. Our Universe can have three geometries of space, spherical ($K=1$), flat ($K=0$) and hyperbolic ($K=-1$).

To obtain the motion equations we shall consider the energy-momentum tensor to be perfect fluid and introduce the FLRW metric into the Einstein Field equations. The dynamic equations one obtains are given by

$$\left(\frac{\dot{a}}{a}\right)^2 = \frac{8\pi G}{3}\rho - \frac{K}{a^2}, \tag{1.7}$$

$$\dot{\rho} + 3\frac{\dot{a}}{a}(\rho + p) = 0, \tag{1.8}$$

$$\frac{\ddot{a}}{a} = -\frac{4\pi G}{3}(\rho + 3p). \tag{1.9}$$

The Eqs. (1.7-1.9) describe the dynamic of a homogeneous, isotropic Universe With this, we can obtain the age of the Universe and the luminosity distance of distant objects in an expanding Universe. The Eq. (1.7) indicate the evolution of scale factor in terms of the total energy density for different geometries. It is called the Friedmann's equation. The Eq. (1.8) suggest the evolution of energy density and is well-known as continuity equation. Finally, the Eq. (1.9) show if the Universe undergo an accelerated expansion. These set of equations really represent two independent equations with three variables a, ρ and p.

We then need an addition equation which relate the density energy and pressure. This expression is called state equation and is given by

$$P = \omega(\rho)\rho. \tag{1.10}$$

ω is a constant for different components in the Universe. For instance, the values for different components of the Universe are shown the following

- $\omega = \frac{1}{3}$ Photons or other relativistic particles.
- $\omega = 0$ Massive non-relativistic particles.
- $0 < \omega < \frac{1}{3}$ Mildly relativistic matter.
- $\omega = -1$ Cosmological constant.
- $\omega < -\frac{1}{3}$ Dark energy.

There is also others models of dark energy whose state equation is varying as a function of time, called dynamical dark energy. The density for the dynamical dark energy with ω_{de} is given by

$$\rho_{de} = \rho_{0,de} \exp\left(-3\int_1^a (1+\omega_{de}(a'))d\ln a'\right). \tag{1.11}$$

In these models, ω_{de} can be allowed to vary in redshift (or scale factor), for example, it take the form $\omega(a) = \omega_0 + \omega_q(1-a)$ known as CPL parametrization ((Chevallier and Polarski, 2001; Linder, 2003). There is a vast set of parametrizations for ω introduced in order to fit other dark energy or modified gravity models.

If we define $H = \dot{a}/a$ as the Hubble parameter, we can written the Eq. (1.7) as

$$H(t)^2 = \frac{8\pi G}{3}\rho(t) - \frac{K}{a(t)^2}. \tag{1.12}$$

This allows us to define a cosmological parameter, the Hubble constant as $H_0 = H(t_0)$ where t_0 is the present time. The cosmological redshift is related to the scale factor by $1+z = a_0/a$, where a_0 is the scale factor in the present time.

For a flat Universe ($K = 0$), the Friedmann equation takes the form

$$H(t)^2 = \frac{8\pi G}{3}\rho(t). \tag{1.13}$$

Therefore, there is a critical value for the energy density expressed ad

$$\rho_c(t) = \frac{3}{8\pi G}H(t)^2. \tag{1.14}$$

The critical density of the Universe evaluated today $\rho_{c,0}$ is useful to describe the energy in the Cosmos as measured from observations. This quantity will serve as a reference density. The value numerical is:

$$\rho_{c,0} = \frac{3H_0^2}{8\pi G} = 1.9\times10^{-29}h^2 \text{grams cm}^{-3} = 2.8\times10^{11}h^2 \text{M}_\odot\text{Mpc}^{-3}, \tag{1.15}$$

where the last line is given in solar masses, $M_\odot$, per megaparsec cubed (Ishak, 2018).

If we take account the Eq. (1.14), the Friedmann's equation reads

$$\frac{K}{a(t)^2H(t)^2} = \frac{\rho(t)}{\rho_c(t)} - 1. \tag{1.16}$$

The Eq. (1.16) describes three possible geometries. We can have flat ($K = 0$), open ($K = -1$) and closed ($K = 1$) Universes. These geometries depend if the critical density is more, less or equal to today density of the Universe:

- If $\rho(t) > \rho_c(t)$ Positively curved Universe.

- If $\rho(t) < \rho_c(t)$ Negatively curved Universe.
- If $\rho(t) = \rho_c(t)$ Flat Universe.

The critical density is defined because it establish the limit between having a universe that expands forever and a universe that expand to value certain and after it contract. Other quantity that we can define is the well-known density parameter Ω

$$\Omega(t) = \frac{\rho(t)}{\rho_c(t)}. \tag{1.17}$$

We can write the Eq. (1.16) in terms of density parameter

$$1 - \Omega(t) = -\frac{K}{a(t)^2 H(t)^2}. \tag{1.18}$$

In terms of today values, $a(t = t_0) = 1$, $H(t = t_0) = H_0$, $\Omega(t = t_0) = \Omega_0$, where t_0 is the present time. Hence, nowadays the curvature can be expressed as

$$K = H_0^2(\Omega_0 - 1). \tag{1.19}$$

Studies have showed that the curvature density $\Omega_K^{(0)}$ is approximately zero, with $-0.005 < \Omega_K^{(0)} < 0.005$ (Planck Collaboration et al., 2016) and combined with BAO $\Omega_K = 0.0007 \pm 0.0019$ (Planck Collaboration, 2018a). However, other geometries are not disfavored by observational data: CMB data alone favours a non-zero value $\Omega_K = -0.044^{+0.019}_{-0.014}$ (Planck Collaboration, 2018a). A Planck research team found that data from the recent Planck Legacy 2018 point instead to a spherical universe with 99.985% probability, although others scientists have showed that this result is most likely a statistical fluctuation (Di Valentino et al., 2019).

We have seen that GR provide a framework to the current standard model of cosmology predicting exact solutions with expanding or contracting universes and allowing the background cosmological evolution. The combination of FLRW models along with a cosmological perturbation theory is fundamental in order to study the cosmic structure evolution from the very early times ($\ll 10^{-6}$s) to the late stages of the Cosmos, some 13.8Gyr later. In sections 2.2 2.3 we will see two perturbation schemes.

1.4.1 Dark Sector

According to the standard model of cosmology, often called ΛCDM, the most quantity of the Universe's energy density is unknown. This non-luminous mass is known as dark sector of the Universe, which is composed of dark energy (Λ, 70%) and cold dark matter (CDM, 25%). Under the label "dark energy" and "dark matter" we include a variety of hypothesis. Although there have been discarded models, the nature of the dark sector is still a mystery (Arun et al., 2017). In this section we describe briefly both components.

Dark Energy

One of the more intriguing questions in modern cosmology is the origin of the acceleration of the Universe, which started when $z \approx 0.6$, i.e. approximately when the Universe was half of its present size. Scientists have proposed a new type of fluid to explain the cosmic acceleration and there is a vast set of candidates for dark energy as a fluid (see Huterer and Shafer (2017)). Today dark energy is the dominant energy component. However, the energy density fraction of dark energy decreases as it increases z. For instance, the dark energy density fraction at $z = 2.5$ was ($> 5\%$) of the total energy density (which is about the baryon energy density today). Cosmological constant's energy density fraction at the epoch of cosmic microwave background last scattering, at $z \approx 1090$, is expected to constitute 10^{-9} of the total energy density. In other dark energy models the contribution could be $10^{-3}-$six orders of magnitude difference (Brax, 2017; Linder, 2021; Frusciante and Perenon, 2020).

Between the observational evidences of dark energy are: type Ia supernovae (SNe Ia), the baryon acoustic oscillations (BAO), the cosmic microwave background (CMB), weak lensing, and galaxy clusters. There are others probes of dark energy like RSD, Cosmic Voids, Standard sirens, etc. (see Table 1 of Huterer and Shafer (2017)).

The measurements of growth rate studying RSD is an important cosmological probe of dark energy since the growth rate reflects a competition between the the gravitational attractive force and the cosmic expansion (Linder, 2019)

Otherwise, dark energy sensitivity of the cosmological data comes from three factors (Yu et al., 2021):

- geometry - distance as a function of redshift,
- growth of structures - the amplitude of the power spectrum as a function of redshift, and
- shape - the power spectrum as a function of wavenumber.

Separately measuring the three primary relationships is an excellent way, not only to measure the dark energy parameters, but also to distinguish dark energy models.

Dark energy has come to dominate the energy budget of the Universe recently ($z \leq 0.5$). The data allows a $\sim 1\%$ contribution by dark energy at early times (The Atacama Cosmology Telescope Collaboration, 2021). For this reason, scientists have proposed early dark energy models where a new field is introduced that acts to briefly accelerate cosmic expansion prior to recombination. In this thesis we work with a EDE-like called Bound Dark Energy model.

Dark Matter

Dark matter, on the other hand, is responsible of clustering of galaxies. In the current model of galaxy formation, we expect every galaxy embedded in a cold dark matter (CDM) halo. According to mathematical model, about 25% of the energy budget of the Universe is dark

matter. There are evidences for existence and nature of this substance at different scales. For instance, the most mature probes of dark matter come from galaxies (galaxy cluster velocity dispersion) (Persic et al., 1996), galaxy clusters (X-ray measurements from galaxy clusters), large-scale structure distributions, anisotropies in the cosmic microwave background, and gravitational lensing studies.

The nature of dark matter is vast and we can to distinguish as the warm vs cold classification. For instance, warm dark matter (WDM) can potentially explain small-scale observations, whereas cold dark matter is a successful model that explains the observed structures well above $\sim$ 1Mpc. By comparing the small-scale observations thus provides a powerful way to distinguish between WDM and CDM models (Dekker et al., 2021).

However, there is population of galaxies, such that ultra-diffuse galaxies (UDGs), that can be explained almost entirely by the contribution of the baryons alone, with little room for dark matter (Piña et al., 2021).

In the next chapter we shall describe the matter density fields via numerical and technical tools. Otherwise, we are going to see in chapter 3 a new scalar field to describe the nature of dark energy.

Chapter2

MODELLING THE LARGE SCALES STRUCTURES OF THE UNIVERSE

The Large-Scale Structure (LSS) is often described by matter density and velocity fields, or by their statistical properties through the matter power spectrum or the two-point correlation function. For this reason, in this chapter, we describe these concepts and techniques used for the study of the large scales. Also, we develop two analytic techniques: the Standard and Lagrangian perturbative schemes. These theories are based on expanding scalar or vector fields as the matter density field, the divergence of the velocity field and the Displacement vector field. Both SPT and LPT are good approximations in the weakly non-linear range because the fluctuations are treated small ($\delta \ll 1$, $\theta \ll 1$ or $\Psi \ll 1$). However, in the strongly nonlinear regime these analytic methods become inadequate.

2.1 Statistical physics for Cosmic Structures

We need statistical methods to describe the galaxies distribution on a wide range of scales, for example the correlation function and power spectrum. Therefore, in this section, we examine some basic statistical concepts and their properties with the major aim of studying the clustering of galaxies.

For this reason we firstly represent the mass distribution through of a homogeneous background $\bar{\rho}(t)$ plus a perturbative term $\delta(\mathbf{x},t)$ which represent the fluctuations

$$\rho(\mathbf{x},t) = \bar{\rho}(t)(1+\delta(\mathbf{x},t)). \tag{2.1}$$

That is, the fluctuation density field is given by

$$\delta(\mathbf{x},t) = \frac{\rho(\mathbf{x},t) - \bar{\rho}(t)}{\bar{\rho}(t)}. \tag{2.2}$$

Equation (2.2) indicates the difference of the matter density at point $\mathbf{x}$ with respect to the average density of the Universe $\bar{\rho}(t)$, and so $\delta(\mathbf{x},t)$ is also known as contrast density. Considering the density contrast, we can define others quantities: the correlation functions and power spectrum. Note that mass field $\rho(\mathbf{x},t)$ is a non-negative quantity; therefore $\delta(\mathbf{x},t) \geq -1$ at any $\mathbf{x}$. For example, the voids are underdense regions, i.e. $\rho(\mathbf{x},t) < \bar{\rho}(t)$. In this case the density contrast is $\delta(\mathbf{x},t) < 0$. To structures as galaxies and cluster of galaxies $\delta(\mathbf{x},t)$ is larger than 1. While, the linear structures, as supercluster of galaxies, are characterized by $\delta(\mathbf{x},t) \ll 1$.

2.1.1 The two-point correlation function

One important question in cosmology is the distribution of galaxies in the Universe. To study this, cosmologists use the correlation function to explain the scale characteristic of found another galaxy given a random galaxy in a point. In other words, the correlation function is a measure of the degree of clustering of galaxies expressing the excess of probability of finding two galaxies separated by a distance r relative to a uniform random distribution. While the power spectrum answers the question "How much of the fluctuations of density field is at a wavenumber k?"

We know that the formation of large scale structure in the universe were originated by small fluctuations in matter density and velocity fields in the primordial universe. The fluctuations of fields were amplified by gravity (Guth et al., 2014). The amplitude of fluctuations on different length scales or equivalently on different mass scales is described by the power spectrum (Baugh, 2000). In view of these considerations, we describe the two point correlation function, the power spectrum and higher-order correlations.

The two-point correlation function is defined in configuration space as the joint ensemble average of density at two different locations,

$$\xi(r) = \langle \delta(\mathbf{r})\delta(\mathbf{x}+\mathbf{r}) \rangle, \tag{2.3}$$

which depends only on the norm of $\mathbf{r}$ due to statistical homogeneity and isotropic.

To calculate the power spectrum of the fluctuations we write the density contrast $\delta(\mathbf{x})$ in terms of its Fourier components,

$$\delta(\mathbf{x}) = \int \frac{d^3k}{(2\pi)^3} e^{i\mathbf{k}\cdot\mathbf{x}} \delta(\mathbf{k}). \tag{2.4}$$

When one considers a Gaussian field, the power spectrum becomes fruitful. Any ensemble average of product of variables can then obtained by product of ensemble averages of pairs (Bernardeau et al., 2002a) (Baugh, 2000). We write this property as follow

$$\langle \delta(\mathbf{k}_1)...\delta(\mathbf{k}_{2p+1}) \rangle = 0, \tag{2.5}$$

$$\langle \delta(\mathbf{k}_1)...\delta(\mathbf{k}_{2p})\rangle = \sum_{\text{all pair associations}} \prod_{\text{p pairs (i,j)}} \langle \delta(\mathbf{k}_i)\delta(\mathbf{k}_j)\rangle. \tag{2.6}$$

The Eqs. (2.5-2.6) are known as the Wick's or Isserlis's theorem (Weinberg, 2008). As first approximation, the initial density field can be considered as a Gaussian random field. However, the simplest inflation model predicts some small deviation from Gaussianity (Guth, 1981; Falk et al., 1993; Maldacena, 2003).

Otherwise, the non-Gaussian aspects of random fields, which are present everywhere in cosmology, can be characterized by higher order spatial statistics as the three-point correlation function or its counterpart in Fourier space, the bispectrum. These ideas can be applied to all cosmological random fields as Lyman-α forests, the large-scale structure, or the Cosmic Microwave Background (CMB).

The concept of the two-point correlation function may be extended to higher-order correlations, for example to third-order. So in place of Eq. (2.3) one writes

$$\zeta(r_{12}, r_{23}, r_{31}) = \langle \delta(\mathbf{r}_1)\delta(\mathbf{r}_2)\delta(\mathbf{r}_3)\rangle, \tag{2.7}$$

which depends only on the norms of $r_{12} = |\mathbf{r}_1 - \mathbf{r}_2|$, $r_{23} = |\mathbf{r}_2 - \mathbf{r}_3|$ and $r_{31} = |\mathbf{r}_3 - \mathbf{r}_1|$ due to homogeneity and isotropy. The Eq. (2.7) represents the three-point correlation function (3PCF). The physical interpretation of the 3PCF is that it measures the probability of finding three objects in a particular triangle configuration compared to a random sample.

On the other hand, the bispectrum B, the Fourier transform of the 3PCF, is given by

$$\langle \delta(\mathbf{k}_1)\delta(\mathbf{k}_2)\delta(\mathbf{k}_3)\rangle = (2\pi)^3 \delta_D(\mathbf{k}_1 + \mathbf{k}_2 + \mathbf{k}_3) B(k_1, k_2, k_3). \tag{2.8}$$

As the power spectrum, the real space bispectrum does not depend on the direction of the k-vectors. The $\mathbf{k}$-vector configurations form closed triangles because of homogeneity. For Gaussian initial conditions the bispectrum is zero since the n-point correlation function of a Gaussian field is always zero when n is an odd number. Also, as long as the k-modes evolve independently, i.e. in linear theory, the bispectrum is zero in the absence of primordial non-gaussianities, as can be seen from Wick's theorem. However, when the k-modes are coupled, i.e. non-linearities start to play an important role, the bispectrum becomes important and is non-zero. Hence, one can extract information about how non-linear processes influence the evolution of dark matter distribution by measuring the bispectrum. To obtain this information is complicated because the effects of gravity can not be isolated, i.e. the cosmological parameters are degenerate.

The forthcoming galaxy surveys will increase the signal-to-noise of the data and the uncertainties around the ΛCDM model will be reduced. That is, higher precision data will allow to use not only the two-point correlation function, but also higher-order statistics, in order to constrain and improve our theories and models. For this, we need better analytical models to describe the bispectrum and the 3-PCF at non-linear scales.

2.1.2 The power spectrum via N-BODYKIT package

In this section we describe how to compute the power spectrum, from a data set either simulated or real, via N-BODYKIT package [1]of (Hand et al., 2018). Physically, the power spectrum is estimated as follows: First, generate data on a mesh. Second, Fast Fourier Transform (FFT) the mesh to Fourier space. Third, generate the 3D power spectrum on the mesh. Finally, perform the binning in the given basis. We now briefly describe these four steps.

The simulation box is discretized on to a mesh to compute the power spectrum. To generate data on a mesh we use the *to_mesh()* function in N-BODYKIT. This function transforms a discrete catalog of particles on to a mesh. The desired number of cells per mesh side is specified by the *Nmesh* parameter. The discrete particles on to a regular mesh is interpolated choosing a interpolation kernel, also known as $W(\mathbf{k})$ Window kernel, which determines which cells an object will contribute to on the mesh. In other words, one should first choose a mass assignment function, which assign a shape to each particle defined by a function $S(\mathbf{x})$. In the simplest procedure, known as the Nearest Grid Point (NGP) assignment scheme, a particle only contributes to the one cell that is closest to its position. We use two more general schemes to calculate the mesh, known as Cloud in Cell (CIC) and Triangular Shape Cloud (TSC) schemes, representing the two and third order piecewise polynomial function, respectively. For these methods, we have

$$W(\mathbf{k}) = \left[\frac{\sin\left(\frac{\pi k_1}{2k_N}\right) \sin\left(\frac{\pi k_2}{2k_N}\right) \sin\left(\frac{\pi k_3}{2k_N}\right)}{\left(\frac{\pi k_1}{2k_N}\right)\left(\frac{\pi k_2}{2k_N}\right)\left(\frac{\pi k_3}{2k_N}\right)} \right]^p , \tag{2.9}$$

with k_i the i-th component of $\mathbf{k}$, and p indicates the mass assignment function: the NGP ($p = 1$), CIC ($p = 2$) and TSC ($p = 3$) function.

The second step is the Fourier transform of the density field $\delta(\mathbf{x_v})$ to obtain the complex modes of the overdensity, $\delta(\mathbf{k_v})$. The 3D power spectrum is then computed on the mesh, using (Sefusatti et al., 2016; Jing, 2005)

$$P(k) \equiv \langle |\delta(\mathbf{k})|^2 \rangle, \tag{2.10}$$

where $\delta(\mathbf{k})$ is the FT of $\delta(\mathbf{r})$, which is defined as

$$\delta(\mathbf{k}) = \frac{1}{V} \int_V \delta(\mathbf{r}) e^{i\mathbf{k}\cdot\mathbf{r}} d\mathbf{r}. \tag{2.11}$$

For a sample of discrete objects, the density field is given by

$$\delta(\mathbf{k}) = \frac{1}{N} \sum_{\mathbf{g}} n^f(\mathbf{r}_g) e^{i\mathbf{r}_g\cdot\mathbf{k}}. \tag{2.12}$$

[1]https://nbodykit.readthedocs.io

Finally, the power spectrum defined on the mesh is binned. N-BODYKIT has three options to do this: *1)* 1D binning as a function of wavenumber k; *2)* 2D binning as a function of wavenumber k and cosine of the angle to the line-of-sight μ; and *3)* multipole binning as a function of k and multipole number l.

We compute the 1D power spectrum, $P(k)$. We specify the *mode* argument as "1D" to compute the $P(k)$. The number of wavenumber bins is specified via the *dk* and *kmin* keywords. By default, the wavenumber maximum is the Nyquist frecuency, given by $k_{Nyq} = \pi N_{mesh}/L_{box}$, and *dk* is the fundamental mode, given by $dk = 2\pi/L_{box}$.

We also compute the multipoles of $P(k,\mu)$. Multipole binning as a function of k and multipole number l is given by

$$P_l(k) = \frac{2l+1}{2}\int_{-1}^{1} d\mu P(k,\mu)L_l(\mu), \tag{2.13}$$

where L_l is the Legendre polynomial of order l. We compute the two first order multipoles, monopole and quadrupole, by passing *poles* keyword, $poles = [0,2]$, to the *FFTpower* function.

2.1.3 The correlation function via CUTE BOX

The two-point correlation function from data inside a cubical box with periodic boundary conditions is computed as follows: First, take a pair of objects in the data. Second, compute the distance between both objects. Third, bin the pair in a histogram according to the calculated distance. This step is repeated for all pairs in the catalog to obtain the histogram $DD(r)$.

The correlation function is calculated using the "natural" estimator $DD/RR-1$, where *DD* and *RR* are histograms containing the counts of pairs of objects separated by a given distance in the data and random catalog, respectively. Both N-BODYKIT and CUTE BOX consider the random distribution as the catalog has no boundaries. This assumption is valid in the case of N-body simulations due to boundary conditions. A region that lies partly outside the box can be wrapped around in the random catalog. In this particular case, the *RR* histogram can easily be computed as

$$RR(r) = \frac{N^2}{V}v(r), \tag{2.14}$$

where $v(r) = 4\pi((r+dr/2)^3-(r-dr/2)^3)/3 \approx 4\pi r^2 dr$ is the volume of a spherical shell of radius r and thickness dr, $V = L^3$, L is the box size and N is the total number particles.

Finally, the correlation function is calculated as:

$$\xi = \frac{V}{v(r)}\frac{DD(r)}{N^2}. \tag{2.15}$$

No random catalogs are need since we have simple periodic boundary conditions Alonso (2013).

2.2 Standard Perturbation Theory (SPT)

The principal aim in this section is to determine the equations of motion governing the CDM particles which are non-relativistic and collisionless. These particles can be considered as fluid because the number of particles is high $N \gg 1$. Our considered system is a set of CDM particles of a mass m that interact only gravitationally in an expanding universe. The Lagrangian of a particle at position $\mathbf{r} = a(\tau)\mathbf{x}$ under the gravitational potential ϕ_N is given by

$$\mathscr{L} = \frac{1}{2}m\dot{\mathbf{r}}^2 - m\phi_N = \frac{1}{2}m(\dot{a}\mathbf{x} + a\dot{\mathbf{x}})^2 - m\phi_N, \tag{2.16}$$

where $\mathbf{x}$ is the comoving coordinate and $a(t)$ is the scale factor and a dot denotes derivative with respect to cosmic time t, which is related to conformal time τ, $dt = a(\tau)d\tau$. We rewrite the Lagrangian as

$$\mathscr{L} = \frac{1}{2}ma^2\dot{\mathbf{x}}^2 - m\Phi, \tag{2.17}$$

where

$$\Phi = \phi_N + \frac{1}{2}a\ddot{a}\mathbf{x}^2. \tag{2.18}$$

In Eq. 2.17 we have added a total derivative dg/dt to the Lagrangian, with $g = -ma\dot{a}\mathbf{x}^2/2$. The conjugate momentum to $\mathbf{x}$ is then

$$\mathbf{p} = \frac{\partial \mathscr{L}}{\partial \dot{\mathbf{x}}} = ma^2\dot{\mathbf{x}} = ma\mathbf{u}, \tag{2.19}$$

where $\mathbf{u} = a\dot{\mathbf{x}} = d\mathbf{x}/d\tau$ is the peculiar velocity. Hence the velocity of a particle can be written as $\dot{\mathbf{r}} = \mathscr{H}\mathbf{x} + \mathbf{u}(\mathbf{x}, \tau)$, where $\mathscr{H} \equiv da/d\tau$. The equation of motion is hence

$$\frac{d\mathbf{p}}{d\tau} = -ma\nabla\Phi \tag{2.20}$$

We can represent therefore the particle number density of CDM particles by a distribution of representative points in phase space denoted by $f(\mathbf{x}, \mathbf{p}, \tau)$ where $f(\mathbf{x}, \mathbf{p}, \tau)d^3\mathbf{x}d^3\mathbf{p}$ indicates the number of CDM particles that at time τ are contained in a differential element volume $d^3\mathbf{x}d^3\mathbf{p}$. Phase-space conservation implies the Boltzmann Equation

$$\frac{df}{d\tau} = \frac{\partial f}{\partial \tau} + \frac{\partial \mathbf{x}}{\partial \tau}\cdot\nabla f + \frac{\partial \mathbf{p}}{\partial \tau}\cdot\frac{\partial f}{\partial \mathbf{p}} = \left(\frac{\partial f}{\partial \tau}\right)_{coll}, \tag{2.21}$$

where the right side is zero since we consider collisionless particles. Therefore, we need find the collisionless Boltzmann equation for our system considered, set of CDM particles of a mass m that interact only gravitationally in an expanding universe, from which all subsequent

calculations of gravitational instability are derived. The collisionless Boltzmann equation is often called the Vlasov equation.

Using equations (2.19-2.20) we can obtain the Vlasov equation

$$\frac{df}{d\tau} = \frac{\partial f}{\partial \tau} + \frac{\mathbf{p}}{ma}\cdot\nabla f - am\nabla\Phi\cdot\frac{\partial f}{\partial \mathbf{p}} = 0. \tag{2.22}$$

Since we are interested in the evolution of the spatial distribution we can take momentum moments of the distribution function. The zeroth order moment relates the space space density to the density field,

$$\frac{m}{a^3}\int d^3\mathbf{p} f(\mathbf{x},\mathbf{p},\tau) \equiv \rho(\mathbf{x},\tau). \tag{2.23}$$

The next order moments,

$$\frac{1}{a^4}\int d^3\mathbf{p}\,\mathbf{p} f(\mathbf{x},\mathbf{p},\tau) \equiv \rho(\mathbf{x},\tau)\langle \mathbf{u}(\mathbf{x},\tau)\rangle_p \equiv \rho(\mathbf{x},\tau)\mathbf{v}(\mathbf{x},\tau), \tag{2.24}$$

$$\rho\langle u^i u^j\rangle_p = \frac{1}{ma^5}\int d^3\mathbf{p} p^i p^j f(\mathbf{x},\mathbf{p},\tau) \equiv \rho(\mathbf{x},\tau)\mathbf{v}^i(\mathbf{x},\tau)\mathbf{v}^j(\mathbf{x},\tau) + \sigma^{ij}(\mathbf{x},\tau), \tag{2.25}$$

define the mean velocity of particles $\mathbf{v}(\mathbf{x},\tau)$ and the velocity dispersion tensor $\sigma^{ij}(\mathbf{x},\tau)$. In Ecs. (2.24-2.25) we considered the momentum average $\langle(\cdots)\rangle$ over the ensemble of matter particles which are given by

$$\langle A\rangle_p = \frac{\int d^3p A f}{\int d^3p f}, \quad \text{such that} \quad \rho\langle A\rangle_p = \frac{m}{a^3}\int d^3p A f. \tag{2.26}$$

The velocity dispersion tensor is defined as the square of the difference between the peculiar velocities and the mean velocity of the particles averaged over the ensemble, that is

$$\sigma^{ij} \equiv \langle (v^i - u^i)(v^j - u^j)\rangle_p. \tag{2.27}$$

In principle we can obtain an infinite set of equation for the Boltzmann hierarchy. To avoid this we can ignore some terms. For example, for CDM particles we can neglect the velocity dispersion tensor and higher rank tensors since each mean momenta is suppressed by a factor p/m and we are assuming the particles are non-relativistic. In this context, the hydrodynamical equations are obtained by taking moments of the Boltzmann equation (2.22) and using the moments (2.23-2.25)

$$\partial_\tau\rho + 3\mathscr{H} + \partial_i(\rho v^i) \;\; = \;\; 0, \tag{2.28}$$

$$\partial_\tau v^i + \mathscr{H} v^i + v^j\partial_j v^i + \partial^i\Phi = -\frac{1}{\rho}\partial_j(\rho\sigma^{ij}) \tag{2.29}$$

$$\partial_\tau \sigma^{ij} + 2\mathscr{H}\sigma^{ij} + v^k \partial_k \sigma^{ij} + \sigma^{ik}\partial_k v^j + \sigma^{jk}\partial_k v^i = \frac{1}{\rho}\partial_k(\rho\sigma^{ijk}). \tag{2.30}$$

Equation (2.28) describes the conservation of mass; Eq.(2.29) specifies the source of the velocity flows in our cosmic fluid. We take into account the gravitational force and the force due to the pressure in the medium. While the Eq.(2.30) quantifies the deviation of the motion of particles from a coherent flow.

These equations are supplemented by the Poisson equation. Using the fact that the potential $\phi(\mathbf{r})$ induced by the mass density $\rho(\mathbf{r})$ satisfies the Poisson equation $\nabla^2\phi(\mathbf{r}) = 4\pi G\rho(\mathbf{r})$, we can derive the perturbed cosmological gravitational potential $\Phi(\mathbf{x},\tau)$

$$\phi(\mathbf{r},\tau) \equiv -\frac{1}{2}\frac{\partial\mathscr{H}}{\partial\tau}x^2 + \Phi(\mathbf{x},\tau), \tag{2.31}$$

which is sourced only by density fluctuations, as expected. Indeed the Poisson equation reads,

$$\nabla^2\Phi(\mathbf{x},\tau) = \frac{3}{2}\Omega_m(\tau)\mathscr{H}^2(\tau)\delta(\mathbf{x},\tau). \tag{2.32}$$

We write now the above equations in terms of the overdensities. The background density field satisfies

$$\partial_\tau\bar{\rho}(\tau) + 3\mathscr{H}(\tau)\bar{\rho}(\tau) = 0, \tag{2.33}$$

and defining the overdensity $\delta(\mathbf{x},\tau)$ through

$$\rho(\mathbf{x},\tau) = \bar{\rho}(\tau)(1+\delta(\mathbf{x},\tau)). \tag{2.34}$$

we get the useful form

$$\partial_\tau\delta(\mathbf{x},\tau) + \partial_i[1+\delta(\mathbf{x},\tau)v^i(\mathbf{x},\tau)] = 0, \tag{2.35}$$

$$\begin{aligned}\partial_\tau v^i(\mathbf{x},\tau) &+ \mathscr{H}(\tau)v^i(\mathbf{x},\tau) + v^j(\mathbf{x},\tau)\partial_j v^i(\mathbf{x},\tau)\\ &+ \partial^i\Phi(\mathbf{x},\tau) = -\frac{1}{1+\delta(\mathbf{x},\tau)}\partial_j[(1+\delta(\mathbf{x},\tau))\sigma^{ij}(\mathbf{x},\tau)]\end{aligned} \tag{2.36}$$

$$\begin{aligned}\partial_\tau\sigma^{ij}(\mathbf{x},\tau) &+ 2\mathscr{H}(\tau)\sigma^{ij}(\mathbf{x},\tau) + v^k(\mathbf{x},\tau)\partial_k\sigma^{ij}(\mathbf{x},\tau) + \sigma^{ik}(\mathbf{x},\tau)\partial_k v^j(\mathbf{x},\tau)\\ &+ \sigma^{jk}(\mathbf{x},\tau)\partial_k v^i(\mathbf{x},\tau) = \frac{1}{1+\delta(\mathbf{x},\tau)}\partial_k((1+\delta(\mathbf{x},\tau))\sigma^{ijk}(\mathbf{x},\tau)).\end{aligned} \tag{2.37}$$

We note that Eqs. (2.28- 2.30) are coupled, the Eq. (2.28) couples the zeroth (ρ) to the first moment (v^i), the Eq. (2.29) couples the first moment v^i to the second moment (σ_{ij}), and so on. To close the hierarchy we can neglect the VDT, $\sigma_{ij} = 0$ since the effect of virialization

are not important for Cold Dark Matter (CDM); its contribution should be small. Hence the hydrodynamical equations become that of a perfect fluid

$$\partial_t \delta(\mathbf{x},t) + \frac{1}{a}\partial_i[1+\delta(\mathbf{x},t)v^i(\mathbf{x},t)] = 0, \tag{2.38}$$

$$\partial_t v^i(\mathbf{x},t) + \mathscr{H}(\tau)v^i(\mathbf{x},t) + \frac{1}{a}v^j\partial_j v^i + \frac{1}{a}\partial^i\Phi(\mathbf{x},t) = 0 \tag{2.39}$$

Instead of setting $\sigma_{ij} = 0$, an alternative to close the system of equation is postulating an ansatz for the stress tensor σ_{ij}. For example, standard fluid dynamics (Landau, 1959) gives $\sigma_{ij} = -p\delta_{ij} + \eta\left(\nabla_i v^j + \nabla_j v^i - \frac{2}{3}\delta_{ij}\nabla_i v_i\right) + \zeta\delta_{ij}\nabla_i v_i$, with p, η and ζ denotes an effective pressure, shear and bulk viscosity, respectively.

The equation of Motion in the Fourier Representation

The hydrodynamical equations, (2.38) and (2.39), in Fourier space are written as

$$\dot{\delta}(\mathbf{k},\tau) + \theta(\mathbf{k},\tau) = -\int \frac{d^3k_1}{(2\pi)^3}\frac{d^3k_2}{(2\pi)^3}(2\pi)^3\delta_D(\mathbf{k}-\mathbf{k}_{12})\alpha(\mathbf{k}_1,\mathbf{k}_2)\theta(\mathbf{k}_1,\tau)\theta(\mathbf{k}_2,\tau), \tag{2.40}$$

$$\begin{aligned}\dot{\theta}(\mathbf{k},\tau) &+ \mathscr{H}(\tau)\theta(\mathbf{k},\tau) + \frac{3}{2}\Omega_m\mathscr{H}^2(\tau)\delta(\mathbf{k},\tau) \\ &= -\int \frac{d^3k_1}{(2\pi)^3}\frac{d^3k_2}{(2\pi)^3}(2\pi)^3\delta_D(\mathbf{k}-\mathbf{k}_{12})\beta(\mathbf{k}_1,\mathbf{k}_2)\theta(\mathbf{k}_1,\tau)\theta(\mathbf{k}_2,\tau),\end{aligned} \tag{2.41}$$

with $\theta = \nabla\cdot\mathbf{v}$, $\mathbf{k}_{12} = \mathbf{k}_1 + \mathbf{k}_2$ and

$$\alpha = \frac{\mathbf{k}_{12}\cdot\mathbf{k}_1}{k_1^2}, \;\; \beta = \frac{k_{12}^2(\mathbf{k}_1\cdot\mathbf{k}_2)}{2k_1^2k_2^2}. \tag{2.42}$$

The left-hand sides of Eq. (2.40) and Eq. (2.41) represent the linear part of density and velocity field, while the right-hand sides constitute the coupling-mode of number of wavelength k. Due to the mode coupling of the nonlinear terms shown in the right hand side of Eqs. (2.40-2.41) one needs to make a perturbative expansion in $\delta(\mathbf{k},\tau)$ and $\theta(\mathbf{k},\tau)$. For example, for an EdS universe we can expand the $\delta(\mathbf{k},\tau)$ and $\theta(\mathbf{k},\tau)$ as follow

$$\delta(\mathbf{k},\tau) = \sum_n^\infty a^n(\tau)\delta_n(\mathbf{k}), \quad \theta(\mathbf{k},\tau) = -\mathscr{H}(\tau)\sum_n^\infty a^n(\tau)\theta_n(\mathbf{k}). \tag{2.43}$$

The solution to first-order is completely determined by the linear fluctuations since $\delta_1(\mathbf{k}) = -\theta_1(\mathbf{k})$. Solving for δ_2 and θ_2 we obtain the following result

$$\delta_2(\mathbf{k}) = \int d^3k_1 d^3k_2\delta_D(\mathbf{k}-\mathbf{k}_1-\mathbf{k}_2)F_2(\mathbf{k}_1,\mathbf{k}_2)\delta_1(\mathbf{k}_1)\delta_1(\mathbf{k}_2), \tag{2.44}$$

$$\theta_2 = \int d^3k_1 d^3k_2 \delta_D(\mathbf{k}-\mathbf{k}_1-\mathbf{k}_2) G_2(\mathbf{k}_1,\mathbf{k}_2)\theta_1(\mathbf{k}_1)\theta_1(\mathbf{k}_2), \tag{2.45}$$

where

$$F_2 = \frac{5}{7} + \frac{1}{2}\frac{\mathbf{k}_1\cdot\mathbf{k}_2}{k_1 k_2}\left(\frac{k_1}{k_2}+\frac{k_2}{k_1}\right) + \frac{2}{7}\frac{(\mathbf{k}_1\cdot\mathbf{k}_2)^2}{k_1^2 k_2^2}. \tag{2.46}$$

$$G_2 = \frac{3}{7} + \frac{1}{2}\frac{\mathbf{k}_1\cdot\mathbf{k}_2}{k_1 k_2}\left(\frac{k_1}{k_2}+\frac{k_2}{k_1}\right) + \frac{4}{7}\frac{(\mathbf{k}_1\cdot\mathbf{k}_2)^2}{k_1^2 k_2^2}. \tag{2.47}$$

Iteratively we can obtain the kernels F_n, G_n. For example, to calculate the bispectrum is need calculate the kernels F_2 y G_2 since the bispectrum is written in terms of these kernels.

2.2.1 The redshift-space power spectrum

The redshift-space power spectrum can be written as (Vlah and White, 2019)

$$(2\pi)^3\delta_D(\mathbf{k}) + P_s(\mathbf{k}) = \int d^3x e^{-i\mathbf{k}\cdot\mathbf{x}}[1+M(\mathbf{J}=\mathbf{k},\mathbf{x})], \tag{2.48}$$

with $M(\mathbf{J})$ the generating function given by

$$1+M(\mathbf{J},\mathbf{x}) = \langle (1+\delta(\mathbf{x}_1))(1+\delta(\mathbf{x}_2))e^{-i\mathbf{J}\cdot\Delta\mathbf{u}}\rangle, \tag{2.49}$$

with $\mathbf{x} = \mathbf{x}_2 - \mathbf{x}_1$ and $\Delta\mathbf{u} = \mathbf{u}(\mathbf{x}_2) - \mathbf{u}_1(\mathbf{x}_1)$. There are different approaches to RSD modeling depending of the expansion procedure of the generating function. One of this expansion method is the momentum expansion approach, in which the power spectrum is given by

$$P_s(\mathbf{k}) = \sum_{m=0}^{\infty} \frac{(-i)^m}{m!} k_{i_1}\ldots k_{i_m} \hat{\Xi}^m_{i_1\ldots 1_m}(\mathbf{k}), \tag{2.50}$$

with the $\hat{\Xi}^m_{i_1\ldots 1_m}(\mathbf{k})$ are the Fourier moments of the generating function

$$\hat{\Xi}^m_{i_1\ldots 1_m}(\mathbf{k}) = \int d^3x e^{-i\mathbf{k}\cdot\mathbf{x}} \Xi^m_{i_1\ldots 1_m}(\mathbf{x}) \tag{2.51}$$

$$= \int d^3x e^{-i\mathbf{k}\cdot\mathbf{x}} (1+\delta(\mathbf{x}_1))(1+\delta(\mathbf{x}_2))\Delta u_{i_1}\ldots\Delta u_{i_m}. \tag{2.52}$$

The m-th density weighted velocity field moment of the generation function is an m-rank tensor defined as

$$\Xi^m_{i_1\ldots 1_m}(\mathbf{x}) \equiv i^m \frac{\partial^m}{\partial J_{i_1}\cdots\partial J_{i_m}}\left[1+M(\mathbf{J},\mathbf{x})\right]|_{\mathbf{J}=0}$$

$$= \langle (1+\delta(\mathbf{x}_1))(1+\delta(\mathbf{x}_2))\Delta u_{i_1}\ldots\Delta u_{i_m}\rangle. \tag{2.53}$$

The sum should be cutted-off at some finite m, depending on the order of the theory. We consider the three first terms to calculate Kaiser non-linear power spectrum. The power spectrum, to linear order, is given by

$$P_s(k,\mu) = \tilde{\Xi}^{m=0}(\mathbf{k}) - ik_i\tilde{\Xi}^{m=1,ud}(\mathbf{k}) - \frac{1}{2}k_ik_j\tilde{\Xi}^{m=2,dd}(\mathbf{k}). \tag{2.54}$$

Summing up the three contributions, we arrive to

$$P^s_{\rm K,NL}(k,\mu) = \left[P_{\delta\delta}(k) + 2f\mu^2 P_{\delta\theta}(k) + f^2\mu^4 P_{\theta\theta}(k)\right], \tag{2.55}$$

where $P_{\delta\delta}$, $P_{\theta\theta}$ and $P_{\delta\theta}$ are respectively the non-linear matter density, velocity divergence, and density-velocity divergence power-spectra. This power spectrum is known as Non-linear Kaiser power spectrum. The sum is cutted-off at $m = 4$ to calculate the redshift-space power spectrum at one-loop in the moment expansion approach, which is given by

$$P_s^{SPT}(k,\mu) = P_s^{\rm K,NL}(k,\mu) + A(k,\mu) + B(k,\mu) + C(k,\mu) - (k\mu f\sigma_v)^2 P_s^{\rm K}(k,\mu). \tag{2.56}$$

We consider a exponential oscillatory factor to describe virialized, non-coherent random motions of dark-matter particles along the line-of-sight direction. This physically well motivated phenomenological model is given by

$$\begin{aligned} P_s(k,\mu) = &\exp\left[-k^2\mu^2 f^2\sigma_v^2\right] \\ &\left[P_s^{\rm K,NL}(k,\mu) + A(k,\mu) + B(k,\mu) + C(k,\mu)\right]. \end{aligned} \tag{2.57}$$

We consider two variations of perturbation theory, the first, 'standard' perturbation theory is constructed in Eulerian space, where we consider the evolution of the density field at fixed positions. We consider the phenomenological, but physically well motivated, redshift-space models of Scoccimarro (2004) and Taruya et al. (2010) to describe the redshift-space power spectrum, which improve the description of redshift-space distortion (RSD) effects on the power spectrum compared to Kaiser linear theory (Kaiser, 1987). In the following we shall refer to these models as Sc04 and TNS, respectively.

The anisotropic redshift-space clustering originates from the peculiar velocities $\mathbf{v}$ of matter, or more generally any tracer of it, such that an object located at a real space position $\mathbf{r}$ is observed to be located at an apparent redshift-space position $\mathbf{s}$. The relation between coordinates system is inferred via the Doppler effect to be $\mathbf{s} = \mathbf{r} + \hat{\mathbf{n}}v_\parallel(aH)^{-1}$, where $\hat{\mathbf{n}}$ is a the line-of-sight direction of the point-process sample, and $v_\parallel = \mathbf{v}\cdot\hat{\mathbf{n}}$. That is, we are using the plane-parallel approximation on which the observer is located at a distant position of the sample of objects over which we perform the statistics. The redshift-space power spectrum, $\langle|\delta^s(\mathbf{k})|^2\rangle$ is given by

$$\begin{aligned} P^s(\mathbf{k}) = \int d^3r\, e^{i\mathbf{k}\cdot\mathbf{r}} \Big\langle & e^{ik\mu\Delta v_\parallel/(aH)} \left(\delta(\mathbf{x}) - \frac{1}{aH}\nabla_\parallel v_\parallel(\mathbf{x})\right) \\ & \times \left(\delta(\mathbf{x}') - \frac{1}{aH}\nabla_\parallel v_\parallel(\mathbf{x}')\right)\Big\rangle \end{aligned} \tag{2.58}$$

where $\mathbf{r} = \mathbf{x} - \mathbf{x}'$ and $\Delta v_\parallel = v_\parallel(\mathbf{x}) - v_\parallel(\mathbf{x}')$ and $\mu = \hat{\mathbf{n}} \cdot \hat{\mathbf{k}}$ is the angle between the wave vector and the line-of-sight direction. The RSD correction at linear order, known as the Kaiser formula, is given by $\delta_L^s(\mathbf{k}) = (1 + f\mu^2)\delta_L(\mathbf{k})$, where $f = d\log D_+(a)/d\log a(t)$ and $D_+(t)$ the linear growth function. The redshift-space power spectrum at linear order becomes

$$P_K^s(k,\mu) = (1 + f\mu^2)^2 P_L(k). \tag{2.59}$$

The exponential oscillatory factor inside the correlator in equation (2.58) is due to virialized, non-coherent random motions of dark-matter particles along the line-of-sight direction, hence it is in essence non-perturbative. In (Scoccimarro, 2004) this factor is replaced by a phenomenological damping function that accounts for the velocity dispersion $\sigma_v^2 = \langle \theta^2 \rangle$. By rotational symmetry around the line-of-sight direction one obtains a simple prescription

$$\begin{aligned} P^s_{\mathrm{Sc04}}(k,\mu) = &\exp\left[-k^2\mu^2 f^2 \sigma_v^2\right] \\ &\times \left[P_{\delta\delta}(k) + 2f\mu^2 P_{\delta\theta}(k) + f^2\mu^4 P_{\theta\theta}(k)\right], \end{aligned} \tag{2.60}$$

where $P_{\delta\delta}$, $P_{\theta\theta}$ and $P_{\delta\theta}$ are respectively the non-linear matter density, velocity divergence, and density-velocity divergence power-spectra. In linear theory equation (2.60) reduces to the Kaiser power spectrum (equation 2.59) times the damping factor. Several other functional forms for this damping factor have been used in the literature. In this work, we opt for the most common – Gaussian damping. The velocity dispersion is physically motivated to be given by PT as

$$\sigma_v^2 = \frac{1}{6\pi^2} \int dp\, P_{\theta\theta}(p), \tag{2.61}$$

but due to its non-perturbative origin it is commonly replaced by a free parameter σ^2_{FoG}, especially for parameter estimation. However in this work, we regard σ_v^2 as the linear velocity dispersion, which is obtained from the above equation by replacing $P_{\theta\theta}$ by its linear value P_L. This prescription has shown to give good results when comparing theory to simulations (e.g., Taruya et al., 2010). The TNS formalism, on the other hand, expands in cumulants the correlator in equation (2.58), and then replaces a residual exponential factor of the form $\exp\left[\langle e^{ik\mu\Delta v_\parallel/(aH)}\rangle_c\right]$, by a position independent, phenomenological damping factor that can be brought out of the integral. The standard formula for TNS is

$$\begin{aligned} P^s_{\mathrm{TNS}}(k,\mu) = &\exp(-k^2\mu^2 f^2\sigma_v^2)\left[P_{\delta\delta}(k) + 2f\mu^2 P_{\delta\theta}(k)\right. \\ &\left. + f^2\mu^4 P_{\theta\theta}(k) + A(k,\mu) + B(k,\mu)\right], \end{aligned} \tag{2.62}$$

where the new correction terms, $A(k,\mu)$ and $B(k,\mu)$, are given by

$$A(k,\mu) = 2k\mu f \int \frac{d^3p}{(2\pi)^3} \frac{\mathbf{p}\cdot\hat{\mathbf{n}}}{p^2} B_\sigma(\mathbf{p}, \mathbf{k}-\mathbf{p}, -\mathbf{k}), \tag{2.63}$$

$$B(k,\mu) = (k\mu f)^2 \int \frac{d^3p}{(2\pi)^3} F(\mathbf{p}) F(\mathbf{k}-\mathbf{p}), \tag{2.64}$$

with the bispectrum

$$(2\pi)^3\delta_{\rm D}(\mathbf{k}_1+\mathbf{k}_2+\mathbf{k}_3)B_\sigma(\mathbf{k}_1,\mathbf{k}_2,\mathbf{k}_3) = \Big\langle \theta(\mathbf{k}_1) \times \left[\delta(\mathbf{k}_2)+f\frac{(\mathbf{k}_2\cdot\hat{\mathbf{n}})^2}{k_2^2}\theta(\mathbf{k}_2)\right]\left[\delta(\mathbf{k}_3)+f\frac{(\mathbf{k}_3\cdot\hat{\mathbf{n}})^2}{k_3^2}\theta(\mathbf{k}_3)\right]\Big\rangle, \tag{2.65}$$

and

$$F(\mathbf{p}) = \frac{\mathbf{p}\cdot\hat{\mathbf{n}}}{p^2}\left(P_{\delta\theta}(p)+f\frac{(\mathbf{p}\cdot\hat{\mathbf{n}})^2}{p^2}P_{\theta\theta}(p)\right). \tag{2.66}$$

Hence, the TNS model partially accounts for the interaction between the Kaiser effect and the non-linear random motion of particles, reflected in the two extra functions A and B. On the other hand, the Sc04 model factorizes the linear and Finger-of-God effects, so each can be treated separately. The real-space matter power spectrum is given by $P_{\delta\delta}(k) = \langle|\delta(\mathbf{k})|^2\rangle$, which can be obtained from both of the above redshift-space formalism by considering only the perpendicular to line-of-sight components (i.e., $\mu = 0$). After that, one can simply use rotational symmetry to obtain the 1-loop SPT power spectrum

$$P^{\rm SPT}_{\text{1-loop}}(k,t) = P_L(k)+P_{22}(k)+P_{13}(k), \tag{2.67}$$

where P_{22} and P_{13} are the usual 1-loop corrections (e.g., Bernardeau et al., 2002b). The linear power spectrum is the dominant term at large scales. However, at smaller scales, the loop corrections contribute with similar magnitude to the linear power, therefore significantly contributing to the total power spectrum.

We notice that the Q-functions have a IR divergence. For instance, $\hat{q}_3(\mathbf{k},\mathbf{p})$, the integrand of Q_3, has a divergence when the internal momentum is equal to the external momentum $\mathbf{p} = \mathbf{k}$. In order to consider this problem, we split the region of integration in two pieces separated by the $\mathbf{p} = \mathbf{k}$ divergence and using the symmetry $\hat{q}_3(\mathbf{k},\mathbf{p}) = \hat{q}_3(\mathbf{q},\mathbf{k}-\mathbf{p})$, we arrive at

$$Q_3(k) = 2\int_{p<|\mathbf{k}-\mathbf{p}|}\frac{d^3p}{(2\pi)^3}\hat{q}_3(\mathbf{k},\mathbf{p}). \tag{2.68}$$

From the region $p < |\mathbf{k}-\mathbf{p}|$ we obtain $x < k/(2p)$, with $x = \hat{k}\cdot\hat{p}$.

For a scalar rotational invariant function $f(\mathbf{k},\mathbf{p}) = f(k,p,x)$

$$\int_{p<|\mathbf{k}-\mathbf{p}|}\frac{d^3p}{(2\pi)^3}f(\mathbf{k},\mathbf{p}) = \int_{p<|\mathbf{k}-\mathbf{p}|}\frac{d^3p}{(2\pi)^3}f(k,p,x) = \int_0^\infty\frac{dp}{4\pi^2}p^2\int_{-1}^{\text{Min}[1,k/(2p)]}f(k,p,x)dx. \tag{2.69}$$

The numerical integration of the Q-functions consider the IR-divergence. The Eq. 2.68 becomes

$$Q_3 = 2\frac{k^3}{4\pi^2}\int_0^\infty drP_L(kr)\int_{-1}^{\text{Min}[1,1/2r]}dx\frac{x^2(1-rx)^2}{(1+r^2-2rx)^2}P_L\left(k\sqrt{1+r^2-2xr}\right), \tag{2.70}$$

with $r = p/k$. The other Q-functions have a similar expression.

2.3 Lagrangian Perturbation Theory (LPT)

In the previous sections, we considered the density and velocity fields on fixed space with the aim of setting up the Standard (Eulerian) Perturbation Theory (SPT). Now we wish to follow the trajectory of a particle (or an individual fluid element) instead of the density contrast, by using the mapping

$$\mathbf{x}(\mathbf{q},t) = \mathbf{q} + \Psi(\mathbf{q},t) + \Gamma(\mathbf{q},t), \tag{2.71}$$

where $\mathbf{x}(\mathbf{q},t)$ is the (Eulerian) position at a later time t, $\mathbf{q}$ is the (Lagrangian) position at some early time t_{ini}, i.e. $\mathbf{x}(q,t_{ini}) = \mathbf{q}$, with t_{ini} an early time where the evolution of all scales of interest remains linear and the overdensities are quite small, $\delta(x,t_{ini}) = \delta(\mathbf{q}) \ll 1$. Ψ is the longitudinal Lagrangian displacement vector (curl-free component or irrotational vector field, $\nabla \times \Psi = 0$) and Γ is the transverse piece of the Lagrangian displacement (divergence-free component or incompressible vector field, $\nabla \cdot \Gamma = 0$). The Lagrangian displacement vector can be written as the sum of two vector fields: $\mathbf{s} = \Psi + \Gamma$. We note that the peculiar velocity of each particle is

$$\mathbf{u}(\mathbf{x},t) = \frac{d\mathbf{x}}{dt} = \frac{d\mathbf{s}(\mathbf{q},t)}{dt}. \tag{2.72}$$

Also, the velocity dispersion is given by

$$\sigma^{ij}(\mathbf{q},t) = \langle \dot{\Gamma}^i(\mathbf{q},t)\dot{\Gamma}^j(\mathbf{q},t)\rangle_p. \tag{2.73}$$

If we assume that the cold dark matter particles can be considered as an irrotational perfect fluid and we want to describe the matter density 2-point and 1-loop statistics, as in this work, therefore the transverse Lagrangian displacement vector is negligible, i.e. $\Gamma = 0$. On the other hand, if we want to describe the dispersion of the particles and the generation of vorticity, hence the transverse piece has contributions at all orders (Aviles, 2016). Since that we consider an irrotational perfect fluid in our studies, the longitudinal Lagrangian displacement vector is different to zero and the transverse component is equal to zero.

Hence, the equations of motion in LPT scheme are given by

$$\partial_t^2 \Psi^i(\mathbf{q},t) + \mathscr{H}\partial_t \Psi(\mathbf{q},t) + \partial^i \phi(\mathbf{q}+\Psi) = -\frac{1}{1+\delta}\partial_j((1+\delta)\sigma^{ij}), \tag{2.74}$$

$$\partial_t \sigma^{ij}(\mathbf{q},t) + 2\mathscr{H}\sigma^{ij} + \sigma^{ik}\partial_k\partial_t\Psi^j + \sigma^{jk}\partial_k\partial_t\Psi^i = 0, \tag{2.75}$$

where the symbol ∂_i indicates the derivatives with respect to Lagrangian coordinates $\mathbf{q}$. We can define the Jacobian of the transformation from $\mathbf{x}$ to $\mathbf{q}$

$$\left|\frac{d^3q}{d^3x}\right| \equiv \frac{1}{J(\mathbf{q},t)} = \frac{1}{det\left(\delta_{ij} + \frac{\partial\Psi^i}{\partial q^j}\right)}. \tag{2.76}$$

The particle density in the Lagrangian coordinate $\rho(\mathbf{q},t_{ini})$ is the same as the average density of the Universe $\bar{\rho}(t)$. Since the particle density is the same in both coordinate systems, therefore we have

$$\bar{\rho}(t)(1+\delta(\mathbf{q}))d^3q = \rho(\mathbf{x},t)d^3x = \bar{\rho}(t)\left[1+\delta(\mathbf{x},t)\right]d^3x. \tag{2.77}$$

From Eq. (2.77), we can find the relation between Lagrangian displacements and overdensities

$$\delta(\mathbf{x},t) = \frac{1+\delta(\mathbf{q})-J(\mathbf{q},t)}{J(\mathbf{q},t)} \backsimeq \frac{1-J(\mathbf{q},t)}{J(\mathbf{q},t)}. \tag{2.78}$$

Since the particle density in the Lagrangian formalism consider the initial time t_{ini}, we may take t_{ini} early enough so that the initial matter fluctuations $\delta(\mathbf{q},t_{ini})$ are arbitrarily small, i.e. $\delta(\mathbf{q}) \approx 0$. Another expression that relates the density field in terms of the Lagrangian displacement field

$$1+\delta(\mathbf{x},t) = \int d^3q\, \delta_D^{(3)}\left[\mathbf{x}-\mathbf{q}-\Psi(\mathbf{q},t)\right], \tag{2.79}$$

where $\delta_D^{(3)}$ is the Three-dimensional Dirac Delta function. The aim of LPT is to find a perturbative solution for the displacement field. As in the Standard scheme, perturbative solutions for the displacement field are obtained by means of an iterative procedure,

$$\Psi(\mathbf{q},t) = \Psi^{(1)}(\mathbf{q},t) + \Psi^{(2)}(\mathbf{q},t) + \Psi^{(3)}(\mathbf{q},t) + \cdots. \tag{2.80}$$

The first-order solution is the well-know Zel'dovich approximation (Zeldovich, 1970). The solution at fourth-order was obtained in (Rampf and Buchert, 2012). The Fourier transform of Eq. (2.79) is

$$\delta(k) = \int d^3q e^{-i\mathbf{k}\cdot\mathbf{q}}(e^{-i\mathbf{k}\cdot\Psi}-1). \tag{2.81}$$

Therefore, we can express the power spectrum by the integral equation (Taylor and Hamilton, 1996)

$$P_{LPT}(k) = \int d^3q e^{-i\mathbf{k}\cdot\mathbf{q}}\left(\langle e^{-i\mathbf{k}\cdot\Delta}\rangle - 1\right), \tag{2.82}$$

where $\Delta^i = \Psi^i(\mathbf{q}_2) - \Psi^i(\mathbf{q}_1)$ are the Lagrangian displacement differences, and $\mathbf{q} = \mathbf{q}_2 - \mathbf{q}_1$ the Lagrangian coordinate difference.

A similar expression to the two-point correlation function can be deduced in the Lagrangian approach using Eq. (2.79), the LPT correlation function becomes

$$1+\xi_{LPT}(r) = \int \frac{d^3k}{(2\pi)^3}\int d^3q e^{i\mathbf{k}\cdot(\mathbf{r}-\mathbf{q})}\langle e^{-i\mathbf{k}\cdot\Delta}\rangle, \tag{2.83}$$

where $\Delta^i = \Psi^i(\mathbf{q}_2) - \Psi^i(\mathbf{q}_1)$ are the Lagrangian displacement differences at two positions $\mathbf{q}_1$ and $\mathbf{q}_2$ separated by a distance $q = |\mathbf{q}_2 - \mathbf{q}_1|$.

2.3.1 Modelling biased tracers

The underlying matter distribution is not observed by the cosmological surveys, but tracers of the nonlinear density field such as halos and galaxies does.

The positions of tracers are assummed to be drawn according to a distribution depending on local initial conditions such that their overdensities in their initial (Lagrangian) coordinates are given by (Matsubara, 2008a; McDonald and Roy, 2009)

$$F[\delta_0, s_{0,ij}, ..., \nabla\delta_0(\mathbf{q})] = 1 + \delta(\mathbf{q}, \tau_0) \tag{2.84}$$

$$= 1 + b_1\delta_0(\mathbf{q}) + \frac{1}{2}b_2(\delta_0^2(\mathbf{q} - \langle\delta_0^2\rangle)) + b_s(s_0^2(\mathbf{q} - \langle s_0^2\rangle)) + b_3 O_3(\mathbf{q}) + ... + b_\nabla\nabla^2\delta_0(\mathbf{q}), \tag{2.85}$$

where δ_0 is the linear density field, s_0 is the initial shear field, and $O_3(\mathbf{q})$ is the representative third order operator. The initial density field can be mapped to the evolved density field of biased tracers via number conservation. Thus we can write

$$1 + \delta_X(\mathbf{x}) = \int d^3q F[\delta(\mathbf{q}), \nabla^2\delta(\mathbf{q}), s^2(\mathbf{q})]\delta_D[\mathbf{x} - \mathbf{q} - \Psi(\mathbf{q})],$$

$$(2\pi)^3\delta_D(\mathbf{k}) + \delta_X(\mathbf{k}) = \int d^3q e^{i\mathbf{k}\cdot(\mathbf{q}+\Psi(\mathbf{q}))} F[\delta(\mathbf{q}), \nabla^2\delta(\mathbf{q}), s^2(\mathbf{q})]. \tag{2.86}$$

In the Eulerian scheme, the galaxy density field is expressed in terms of a bias expansion based on present-day operators such as the nonlinear density $\delta(\mathbf{x})$. The biasing scheme up to third order is given by (McDonald and Roy, 2009)

$$\delta_X = c_1\delta + \frac{c_2}{2}\delta^2 + c_s s^2 + \frac{c_3}{6}\delta^3 + c_{1s}\delta s^2 + c_{st} st + c_{s3}s^3 + c_\psi\psi, \tag{2.87}$$

with $s^2 = s_{ij}s_{ij}$, $s^3 = s_{ij}s_{jl}s_{li}$, and $st = s_{ij}t_{ij}$, and the shear operators are defined as

$$\psi = \eta - \frac{2}{7}s^2 + \frac{4}{21}\delta^2, \;\; s_{ij} = \left(\frac{\partial_i\partial_j}{\partial^2} - \frac{1}{3}\delta_{ij}\right)\delta, \;\; t_{ij} = \left(\frac{\partial_i\partial_j}{\partial^2} - \frac{1}{3}\delta_{ij}\right)\eta, \;\; \eta = \theta - \delta. \tag{2.88}$$

2.3.2 Convolution Lagrangian Perturbation Theory

In Convolution-LPT (CLPT) we expand in a Taylor series the non-linear pieces out of the exponential allowing to perform analytically the $\mathbf{k}$-integral using standard Gaussian integration techniques (see Carlson et al. (2012b)), by which we arrive at

$$1 + \xi_{\rm CLPT}(r) = \int \frac{d^3q}{(2\pi)^3\det[A_{ij}^L]^{1/2}} e^{\frac{1}{2}A_{ij}^L(r_i - q_i)(r_j - q_j)} \times \left[1 - \frac{1}{2}G_{ij}A_{ij}^{\rm loop} + \frac{1}{6}\Gamma_{ijk}W_{ijk}^{\rm loop} + \cdots\right], \tag{2.89}$$

with cumulants $A_{ij} = \langle \Delta_i \Delta_j \rangle_c$ and $W_{ijk} = \langle \Delta_i \Delta_j \Delta_k \rangle_c$, and tensors $G_{ij} = A^{-1}_{Lij} - g_i g_j$, $\Gamma_{ijk} = A^{-1}_{Lij} g_k + A^{-1}_{Ljk} g_i + A^{-1}_{Lki} g_j - g_i g_j g_k$, and $g_{ij} = A^{-1}_{Lij}(r_j - q_j)$. The label '$L$' in the A function denotes the linear piece and 'loop' the pure 1-loop piece, such that $A_{ij} = A^L_{ij} + A^{\rm loop}_{ij}$. Notice that the '1' in the squared brackets of the above equation corresponds to the Zeldovich correlation function and the other two terms yield the next-to-leading order, 1-loop contributions.

Otherwise, the real space correlation function for tracers which are locally biased in Lagrangian space is given by (Matsubara, 2008a; Carlson et al., 2012b; Vlah et al., 2016)

$$
\begin{aligned}
1 + \xi^{\rm X}_{\rm CLPT}(r) = \int \frac{d^3q}{(2\pi)^3 \det[A^L_{ij}]^{1/2}} e^{\frac{1}{2} A^L_{ij}(r_i - q_i)(r_j - q_j)} \\
\times \Bigg[1 - \frac{1}{2} G_{ij} A^{\rm loop}_{ij} + \frac{1}{6} \Gamma_{ijk} W^{\rm loop}_{ijk} + b_1^2 \xi_L + \frac{1}{2} b_2^2 \xi_L^2 - 2 b_1 U_i g_i \\
- [b_2 + b_1^2] U_i^{(1)} U_j^{(1)} G_{ij} - b_1^2 U_i^{11} g_i - b_2 U_i^{20} g_i - 2 b_1 b_2 \xi_L U_i^{(1)} g_i - b_1 A^{10}_{ij} G_{ij} \\
- b_{s^2} (G_{ij} \Upsilon_{ij} + 2 g_i V_i^{10}) + b_{s^2}^2 \zeta - 2 b_1 b_{s^2} g_i V_i^{12} + b_2 b_{s^2} \chi^{12} \cdots \Bigg],
\end{aligned}
\tag{2.90}
$$

where the first two lines within the eq. (2.90) are the predictions of standard LPT, meanwhile the third line are from the shear-dependence of the bias b_{s^2}. The functions V, ζ, Υ, χ are fourth order terms of the density contrast, i.e. up to $O(\delta^4)$ we have $V_i^{11} = \langle s^2 \Delta_i \rangle_c$, $V_i^{12} = \langle s_1^2 \delta_2 \Delta_i \rangle_c$, $V_{ij} = \langle s^2 \Delta_i \Delta_j \rangle_c$, $\zeta = \langle s_1^2 s_2^2 \rangle_c$, and $\chi^{12} = \langle s_1^2 \delta_2^2 \rangle_c$.

We use the code MGPT (Aviles et al., 2018),[2] in order to solve numerically the CLPT correlation function of equation (2.89), which accounts for the the exact kernels for a ΛCDM background cosmology, instead of the most commonly used Einstein-de Sitter ($\Omega_{\rm m} = 1$) kernels. The difference between both kernels is small, but noticeable, as much as 0.8 per cent at quasi-linear scales at $z = 0$ in the power spectrum.

2.4 Halo model

In this section we discuss about a useful phenomenological description method of the clustering of matter, called "Halo model", whose inceptions go back decades ago (e.g., Seljak, 2000; Peacock and Smith, 2000; Cooray and Sheth, 2002). The main idea is based on the simple assumption that all matter in the Cosmos lies within spherically symmetric halos of some size, where the clustering issue is decomposed into the clustering that arises between haloes and within individual haloes. In other words, this model is based on the premise that on small scales haloes are randomly distributed (one-halo term), while on large scales haloes are not, and displacements of haloes with respect to one another require us to add a two-halo term to the power.

[2] https://github.com/cosmoinin/MGPT

The standard halo-model calculation for the matter power spectrum includes the two halo terms described above. The one-halo term is given by

$$\Delta^2_{1H}(k) = 4\pi \frac{k}{(2\pi)^3} \frac{1}{\overline{\rho}^2} \int_0^\infty M^2 W^2(k,M) F(M) dM, \tag{2.91}$$

where Δ indicates the dimensionless matter power spectrum $\Delta = (k^3/2\pi^2)P(k)$, M is the halo mass, $F(M)$ is the halo mass function (comoving halo number density in dM), $W(k,M)$ is the normalized transform of the halo density profile:

$$W(k,M) = \frac{1}{M} \int_0^{r_v} \frac{\sin(kr)}{kr} 4\pi r^2 \rho(r,M) dr, \tag{2.92}$$

where r_v is the halo virial radius. The Eq. (2.91) is computed as an integral over all halo mass. Mass function and internal density structure are known as functions of cosmology from high-resolution simulations. The halo mass is related to the virial radius, r_v via

$$M = \frac{4}{3}\pi r_v^3 \Delta_v(z) \overline{\rho}, \tag{2.93}$$

where $\Delta_v(z)$ is the virial halo overdensity. Usually, a value of $\Delta_v = 200$ is taken, which is based on the spherical-collapse model in an EdS cosmology.

On large scales, the dimensionless power spectrum associated to spherically symmetric haloes can be approximately the linear-theory power spectrum:

$$\Delta^2_{2H} = \Delta^2_{lin}(k). \tag{2.94}$$

This approximation is valid for the matter distribution. The full halo-model power spectrum is then given by a simple sum of the terms

$$\Delta^2(k) = \Delta^2_{1H} + \Delta^2_{2H}. \tag{2.95}$$

2.4.1 HMCODE

The HMCODE (Mead et al., 2015) model is a variant of the standard model with parameters fitted to the power spectrum data from high-resolution simulations. This method provides a powerful tool to compute the non-linear matter power spectrum at the few percent level for $k < 10hMpc^{-1}$ for a variety of dark energy models such as $\omega(a)$ dark energy, massive neutrinos and modified gravity models with chameleon and Vainshtein screening mechanisms (Mead et al., 2016). This also improves the accuracy of the calculation from ~ 30 per cent to ~ 5 per cent for a wide range of cosmologies and redshifts.

Mead et al. (2016) found that the one-halo term can be augmented in the following way:

$$\begin{aligned} \Delta^2_{1H} &= [1 - e^{-(k/k_*)^2}] 4\pi (\frac{k}{2\pi})^3 \frac{1}{\overline{\rho}} \\ &\times \int_0^\infty M(\nu) W^2(\nu^\eta k, M) f(\nu) d\nu, \end{aligned} \tag{2.96}$$

where ν is the peak threshold $\nu = \delta_c(z)/\sigma(M,z)$, δ_c is the critical density contrast, $f(\nu)$ is the halo mass function, $W(k,M)$ is the normalized Fourier transform of the halo-density profile defined in Eq.(2.92), η is a fitted parameter given by $\eta = 0.603 - 0.3\sigma_8(z)$ to constrict haloes as a functions of their mass at fixed virial radius. Notice that the one-halo term is calculated as an integral over all halo mass.

Mead et al. (2016) use the fitting formula of Nakamura and Suto (1997) to augmented the linear collapse threshold, given by

$$\delta_c = [1.59 + 0.0314 \ln \sigma_8(z)] \times [1 + 0.0123 \log_{10} \Omega_m(z)], \tag{2.97}$$

which is obtained using spherical-collapse model for ΛCDM. Usually δ_c is computed using spherical-collapse model predictions for EdS universe ($\Omega_m = 1$) getting $\delta_c = 1.686$. Mead et al. (2016) also consider a damping term in the one-halo term to prevent divergences on very large scales, which is governed by the fitted parameter $k_* = 0.584\sigma_d^{-1}(z)$. For the virial halo overdensity they use $\Delta_v = 418\Omega_m^{-0.352}(z)$, and for the mass function they use the fitted relation:

$$f(\nu) = A[1 + \frac{1}{(a\nu^2)^p}]e^{-a\nu^2/2}, \tag{2.98}$$

where the parameters of the model are $a = 0.707$, $p = 0.3$ and the normalization A is constrained by the condition that $F(\nu)d\nu$ must integrate to unity, which gives $A \approx 0.2162$. They use halo profiles of Navarro et al. (1997)

$$\rho(r) = \frac{\rho_N}{(r/r_s)(1 + r/r_s)^2}, \tag{2.99}$$

with r_s scale radius that separates the core of the halo from the outer portion and ρ_N is a normalization. This split of the halo is expressed usually via the concentration $c = r_v/r_s$. There is a widely set of $c(M)$ relations in the literature because haloes form at different times in dark energy models. (Mead et al., 2016) use the the concentration–mass relations of Bullock et al. (2001)

$$c(M) = A\frac{1 + z_f(M)}{1 + z}\left[\frac{g(z \to \infty)}{g_\Lambda(z \to \infty)}\right], \tag{2.100}$$

where $g(z)$ represents the linear growth function such that $g(z = 0) = 1$. The 1.5 exponent gives more accurate power spectrum for the more DE models. At small scales the nonlinear power spectrum will be different in DE models because halo concentrations affects on small-scale power. z_f represents the halo formation redshift, which depends on the formation history of the halo.

On the other hand, the two-halo term is given by

$$\Delta^2_{2H}(k) = [1 - f \tanh^2(k\sigma_d/\sqrt{f})]\Delta^2_{lin}(k), \tag{2.101}$$

where f is a free parameter in the fit, σ_v^2 is the 1D linear-theory displacement variance given by

$$\sigma_v^2 = \frac{1}{3}\int_0^\infty \frac{\Delta_{lin}^2}{k^3} dk. \tag{2.102}$$

Notice that in the $k\sigma_v >> 1$ limit, equation (2.101) reduces to $\Delta_{2H}^2 = (1-f)\Delta_{lin}^2$. Eq. (2.101) is motivated by perturbation theory results (e.g., Crocce and Scoccimarro, 2006), which suggest that on quasilinear scales the matter power spectrum can be approximated by a damping term $e^{-k^2\sigma_v^2}$ getting

$$\Delta_{lin}^2 \to e^{-k^2\sigma_v^2}\Delta_{lin}^2. \tag{2.103}$$

We use this augmented version of the halo-model calculation to look at predictions for the non-linear matter power spectrum for the bump cosmology in Chapter 5. We will see that the bump will affect the halo mass function and we expect that it will boost the predicted numbers of haloes in certain mass ranges.

2.4.2 Halo mass function

The number density of dark matter halos of a given mass in a given cosmology is called the halo mass function (HMF). The mass functions can be based on the spherical collapse model and the hypothesis that the mass in collapsed objects is related to the volume with density above a certain threshold. The Press-Schechter (PS) mass functions is based on these assumptions Press and Schechter (1974). However, the PS scheme has deviations at the low mass and the high mass ends. Many mass functions have been proposed, which are based on the more realistic ellipsoidal collapse model. For instance, the Sheth-Tormen HMF, which fits numerical results better, is based on three fitting parameters Sheth et al. (2001).

The functional form for halo mass function

$$\frac{dn}{dM} = f(\sigma)\frac{\bar{\rho}_m}{M}\frac{d\ln\sigma^{-1}}{dM}, \tag{2.104}$$

where $\bar{\rho}_m$ is the average matter density at redshift z, and the mass function $f(\sigma)$ is defined as the fraction of mass in collapsed halos per unit interval in $\ln\sigma^{-1}$, i.e. if all matter is in halos of some mass then

$$\int_\infty^\infty f d\ln\sigma^{-1} = 1. \tag{2.105}$$

A number of mass function have been proposed based on fits to simulation data as the Sheth-Tormen mass function, which is given by

$$f_{ST}(\sigma) = A\sqrt{\frac{2a}{\pi}}\left[1+\left(\frac{\sigma^2}{a\delta_c^2}\right)^p\right]\frac{\delta_c}{\sigma}\exp\left(-\frac{a\delta_c^2}{2\sigma^2}\right), \tag{2.106}$$

with $A = 0.322$, $a = 0.707$, and $p = 0.3$. The quantity $\delta_c = 1.686$ can be interpreted as the linearly extrapolated overdensity of a top-hat spherical density fluctuation at the moment of maximum compression for an matter-dominated universe ($\Omega_m = 1$). The most commonly used analytical halo mass function, the Press-Scheter HMF, can be obtained by choosing $A = 0.5$, $a = 1.0$ and $p = 0.0$. We notice that the dependence on cosmology and power spectrum is absorbed in σ. The rms density fluctuation σ is given by

$$\sigma^2(M,z) = \frac{D^2(z)}{2\pi^2}\int_0^\infty k^2 P(k) W^2(k,M) dk. \tag{2.107}$$

In Eq. (2.107), $P(k)$ is the linear power spectrum, $D(z)$ is the growth factor of linear density perturbations and $W(k,M)$ is the Fourier-space representation of a real-space top-hat filter of radius R in Mpc/h, which on average encloses a mass $M = 4\pi R^3 \bar{\rho_m}(z)/3$, given by

$$W(k,R) = \frac{3}{(kR)^3}\left[\sin(kR) - kR\cos(kR)\right]. \tag{2.108}$$

A commonly used cosmological parameter is σ_8, the filtered variance in spheres of radius $R_T = 8Mpc/h$, which roughly corresponding to the scale of massive galaxy clusters.

2.5 N-body simulations

N-body simulations are a powerful probes to make detailed and reliable predictions for the dark matter based on their general characteristics (Kuhlen et al., 2012). Dark matter simulations consider all matter as collisionless DM neglecting any dissipational baryonic physics. The dark matter particles hence is described by the collisionless Boltzmann equation coupled to Poisson's equation in a comoving coordinate system (see Eqs in section 2.2). The density field is sampled by an ensemble of N phase-space points r_i, $\dot{r}_i$, $i = 1,...,N$ with masses m_i to solve this set of equations. This discrete systems does introduce a characteristic scale since the fluctuations in their forces shrink with distance as $1/r$. In other words, at small distances the fluctuations are large and irregular while at large scales are small and smooth.

Therefore, the main challenge of N-body simulations is to compute the gravitational force that governs the motion of the dark matter particles. There are many different numerical techniques have been developed over the past decades to calculate force of gravity. In this section we describe two methods: one is to evaluate short range forces and the second is using to compute long range interactions.

Tree code is one of the numerical techniques used to evaluate the forces at small distances (Barnes and Hut, 1986). This method is based on a hierarchical tree structure in which the volume is divided into cubic cells and only interactions between particles in distant cells are approximated as a single large particle centered at the distant cell's center of mass. For this reason, the gravitational potential can be treated in terms of a multipole expansion of the mass distribution. The higher order terms in a multipole expansion can be considered depending

of the accuracy requirements. This technique has a $O(N\log N)$ complexity, while the force brute method scale as $O(N^2)$, here N refers to the number of particles.

Otherwise, the adaptive particle-mesh (PM) approach is used to compute the large-scale forces, in which the particles are within an regular mesh to produce density field. Particles are assumed to be divided between the nearby vertices of this discretised space. In denser regions of the simulation the mesh cell are much smaller increasing force accuracy. This method reduces the computational cost from $O(N^2)$ to $M\log M$, where M is the number of mesh cells and is typically taken to be 2^3 times the number of particles.

The hybrid Tree-PM code GADGET combine the tree method, for short range forces, with adaptive particle-mesh (PM), for long range interactions. This software is one of the most widely used cosmological simulation codes and is free. GADGET and other modern simulation codes implement these hybrid solvers to achieve high efficiency.

The gravitational potential is split in Fourier space into a long-range part and a short-range part as follows

$$\phi_{\mathbf{k}} = \phi_{\mathbf{k}}^{\text{long}} + \phi_{\mathbf{k}}^{\text{short}}. \tag{2.109}$$

This breaking requires a spatial scale of the force split labeled as r_s.

Classical equations of motion, in comoving coordinates, are given by

$$\frac{d}{dt}(a^2\dot{\mathbf{x}}) = -\frac{1}{a}\nabla_i\phi(\mathbf{x}_i), \tag{2.110}$$

$$\nabla^2\phi(\mathbf{x}) = 4\pi G\sum_i m_i \times \left[-\frac{1}{L^3} + \sum_{\mathbf{n}}\delta(\mathbf{x}-\mathbf{x}_i-\mathbf{n}L)\right]. \tag{2.111}$$

The sum over i means the N particles, $\mathbf{n}$ is a integer vector, and $\phi = \sum_i m_i\varphi(\mathbf{x}-\mathbf{x}_i)$ is the peculiar gravitational potential. The $-1/L^3$ term is there to make sure that the mean density in Poisson's equation is different of zero.

In order to evolve a particle system is need initial conditions. There is a variety of initial condition codes like GalIC (Yurin and Springel, 2014), N-GenIC (Grossi and Springel, 2009), MusIC (Hahn and Abel, 2011) and 2LPTIC (Crocce et al., 2006). In this thesis, the N-body simulation was carried out starting from $z = 99$ to $z = 0$ in a standard ΛCDM model (see subsection 5.2.2). The following table includes a list of parameters in order to generate initial conditions using N-GenIC:

- Simulation including only dark matter or dark matter with baryonic particles.
- The number of particles N.
- The initial time of the simulation.
- Dark matter density.

- Dark energy density
- Baryonic matter density.
- Hubble parameter.
- Box size of the simulation.
- power spectrum normalization.

We now explain how to generate the initial conditions of a N-body simulation by using the Lagrangian scheme. The cubic box is divided into N^3 regular grid points at redshift z. These points are the Lagrangian coordinate $\mathbf{q}$. We generate now the Gaussian initial density field since Lagrangian displacements are determined by the overdensity field. The density contrast in the Fourier space is given by

$$\delta(\mathbf{k}) \equiv \delta_r(\mathbf{k}) + \delta_i(\mathbf{k}), \tag{2.112}$$

which obeys the Gaussian statistics with mean and variance given by

$$\langle \delta_r(\mathbf{k}) \rangle = 0, \quad \langle \delta_r^2(\mathbf{k}) \rangle = \sqrt{\frac{VP(k)}{2}}, \langle \delta_i(\mathbf{k}) \rangle = 0, \quad \langle \delta_i^2(\mathbf{k}) \rangle = \sqrt{\frac{VP(k)}{2}}. \tag{2.113}$$

In order to generate the random variable, we impose the Hermitian condition of density field

$$\delta(-\mathbf{k}) = \delta*(\mathbf{k}). \tag{2.114}$$

The real density field is given by

$$\delta(\mathbf{q}) = \frac{1}{V}\sum \delta(\mathbf{k}) e^{i\mathbf{k}\cdot\mathbf{q}} = \frac{1}{V}\delta^{\mathrm{FFTW}}(\mathbf{q}). \tag{2.115}$$

Otherwise, the linear Lagrangian displacement field in Fourier space becomes

$$\Psi^{(1)}(\mathbf{k},z) = -i\mathbf{k}\phi^{(1)}(\mathbf{k},t) = i\mathbf{k}\frac{\delta_1(\mathbf{k},z)}{k^2} \tag{2.116}$$

where we have used $-k^2\phi^{(1)}(\mathbf{k},z) = \delta_1(\mathbf{k},z)$. Move particles at each point grid $\mathbf{q}$ by the displacement field at that point

$$\mathbf{x} = \mathbf{q} + \Psi^{(1)}(\mathbf{q},z), \tag{2.117}$$

where the linear displacement is given by

$$\Psi^{(1)}(\mathbf{q},z) = \frac{1}{V}\sum i\mathbf{k}\frac{\delta_1(\mathbf{k},z)}{k^2} e^{i\mathbf{k}\cdot\mathbf{q}}. \tag{2.118}$$

Chapter3

DARK ENERGY MODELS

This chapter is adapted from its corresponding publication, "Cosmological signatures of a rapid diluted energy density. Axel de la Macorra, Dante V. Gomez-Navarro, Jorge Mastache, Alejandro Aviles, Mariana Jaber, and Erick Almaraz. Phys. Rev. D 104, 023529 – Published 28 July 2021".

3.1 Rapidly Diluted Energy Density (RDED)

In this section, we analytically study the cosmological imprints and consequences of having an extra energy density $\rho_{ex}(a)$ beyond the standard ΛCDM that dilutes rapidly at a scale factor a_c. Such a dilution may be generated by a phase transition of the underlying particle model or due to the dynamical properties of the equation of state of the fluid, for example for quintessence dark energy models. In the latter case, the RDED component can be described in terms of a scalar field ϕ, with evolution depending on the choice of a potential $V(\phi)$ and kinetic energy (de la Macorra and Piccinelli, 2000; Steinhardt et al., 1999; Copeland et al., 2006). Here, we will focus on the implications of this energy component over the background expansion history and on cosmological distances.

The BDE is a scalar field ϕ with well defined potential V and kinetic energy E_k (de la Macorra and Almaraz, 2018; Almaraz and de la Macorra, 2019). Its EoS $w = p/\rho = (E_k - V)/(E_k + V)$ behaves as radiation $w = 1/3$ at early times for $a \leq a_c$ when all the elementary particles are relativistic but after the phase transition taking place at a_c, these elementary particle form bounds states (e.g. as baryon and meson in QCD) and the potential energy V dominates ($E_k/V \ll 1$), the EoS jumps to $w = 1$ and the energy density dilutes as $\rho \sim 1/a^6$. At a much later time the EoS goes from $w = -1$ and remains at this value for a long period of time. Finally the w grows from $w = -1$ to $w_o = -0.93$ at a transition redshift $z_c < 2$.

The RDED transition has been suggested in the BDE model, by means of a phase transition

occurring at early times, well inside the radiation dominated epoch $a_c \sim 10^{-6}$, affecting modes $k \sim 1\,h\mathrm{Mpc}^{-1}$ that are entering the horizon at those times. At a much later time, close to present day, a second rapid dilution takes place in BDE (de la Macorra and Almaraz, 2018), where the EoS goes from $w_i = -1$ for $z \gg 1$ to $w_0(z=0) = -0.93$ at present time, with an intermediate value $w(z_c) = -0.965$ at a redshift $z_c = 0.625$, due to the dynamics of the dark energy scalar field. We see that BDE contains two epochs encountering a RDED component one at early times and the second close to the present time.

Alternatively, the late time behaviour of DE has also been investigated in a model independent analysis by introducing a phenomenological EoS $w(a)$, modeling a phase transition with an abrupt change at a_c. In this SEOS models (Jaber and de la Macorra, 2018; Jaber-Bravo et al., 2020) we found a late time transition at $z_c = 0.28$ with $w(z \gg 1) = -1$ and $w_0 = -0.93$, with a lower value of $\chi^2_{BAO+H_0}$ compared to ΛCDM, and consistent with the BDE model. Both BDE and SEOS adjust very well to observations; yet, some Bayesian criteria suggest a better fitting to the data than ΛCDM (de la Macorra and Almaraz, 2018; Jaber and de la Macorra, 2018).

It is worth to emphasize that we do not consider perturbations of SEOS parametrization model. The reason is that SEOS is motivated by the late time dynamics of BDE and we found that the perturbations for the BDE scalar field are subdominant [17]. SEOS generalizes the late time dynamics of BDE, allowing for late time transitions. The EoS of SEOS contains as a limiting case ($q = 1$, $z_c = 1$) the widely used EoS $w = w_0 + (1-a)w_a$.

Here we propose as our working hypothesis, and motivated by BDE, to extract generic properties of having a RDED component in a model independent way. We will add an extra energy density $\rho_{ex}(a)$ present for $a \leq a_c$. The main ingredient in RDED is that the EoS w increases after transition at scale factor a_c $w_{ex}(a \leq a_c) < w_{ex}(a > a_c)$. The value w_{ex} must be larger than the EoS of the leading energy density in the standard model so that ρ_{ex}/ρ_{sm} dilutes. We will present models with at transition scale factor given by a_c at early times $a_c \sim 10^{-5}$ and we referred to this case as BDE-like models and at late times just before Dark Energy starts to dominate defined as SEOS-like models. We assume that after the transition $w_{ex} = 1$ and ρ_{ex} dilutes as $\rho_{ex} \propto 1/a^6$ in the BDE-like examples and we take a transition from $w_{ex} = -1$ to a larger value $w_{ex} \sim -0.93$ in SEOS-like models with a transition at a scale factor $a_c = 0.8$. These two examples examples are motivated by BDE and SEOS previous work. Of course other values of w_{ex} and transitions scale a_c can be taken however the main conclusion on the effect of RDED remains the same.

We will show that a bump is generated in the power spectrum $P(\mathrm{Model})/P(\Lambda\mathrm{CDM})$ for modes $k < k_c$, with $k_c = a_c H(a_c)$. We determine the amplitude and width of these bumps at linear order and first corrections in SPT and compare them to our analytic solutions showing that the bump is indeed produced and that the amplitude is correlated with the amount of the diluted ρ_{ex} however the effect on the Power spectrum differs in early times and late times RDED.

In the rest of this section and in Sect. III, we present a model independent framework for RDED, valid when the extra energy density ρ_{ex} tracks the dominant energy component

closely before the transition takes place at a_c. This allows to study analytically the implications of having ρ_{ex} over cosmological distances and the linear matter densities fluctuations and matter power spectrum. We compare the bumps in section 3.2 and we find good agreements between our simplified analytical developments and those obtained numerically by introducing them into CAMB.

3.1.1 Analytic Model Independent Analysis

We present a model independent framework of RDED. We consider the standard model of cosmology and add an extra energy density ρ_{ex}, that is present only at times before the transition, $a \leq a_c$.

The Hubble parameter $H \equiv \dot{a}/a$ is determined by the Friedman equation

$$H_{sm}^2(a) = \tfrac{8\pi G}{3}\rho_{sm}, \tag{3.1}$$

with

$$\rho_{sm} \equiv \rho_{mo}a^{-3} + \rho_{ro}a^{-4} + \rho_\Lambda \tag{3.2}$$

the standard model total energy density. The matter density ρ_m contains CDM and baryons, ρ_r are the relativistic particles, i.e. photons and neutrinos which we consider massless, while ρ_Λ corresponds to dark energy. The subindex o denotes present time quantities. For scale factors $a \leq a_c$, the extra energy density $\rho_{ex}(a)$ contributes to the total energy density, and Friedmann equation becomes

$$H_{smx}^2(a) = \tfrac{8\pi G}{3}\rho_{smx} = \tfrac{8\pi G}{3}\left(\rho_{sm} + \rho_{ex}\right). \tag{3.3}$$

with

$$\rho_{smx} \equiv \rho_{mo}a^{-3} + \rho_{ro}a^{-4} + \rho_\Lambda + \rho_{ex}. \tag{3.4}$$

Notice that we have used the subscript "*sm*" to refer to the standard model components, while the subscript "*smx*" corresponds to further adding ρ_{ex}. The amount of extra energy density is given by

$$\Omega_{ex} \equiv \frac{\rho_{ex}}{\rho_{sm} + \rho_{ex}} = 1 - \frac{H_{sm}^2(a)}{H_{smx}^2(a)}, \tag{3.5}$$

which in the radiation dominated epoch can be approximated by

$$\Omega_{ex} \simeq \frac{N_{ex}\,\beta}{1 + (N_\nu + N_{ex})\,\beta}, \tag{3.6}$$

with $\rho_{ex} = \beta N_{ex} T_\nu^4$, T_ν the neutrinos temperature, $N_\nu = 3.046$ for three massless neutrinos and $\beta \equiv (7/8)\,(4/11)^{4/3}$.

A RDED takes place if the EoS of ρ_{ex} suffers a transition from $w_c \equiv w_{ex}(a \leq a_c)$ to $w_f \equiv w(a_f > a_c) > w_c$. To have a RDED the value of $\Delta w \equiv w_f - w_c > 0$ must be positive, while the

width $\Delta a \equiv (a_f - a_c)/a_c$ sets the steepness of the transition and how fast ρ_{ex} dilutes compared to ρ_{sm} for $a > a_c$. We define the ratio of energy density for $a > a_c$ as

$$\widetilde{\Omega}_{ex} \equiv \frac{\rho_{ex}}{\rho_{sm}} = \frac{\rho_{ex}^c}{\rho_{sm}^c} \left(\frac{a}{a_c}\right)^{3(w_c - w_f)} \tag{3.7}$$

Notice that a particle with mass m goes from being relativistic, at early times with $T/m \gg 1$, and hence $w_c = 1/3$, to non-relativistic at late times, such that $w_f = 0$ with $\Delta w = w_f - w_c = -1/3$ being negative.
The interesting cases in RDED happen when Δw is positive, and hence this transition is beyond the standard model. Such phase transitions can be realized in dynamical scalar fields (de la Macorra and Piccinelli, 2000; Steinhardt et al., 1999; Copeland et al., 2006), where one finds examples where the EoS evolves from $w_c = 1/3$ to $w_f = 1$.
Here we consider in BDE-like models, where the transition take place in radiation domination epoch ($\rho_{sm} \propto a^{-4}$) and relativistic fluid ρ_{ex} with $w_c = 1/3$ for $a \leq a_c$ with a transition to o $w_f = 1$ at a_c, i.e. we have for $a > a_c$

$$\widetilde{\Omega}_{ex}^r = \frac{\rho_{ex}^c}{\rho_{sm}^c} \left(\frac{a}{a_c}\right)^{-2} \tag{3.8}$$

. On the other hand in SEOS-like models, where the transition takes place during dark energy domination with $w_c \simeq -1$ to $w = -0.93$ close to the present time we have for $a > a_c$ and $3(w_c - w_f) = -0.21 <$.

In section 4.2, we use a modified version of CAMB to follow the exact evolution of ρ_{ex} and we determine the matter and CMB power spectrum and we compare ΛCDM and BDE-like and SEOS-like models.

A transition due to a RDED taking place at a_c modifies H_{sm}, and henceforth the comoving angular distance D_A, the angular diameter $D_M = c/H$, the acoustic scale at recombination r_s and the diffusion damping scale r_d. All these distances are well constrained by CMB (Planck Collaboration, 2018b), BAO (Anderson et al., 2014; Alam et al., 2016, 2020) and SNIa (Scolnic et al., 2018) observations allowing us to constrain the cosmological models. Besides the changes in cosmological distances, the evolution of perturbations will be affected and we determine the matter and CMB power spectra in section 4.2. In Appendix A we show examples of scalar fields yielding indeed this type of transition in the EoS.

3.1.2 Impact on Cosmological Distances

Let us now study how an extra energy density ρ_{ex}, for $a \leq a_c$ and diluting at a_c, affects cosmological distances. The precise value of the distances requires to be numerically calculated, however approximated analytic expressions of the cosmological distances give us an simple understanding on how this ρ_{ex} modifies them, mainly due to a change in the Hubble parameter H.

The sound horizon and damping scale at recombination $a_\star$ are given by

$$r_s(a_\star) = \int_0^{a_\star} \frac{c_s\, da}{a^2 H(a)}, \tag{3.9}$$

with c_s to the sound speed of the photon-baryon plasma,

$$c_s(a) = \frac{1}{\sqrt{3(1+R)}}, \tag{3.10}$$

with $R = (3/4)(\rho_b/\rho_\gamma)$ carrying the speed of sound time dependence. An approximate expression for the damping scale is given by <

$$r_d^2(a_\star) = (2\pi)^2 \int_0^{a_\star} \frac{da}{a^3 \sigma_T n_e H} \left[\frac{R^2 + \frac{16}{15}(1+R)}{6(1+R^2)}\right], \tag{3.11}$$

with n_e the number density of free electrons, σ_T the Thomson scattering cross-section, and the factor in between square brackets is due to the directional and polarization dependence of the electron-photon scattering.

A non-vanishing ρ_{ex} in the region $a \leq a_\star$ will affect the value of the Hubble parameter H, modifying $r_s(a_\star)$ and $r_d(a_\star)$, and impacting the CMB and BAO observations, with the caveat that for BAO measurements one has to consider the drag scale factor $a_{drag} \simeq 9.4 \times 10^{-4}$ instead of the recombination scale $a_\star \simeq 1/1090$ as the upper integration limit. Cosmological distances such as the angular diameter distance at recombination

$$D_A(a_\star) = \int_{a_\star}^{a_o} \frac{da}{a^2 H(a)}, \tag{3.12}$$

will not be affected if $a_c < a_\star$. On the other hand, if the transition occurs after recombination ($a_c > a_\star$), then the acoustic scale, the damping scale and in general cosmological distances, such as

$$d_L(a) = \frac{1}{a}\int_a^{a_o} \frac{da'}{a'^2 H(a')}, \quad D_M(a) = \frac{c}{H(a)}, \tag{3.13}$$

relevant for SNIa and BAO measurements are modified by a non-vanishing ρ_{ex} in $H(a)$ in eqs.(3.12) and (3.13).

3.1.3 Ω_{ex} constant

Let us present the analytic solution assuming Ω_{ex} constant for $a \leq a_c$, valid if ρ_{ex} tracks the leading contribution on H, and $\Omega_{ex} = 0$ for $a > a_c$. In this limit we can express

$$\frac{H_{sm}}{H_{smx}} = \sqrt{1 - \Omega_{ex}} \tag{3.14}$$

which is constant. Since all the cosmological distances considered in the previous subsection the integrand is proportional to $1/H$ we can then simply obtain the ratio of $r_s(a)$ for $a \leq a_c$ in the two models as

$$\begin{aligned} r_s^{smx}(a_c) &\equiv \int_0^{a_c} \frac{c_s\, da}{a^2 H_{smx}} = \int_0^{a_c} \left(\frac{H_{sm}}{H_{smx}}\right) \frac{c_s\, da}{a^2 H_{sm}} \\ &= \sqrt{1-\Omega_{ex}} \int_0^{a_c} \frac{c_s\, da}{a^2 H_{sm}}, \end{aligned} \tag{3.15}$$

and express it in terms of $r_s^{sm}(a_c)$ to obtain

$$\frac{r_s^{smx}(a_c)}{r_s^{sm}(a_c)} = \sqrt{1-\Omega_{ex}}, \tag{3.16}$$

such that the acoustic scale at the transition scale is suppressed by the presence of the extra density component. Similar equations hold generally for cosmological distances,

$$D^{smx}(a_c) = \sqrt{1-\Omega_{ex}}\, D^{sm}(a_c). \tag{3.17}$$

Of course, these results are valid as long as Ω_{ex} remains constant which requires ρ_{ex} to track (i.e. to have the same equation of state) as the leading energy density in H_{smx}, which is a reasonable working hypothesis. If ρ_{ex} dilutes faster than the background it will have little or no effect, meanwhile if ρ_{ex} dominates H it will be ruled out by observations.

Region with $a_c < a_\star$

Here we will study the model when $a_c < a_\star$. In this case we can distinguish two scenarios having $a_c < a_{eq}$ or $a_{eq} < a_c < a_\star$. In the first case let us consider for simplicity and presentation purposes that the Universe is dominated by radiation and we consider c_s constant. The quantity $\Delta r_s(a_\star) \equiv r_s^{smx}(a_\star) - r_s^{sm}(a_\star)$ can be divided in two integrals from a_i to a_c and from a_c to $a_\star$. The second integration will cancel since both terms in $\Delta r_s(a_\star)$ have the same integrand for $a_c \leq a \leq a_\star$ and we than have

$$\Delta r_s(a_\star) = \Delta r_s(a_c) \tag{3.18}$$

where the r.h.s of Eq. (3.18) is evaluated from $a_i \leq a \leq a_c$, with $\Delta r_s(a_c) = r_s^{smx}(a_c) - r_s^{smx}(a_c)$. Using Eq. (3.16) we simply get

$$\frac{\Delta r_s(a_\star)}{r_s^{sm}(a_\star)} = \frac{\Delta r_s(a_c)}{r_s^{sm}(a_\star)} = \left(\sqrt{1-\Omega_{ex}} - 1\right) \left(\frac{r_s^{sm}(a_c)}{r_s^{sm}(a_\star)}\right). \tag{3.19}$$

We see that $\Delta r_s(a_\star) \neq 0$ due to the contribution of Ω_{ex}. On the other hand for $a_c < a_\star$ the angular diameter distance $D_A(a_\star)$ is not affected by Ω_{ex} and we have

$$\Delta D_A(a_\star) = D_A^{smx}(a_\star) - D_A^{sm}(a_\star) = 0. \tag{3.20}$$

Region with $a_\star < a_c$

We consider now a transition for $a_c > a_\star$ with Ω_{ex} constant. The ratio of acoustic scale r_s is

$$\frac{r_s^{smx}(a_\star)}{r_s^{sm}(a_\star)} = \sqrt{1-\Omega_{ex}}, \tag{3.21}$$

while for the angular distance we get

$$\begin{aligned} D_A^{smx}(a_\star) &= \int_{a_\star}^{a_c} \frac{da}{a^2 H_{smx}} + \int_{a_c}^{a_o} \frac{da}{a^2 H_{sm}} \\ &= \sqrt{1-\Omega_{ex}} \int_{a_\star}^{a_c} \frac{da}{a^2 H_{sm}} + \int_{a_c}^{a_o} \frac{da}{a^2 H_{sm}}. \end{aligned} \tag{3.22}$$

We compare $D_A^{smx}(a_\star)$ with $D_A^{sm}(a_\star)$ by taking their difference, $\Delta D_A(a_\star) \equiv D_A^{smx}(a_\star) - D_A^{sm}(a_\star)$, yielding

$$\begin{aligned} \Delta D_A(a_\star) &= \left(\sqrt{1-\Omega_{ex}} - 1\right) \int_{a_\star}^{a_c} \frac{da}{a^2 H_{sm}} \\ &= \left(\sqrt{1-\Omega_{ex}} - 1\right) D_A(a_c) \end{aligned} \tag{3.23}$$

which is negative for $\Omega_{ex} \neq 0$; and therefore, we see that Ω_{ex} reduces $D_A^{smx}(a_\star)$ compared to $D_A^{sm}(a_\star)$.

3.2 Signatures of a RDED on Matter Density Perturbations

We will now study the impact of a RDED model on structure growth and the signals it leaves in the matter power spectrum. We will show that modes entering the horizon before the RDED transition takes place at a_c will grow faster for a non-vanishing ρ_{ex}. This growth generates a bump in the linear matter power spectrum, easily noticeable by taking the quotient of the spectra of models with and without the RDED component. We emphasize that we assume, as in the previous section, that ρ_{ex} tracks the dominant energy component at the time it dilutes.

The bump is located for wave-vectors with $k \geq k_c$, corresponding to modes entering the horizon at a scale factor $a \leq a_c$ with an associated mode

$$k_c \equiv a_c H(a_c). \tag{3.24}$$

Let us now consider the linear evolution of matter densities δ_m in our two models; that we will refer for notational simplicity, as X for the *smx* model, and Λ for the standard model *sm*. The effect of having extra particles ρ_{ex} impacts the amplitude of the energy density perturbation $\delta_m(a_h) = \delta\rho_m(a_h)/\rho_m(a_h)$, the scale factor at horizon crossing (a_h) for the same mode k (i.e. $k = a_h^X H(a_h^X) = a_h^\Lambda H(a_h^\Lambda)$) and the subsequent evolution.

3.2.1 Linear density evolution: Outside Horizon

Outside the horizon the amplitude of the density modes k remain constant, but once they enter the horizon they start to grow. The ratio at horizon crossing is Ma and Bertschinger (1995)

$$\frac{\delta_m^X(a_h^X)}{\delta_m^\Lambda(a_h^\Lambda)} = \frac{1+\frac{4}{15}f_\nu^\Lambda}{1+\frac{4}{15}f_\nu^X}, \tag{3.25}$$

where

$$f_\nu^\Lambda = \frac{\rho_{\rm eff}^\Lambda}{\rho_\gamma+\rho_{\rm eff}^\Lambda}, \qquad \rho_{\rm eff}^\Lambda = \rho_\nu, \tag{3.26}$$

$$f_\nu^X = \frac{\rho_{\rm eff}^X}{\rho_\gamma+\rho_{\rm eff}^X}, \qquad \rho_{\rm eff}^X = \rho_\nu+\rho_{ex}. \tag{3.27}$$

account for the relativistic particles contribution. Since $f_\nu^\Lambda/f_\nu^X \leq 1$ one has a lower amplitude for *smx* model $\delta_m^X(a_h^X) \leq \delta_m^\Lambda(a_h^\Lambda)$.

A fixed mode k that crosses the horizon in the Λ model at the scale factor a_h^Λ, given by $k = a_h^\Lambda H^\Lambda(a_h^\Lambda)$, would otherwise enter the horizon in the X model at a scale factor a_h^X, given by $k = a_h^X H^X(a_h^X)$. Therefore, we get

$$\frac{a_h^X}{a_h^\Lambda} = \frac{H^\Lambda(a_h^\Lambda)}{H^X(a_h^X)} = \sqrt{\frac{1-f_\nu^\Lambda}{1-f_\nu^X}} = \frac{1}{\sqrt{1-\Omega_{ex}}}. \tag{3.28}$$

Notice that the presence of an extra ρ_{ex} component provokes a mode k to enter the horizon at a later time $a_h^X > a_h^\Lambda$ with $H^\Lambda(a_h^\Lambda) > H^X(a_h^X)$. At horizon crossing modes with $k > k_c$ in X and Λ models have a relative scale factor at horizon crossing given by eq.(3.28) $a_h^X/a_h^\Lambda = 1/\sqrt{1-\Omega_{ex}} > 1$. Modes in the X model cross the horizon a later time and have therefore less time to grow and it is reflected as an early suppression in $\Delta\delta_m$. However, after the initial suppression at horizon crossing the matter perturbations in the X model have a higher growing rate than in the ΛCDM model that not only compensates but also reverses the initial suppression.

3.2.2 Linear Matter density evolution: transition at early times in radiation domination

To gain physical intuition on how the rapid diluted dark energy component affects matter density fluctuations well inside the radiation dominated epoch we analyze a simplified version of the equations (ultimately all these quantities will be computed using the code CAMB). To this end, let us solve $\delta_m'' + \mathscr{H}\delta_m' = 0$ where a prime means derivative with respect to conformal time τ and $\mathscr{H} = aH$ is the conformal Hubble rate. The solution is

$$\delta_m'(\tau) = \frac{\tau_i}{\tau} = \frac{aH}{a_i H_i} \tag{3.29}$$

with initial condition $1/\tau_i = \mathscr{H}_i = a_i H_i$ at some pivotal scale a_i, which can be taken as a_c. We can see that for $a < a_c$ we have an increase rate for δ_m for $\rho_{ex} > 0$ and it ceases for modes entering the horizon for $a > a_c$. Therefore the increase takes place only for modes $k \geq k_c$, while modes with smaller k enter the horizon after the RDED dilution has taken place and both models have the same expansion rate and evolution of matter perturbations.

Alternatively, we find convenient to present the evolution in terms of the scale factor, the solution for δ_m is simply a logarithmic function —the Mezsaros effect— $\delta_m(a) = \delta_{mi} + (\delta'_{mi}/k)\ln(a/a_h)$ with initial conditions $\delta'_{mi}/k_i = 2\delta_{mi}$, giving

$$\delta^X_m(a) = \delta^X_{mi}\left(\ln(a/a^X_h) + 1/2\right), \tag{3.30}$$

$$\delta^\Lambda_m(a) = \delta^\Lambda_{mi}\left(\ln(a/a^\Lambda_h) + 1/2\right). \tag{3.31}$$

This enhancement can be semi analytically estimated in terms of the dilution of the extra component ρ_{ex} after a_c. For simplicity we assume that the dilution takes place at a_c and therefore H contains the extra relativistic particles (we name it H^X_+) for $a \leq a_c$ while H^X_- for $a > a_c$ does no longer have them. This change is reflected in the value of initial condition $\delta'_m = \tau_i/\tau$ where we can take the initial condition at $a_i = a_c$ with $\tau_{i-} = 1/\mathscr{H}^X_- = 1/(a_c H^X_-)$, $\tau_{i+} = 1/\mathscr{H}^X_+ = 1/(a_c H^X_+)$ and a ratio $\tau_{i-}/\tau_{i+} = H^X_+/H^X_-$. We obtain then

$$\delta^X_m(a) = \delta^X_{mi}\left[\ln(a_c/a^X_h) + (H^X_+/H^X_-)\ln(a/a_c) + 1/2\right] \tag{3.32}$$

for $a > a_c$ with

$$\frac{H^X_+}{H^X_-} = \frac{1}{\sqrt{1-\Omega_{ex}}}. \tag{3.33}$$

To easily compare Eq. (3.32) to Eq. (3.31) we write $a_c/a^X_h = (a_c/a^\Lambda_h)(a^\Lambda_h/a^X_h)$

$$\delta^X_m(a) = \delta^X_{mi}\left[\left(\frac{H^X_+}{H^X_-}\right)\ln\left(\frac{a}{a_c}\right) + \ln\left(\frac{a_c}{a^\Lambda_h}\frac{a^\Lambda_h}{a^X_h}\right) + \frac{1}{2}\right] \tag{3.34}$$

and leads to a ratio $\Delta\delta_m = \delta^X_m/\delta^\Lambda_m$

$$\Delta\delta_m = \frac{\delta^X_{mi}}{\delta^\Lambda_{mi}}\frac{\left[\left(\frac{H^X_+}{H^X_-}\right)\ln\left(\frac{a}{a_c}\right) + \ln\left(\frac{a^\Lambda_h}{a^X_h}\right) + \ln\left(\frac{a_c}{a^\Lambda_h}\right) + \frac{1}{2}\right]}{\ln\left(\frac{a}{a_c}\right) + \ln\left(\frac{a_c}{a^\Lambda_h}\right) + \frac{1}{2}}, \tag{3.35}$$

with $a_c/a^\Lambda_h = k/k_c$ ($k = a^\Lambda_h H^\Lambda(a^\Lambda_h)$) and a^Λ_h/a^X_h, H^X_+/H^X_- given in Eqs. (3.28) and (3.33), respectively. Equation (3.35) is valid for $a > a_c$ and $k > k_c$. From Eq. (3.35) we see an increase of $\Delta\delta_m$ which tends to $\delta^X_{mi}/\delta^\Lambda_{mi}$ for $k \gg k_c$, while the enhancement is

$$\frac{\delta^X_m}{\delta^\Lambda_m} = \frac{\delta^X_{mi}}{\delta^\Lambda_{mi}}\frac{H^X_+}{H^X_-} \tag{3.36}$$

for $a \gg a_c$. Since $H_+^X/H_-^X > 1$ we see that the linear matter perturbation δ_m in radiation domination grows faster for $\rho_{ex} > 0$. The bump is generated because the linear growth $\delta_m(k)$ has a higher increase rate in radiation domination for larger H, as seen from $\delta_m' = \tau_i/\tau = \mathscr{H}/\mathscr{H}_i \propto aH$. This increase is only valid for modes $k \geq k_c$ while for mode $k < k_c$ both models have the same H and the evolution of $\delta_m(k)$ is the same in both cases. This explains why a RDED model shows a bump compared to ΛCDM. The amplitude of the bump is related to the amount of ρ_{ex} while the width and steepness of the bump are determined by how fast the RDED transition takes place and can be parametrized phenomenological by the quantities $\Delta a = (a_f - a_c)/a_c$ and $\Delta w = w_f - w_c$. The modes $k < k_c$ that enter the horizon after a_c are not affected by the extra energy density ρ_{ex} dilution, for these modes we have $H_+^X = H_-^X$ and $a_h^X = a_h^\Lambda$. The final shape of the matter power spectrum is a combination of the present value of δ_m determined by the dynamical processes described in this section and the fitting values of n_s and A_s which define the primordial spectrum P_s. Here we consider the same P_s in *sm* and *smx* models.

Matter Power Spectrum: Transition at early times in radiation domination

Let us now estimate the amplitude and width of the bump generated by the RDED in radiation domination and we will compare with the numerical simulations obtained from CAMB and shown in table 4.1.

We take $\widetilde{\Omega}_{ex}$ defined in eq.(3.7) and with an EoS $w_{ex}(a_c) = 1/3$ for $a \leq a_c$ and $w_{ex} = 1$ for $a > a_c$. In the region $a \geq a_c$ we have then

$$\widetilde{\Omega}_{ex}(a) \equiv \frac{\rho_{ex}}{\rho_{sm}} \simeq \frac{\rho_{ex}}{\rho_r} = \widetilde{\Omega}_{ex}^c \left(\frac{a}{a_c}\right)^{-2} \tag{3.37}$$

and we find convenient to express H_X as

$$H_X(a) = H_\Lambda(a)\sqrt{1+\widetilde{\Omega}_{ex}(a)}. \tag{3.38}$$

since $\rho_{smx}/\rho_{sm} = 1 + \rho_{ex}/\rho_{sm}$. Hence, since the primordial power spectra of the two models is assumed to be the same, we have

$$R_L^T \equiv \frac{P_X(k,a)}{P_\Lambda(k,a)} = \left(\frac{\delta_m^X}{\delta_m^\Lambda}\right)^2 = \left(\frac{\delta_{mi}^X}{\delta_{mi}^\Lambda}\right)^2 \left(\frac{H^X}{H^\Lambda}\right)^2 \tag{3.39}$$

$$= \left(\frac{\delta_{mi}^X}{\delta_{mi}^\Lambda}\right)^2 \left(1+\widetilde{\Omega}_{ex}(a)\right). \tag{3.40}$$

we see that the ratio of power spectra P_X/P_Λ are proportional to $\widetilde{\Omega}_{ex}(a_c)$ and the largest ratio is for the mode $k \sim k_c$. Since for $a \gg a_c$ the amount of $\widetilde{\Omega}_{ex}$ dilutes rapidly we expect the ratio of power spectra to diminish. For simplicity we take the same initial condition

at horizon crossing $\delta^X_{mi} = \delta^\Lambda_{mi}$. We will define the value of k_{min} and a_{min} at an arbitrary minimum ratio $R^T_L = P_X(k,a)/P_\Lambda(k,a)$ which we take as $R^T_L = 1.01$ or equivalently a value of $\widetilde{\Omega}_{ex} = 0.01$, corresponding to a 1% difference between in the power spectra amplitude of these two models. Of course other values of $\widetilde{\Omega}_{ex}$ and R^T_L may be used as references.

Let is now take the ratio of the two modes $k_c = a_c H(a_c)$ and $k_{min} = a_{min} H(a_{min})$. The ratio k_c/k_{min} sets the width of the bump with $\Delta k = k_c - k_{min} = k_c(1 - k_{min}/k_c)$ with k_c the largest value. We find

$$\begin{aligned} \frac{k_{min}}{k_c} &= \frac{a_{min}}{a_c}\frac{H^X_{min}}{H^X_c} = \frac{a_{min}}{a_c}\frac{H^\Lambda_{min}}{H^\Lambda_c}\sqrt{\frac{1+\widetilde{\Omega}_{ex}(a_{min})}{1+\widetilde{\Omega}_{ex}(a_c)}} \\ &= \sqrt{\frac{\widetilde{\Omega}_{ex}(a_{min})}{\widetilde{\Omega}_{ex}(a_{min})}}\sqrt{\frac{1+\widetilde{\Omega}_{ex}(a_c)}{1+\widetilde{\Omega}_{ex}(a_c)}} \end{aligned} \tag{3.41}$$

where we have used eqs.(3.38) and that in radiation domination $a^2_{min}H^\Lambda_{min} = a^2_c H^\Lambda_c$ giving

$$\left(\frac{a_c}{a_{min}}\right)^{1/2} = \frac{a_{min}}{a_c}\frac{H^\Lambda_{min}}{H^\Lambda_c} = \left(\frac{\widetilde{\Omega}_{ex}(a_{min})}{\widetilde{\Omega}_{ex}(a_c)}\right)^{1/2}. \tag{3.42}$$

The results and values for different modes k_c and amplitudes are shown in table 4.1. We compare our theoretical estimation with a full CMB implementation of our models and we find a very good agreement.

3.2.3 Linear Matter density evolution: Transition in Dark Matter domination

Let as now consider the case when a RDED transition takes place during matter domination and we add an extra energy density ρ_{ex} that evolves as matter. The RDED takes place at a_c and ρ_{ex} evolves from $\rho_{ex} \propto a^{-3}$ for $a < a_c$ to $\rho_{ex} \propto a^{-6}$ for $a > a_c$ diluting rapidly.
We assume the same amount of matter ρ_m in both models *sm* and *smx* but since in this case ρ_{ex} evolves also as matter the total amount of matter becomes

$$\rho^X_m = \rho_m + \rho_{ex}, \qquad \rho^\Lambda_m = \rho_m \tag{3.43}$$

and with a energy density ratio

$$\Omega^X_m \equiv \frac{\rho_m + \rho_{ex}}{\rho_{smx}}, \qquad \Omega^\Lambda_m = \frac{\rho_m}{\rho_{sm}}, \tag{3.44}$$

with ρ_{sm} and ρ_{smx} defined in eqs.(3.2) and (3.4) respectively, and

$$\widetilde{\Omega}_{ex}(a) \equiv \frac{\rho_{ex}(a)}{\rho_{sm}(a)} = \frac{\rho_{ex}(a)}{\rho_m(a) + \rho_r(a) + \rho_\Lambda(a)}. \tag{3.45}$$

The quotient of Ω_m is

$$\frac{\Omega_m^\Lambda}{\Omega_m^X} = \left(\frac{\rho_m}{\rho_m+\rho_{ex}}\right)\left(\frac{H^X}{H^\Lambda}\right)^2 = \frac{1+\widetilde{\Omega}_{ex}}{1+\rho_{ex}/\rho_m} \tag{3.46}$$

with a the ratio of H given by

$$\frac{(H^X)^2}{(H^\Lambda)^2} = \frac{\rho_m+\rho_r+\rho_\Lambda+\rho_{ex}}{\rho_m+\rho_r+\rho_\Lambda} = 1+\widetilde{\Omega}_{ex}. \tag{3.47}$$

In matter domination the evolution of the linear matter density perturbations is proportional to the scale factor a and in the *sm* model we have

$$\delta_m^\Lambda(a) = \delta_{mi}^\Lambda\left(\frac{a}{a_h^\Lambda}\right). \tag{3.48}$$

In the *smx* model the linear evolution of δ_m^X is impacted by the transition of ρ_{ex} at a_c. Here, for presentation purposes we assume as in section 3.2.2 a step transition of $\widetilde{\Omega}_{ex}$ at a_c with $\widetilde{\Omega}_{ex}(a \geq a_c)$ vanishing. Of course the numerical implementation of the evolution in CAMB has a smooth transition $\widetilde{\Omega}_{ex}$ at a_c. This transition can be estimated at a_c by the RDED of ρ_{ex} with $(a_c^-/a_c^+) = (H_+^X(a_c)/H_-^X(a_c))^{2/3} = (1+\Omega_{ex}(a_c))^{1/3}$ and $\Omega_{ex}(a > a_c) = 0$. The evolution of the linear matter density perturbation is than given by

$$\begin{aligned}
\delta_m^X(a) &= \delta_{mi}^X\left(\frac{a}{a_h^X}\right) = \delta_{mi}^X\left(\frac{a_c^+}{a_h^X}\right)\left(\frac{a_c^-}{a_c^+}\right)\left(\frac{a}{a_c^-}\right) \\
&= \delta_{mi}^X\left(\frac{H_+^X(a_c)}{H_-^X(a_c)}\right)^{2/3}\left(\frac{a}{a_h^X}\right) \qquad (3.49)\\
&= \delta_{mi}^X\left(1+\widetilde{\Omega}_{ex}(a_c)\right)^{1/3}\left(\frac{a}{a_h^X}\right). \qquad (3.50)
\end{aligned}$$

Of course the value of the scale factor at a_c does not vary, it is just the scale where $H^X(a_c)$ is impacted by the RDED of ρ_{ex}.

Matter Power Spectrum: transition in matter domination

We will now determine the matter power spectrum and determine the observational consequences of a late time transition. For that purposes we compare $\delta_m = \delta\rho/\rho$ for the same mode k, with $k = a_h^X H_c^X(a_h^X) = a_h^\Lambda H_c^\Lambda(a_h^\Lambda)$, obtaining

$$\frac{a_h^X}{a_h^\Lambda} = \frac{H^\Lambda(a_h^\Lambda)}{H^X(a_h^X)} = 1+\widetilde{\Omega}_{ex}(a_h^X), \tag{3.51}$$

which shows that modes in the *smx* model enter the horizon at a later time than in the *sm* model. For modes entering the horizon well before the matter-radiation equality $\widetilde{\Omega}_{ex}(a_h^X) \ll 1$, since in radiation ρ_r dominates ρ_{smx} with $\rho_{ex} \ll \rho_r$, while modes $k < k_c$ entering the horizon after the transition a_c have $\widetilde{\Omega}_{ex}(a_h^X) = 0$ due to the RDED of $\rho_{ex}(a)$, i.e. $\rho_{ex}(a) = 0$ for $a > a_c$. Let us now estimate now the matter power spectrum, assuming the same primordial power spectrum P_s in both *sm* and *smx* models. The ratio of power spectra $P_X(k,a)/P_\Lambda(k,a) = (\delta_m^X(k,a)/\delta_m^\Lambda(k,a))^2$ is

$$\begin{aligned} \frac{P_X(k,a)}{P_\Lambda(k,a)} &= \left(\frac{\delta_{mi}^X}{\delta_{mi}^\Lambda}\right)^2 \left(\frac{a_h^\Lambda}{a_h^X}\right)^2 \left(1+\widetilde{\Omega}_{ex}(a_c)\right)^{2/3} \\ &= \left(\frac{\delta_{mi}^X}{\delta_{mi}^\Lambda}\right)^2 \frac{\left(1+\widetilde{\Omega}_{ex}(a_c)\right)^{2/3}}{\left(1+\widetilde{\Omega}_{ex}(a_h^X)\right)} \end{aligned} \tag{3.52}$$

where we have used eqs.(3.48), (3.50) and (3.51). The term coming from eq.(3.51) is an overall suppression due to extra particles at horizon crossing while the term eq.(3.50) corresponds to an enhancement of the matter power spectrum due to the RDED of ρ_{ex} at a_c.
The relative amplitude in the power spectra in eq.(3.52) is determined by the extra energy density $\widetilde{\Omega}_{ex}(a_c)$ at the transition a_c and at the time of horizon crossing $\widetilde{\Omega}_{ex}(a_h^X)$ for the different modes k. The evolution of $\widetilde{\Omega}_{ex}(a)$ given in eq.(3.62) and plotted in figure 4.3 shows that $\widetilde{\Omega}_{ex}(a)$ peaks at $a = a_c$, while for $a \ll a_c$ and for $a > a_c$ the amount of $\widetilde{\Omega}_{ex}$ is subdominant and tends to vanish. In a steep RDED transition we can approximate $\Omega_{ex}(a) = 0$ for $a > a_c$. Large modes $k < k_c$ enter the horizon at late times with $a > a_c$, $\widetilde{\Omega}_{ex}(a > a_c) = 0$ and $\widetilde{\Omega}_{ex}(a_h^X) = 0$. Therefore there is no enhancement in the power spectrum, $P_X(k,a_o)/P_\Lambda(k,a_o) = 1$ for $k < k_c$, which is verified by the numerical implementation shown in Fig. 4.6. On the other hand small modes $k > k_c$, enter the horizon before at a_c (i.e. $a_h^X < a_c$) and we have a reduction in the ratio power spectra in eq.(3.52) due to the suppression from horizon crossing determined by $\widetilde{\Omega}_{ex}(a_h^X) > 0$ and a boost due to the RDED of $\widetilde{\Omega}_{ex}(a_c)$ at a_c. To conclude we find the ratio of power spectra $P_X(k,a_o)/P_\Lambda(k,a_o)$ shows an increase for modes $k > k_c$ due to the extra amount of matter $\rho_{ex}(a > a_c)$ but there is no increase for modes $k < k_c$.

We define the width of the bump from the transition mode k_c to the maximum of the bump in $P_X(k_b,a_0)/P_\Lambda(k_b,a_0)$ defined by the mode k_b. Following the same steps as in section 3.2.2 we determine the width of the bump $\delta k = k_c - k_b$ by taking the ratio k_c/k_b is in this case

$$\begin{aligned} \frac{k_b}{k_c} &= \frac{a_b}{a_c}\frac{H_b^X}{H_c^X} = \frac{a_b}{a_c}\frac{H_b^\Lambda}{H_c^\Lambda}\sqrt{\frac{1+\widetilde{\Omega}_{ex}(a_b)}{1+\widetilde{\Omega}_{ex}(a_c)}} \\ &\simeq \left(\frac{\widetilde{\Omega}_{ex}(a_b)}{\widetilde{\Omega}_{ex}(a_c)}\right)^{1/6} \sqrt{\frac{1+\widetilde{\Omega}_{ex}(a_b)}{1+\widetilde{\Omega}_{ex}(a_c)}} \end{aligned} \tag{3.53}$$

where we have approximated a_b/a_c in eq.(3.53) by

$$\left(\frac{a_c}{a_b}\right)^{1/2} = \frac{a_b}{a_c}\frac{H_b^\Lambda}{H_c^\Lambda} = \left(\frac{\widetilde{\Omega}_{ex}(a_b)}{\widetilde{\Omega}_{ex}(a_c)}\right)^{1/6}. \tag{3.54}$$

valid in matter domination.

3.2.4 Linear Matter density evolution: transition at late times in dark energy domination

Let us now consider the case where the RDED takes place at late times. The evolution of the linear matter density perturbations are well described by the ansatz

$$f \equiv \frac{d\log\delta_m}{d\log a} = \Omega_m^\gamma(a) \tag{3.55}$$

where $\gamma \simeq 0.55$ in a ΛCDM model. In the regime where Ω_m constant the solution to Eq. (3.55) is just

$$\delta_m^X(a) = \delta_{mi}^X\left(\frac{a}{a_h^X}\right)^{(\Omega_m^X)^\gamma} \tag{3.56}$$

$$\delta_m^\Lambda(a) = \delta_{mi}^\Lambda\left(\frac{a}{a_h^\Lambda}\right)^{(\Omega_m^\Lambda)^\gamma}. \tag{3.57}$$

However we do not expect Ω_m to be constant. Still equations (3.57) are a good approximation as we will see by comparing our results with the numerical implementation. The amount of extra energy density is given by

$$\widetilde{\Omega}_{ex}(a) \equiv \frac{\rho_{ex}(a)}{\rho_{sm}(a)} \simeq \frac{\rho_{ex}(a)}{\rho_m(a)+\rho_\Lambda(a)}. \tag{3.58}$$

The transition takes place at late times during dark energy domination and is not due to an additional fluid but corresponds to the distinctive evolution of a cosmological constant with $w_\Lambda \equiv -1$ and a dynamical dark energy with $w(a)$, as for example in BDE model (Almaraz and de la Macorra, 2019; de la Macorra and Almaraz, 2018) or quintessence models (Zlatev et al., 1999; Steinhardt et al., 1999; de la Macorra and Piccinelli, 2000), (de la Macorra and Stephan-Otto, 2002; de la Macorra, 2005; De la Macorra, 2003) and the review work(Copeland et al., 2006). The evolution of $\rho_{de}(a)$ is a time dependent quantity given by

$$\rho_{de}(a) = \rho_\Lambda\, e^{\int_{a_o}^a da\, 3(1+w(a))} \tag{3.59}$$

with $\rho_{de}(a_o) = \rho_\Lambda$ and $\rho_\Lambda = \Lambda^4$ the cosmological constant. We define $\rho_{ex}(a)$ as the difference between DE and the cosmological constant,

$$\rho_{ex}(a) = \rho_{de}(a) - \rho_\Lambda = \rho_\Lambda \left(e^{\int_{a_o}^{a} da\, 3(1+w(a))} - 1 \right) \tag{3.60}$$

giving $\rho_{ex}(a_o) = 0$. In this case we have

$$\Omega_m^X = \frac{\rho_m}{\rho_m + \rho_{ex} + \rho_\Lambda}, \quad \Omega_m^\Lambda \equiv \frac{\rho_m}{\rho_m + \rho_\Lambda} \tag{3.61}$$

with

$$\frac{\Omega_m^\Lambda}{\Omega_m^X} = \frac{(H^X)^2}{(H^\Lambda)^2} = \frac{\rho_m + \rho_\Lambda + \rho_{ex}}{\rho_m + \rho_\Lambda} = 1 + \widetilde{\Omega}_{ex}. \tag{3.62}$$

Matter Power Spectrum:
transition at late times in dark energy domination

We will now determine the matter power spectrum and determine the observational consequences of a late time transition. For that purposes we will compare $\delta_m = \delta\rho/\rho$ for the same mode k, with $k = a_h^X H_c^X(a_h^X) = a_h^\Lambda H_c^\Lambda(a_h^\Lambda)$ and assuming for simplicity and presentation purposes that modes enter in matter domination with $H_c^\Lambda(a_h^\Lambda) = H_c^\Lambda(a_h^X)(a_h^X/a_h^\Lambda)^{3/2}$ we obtain

$$\frac{a_h^X}{a_h^\Lambda} = 1 + \widetilde{\Omega}_{ex}(a_h^X) \tag{3.63}$$

showing that modes in SEOS-like model enter later than in ΛCDM. We estimate the matter power spectrum, assuming the same P_s in both models using eqs.(3.56) and (3.57) we get $P_X(k,a)/P_\Lambda(k,a) = (\delta_m^X(k,a)/\delta_m^\Lambda(k,a))^2$ with

$$\frac{P_X(k,a)}{P_\Lambda(k,a)} = \left(\frac{\delta_{mi}^X}{\delta_{mi}^\Lambda}\right)^2 \left(\frac{a_h^\Lambda}{a_h^X}\right)^{2(\Omega_m^X)^\gamma} \left(\frac{a}{a_h^\Lambda}\right)^{2((\Omega_m^X)^\gamma - (\Omega_m^\Lambda)^\gamma)} \tag{3.64}$$

with

$$(\Omega_m^X)^\gamma - (\Omega_m^\Lambda)^\gamma = (\Omega_m^X)^\gamma \left(1 - \left(\frac{\Omega_m^\Lambda}{\Omega_m^X}\right)^\gamma\right) \tag{3.65}$$

with $\Omega_m^\Lambda/\Omega_m^X$ given in eq.(3.46) for a ρ_{ex} model with a transitions in matter domination and as in eq.(3.62) for a transition in dark energy domination.

For $\widetilde{\Omega}_{ex} \ll 1$ we have $(1+\widetilde{\Omega}_{ex})^\gamma = 1 + \gamma\widetilde{\Omega}_{ex} + O(\widetilde{\Omega}_{ex}^2)$. Notice that $\widetilde{\Omega}_{ex}(a_0) = 0$ and $\Omega_m^X(a_0) = \Omega_m^\Lambda(a_0) = \Omega_m(a_0)$ and therefore we have an overall suppression in of the power

spectra for all modes with

$$\frac{P_X(k,a_0)}{P_\Lambda(k,a_0)} = \left(\frac{\delta^X_{mi}}{\delta^\Lambda_{mi}}\right)^2 \left(\frac{a^\Lambda_h}{a^X_h}\right)^{2(\Omega_{mo})^\gamma} \tag{3.66}$$

$$= \left(\frac{\delta^X_{mi}}{\delta^\Lambda_{mi}}\right)^2 \left(1+\widetilde{\Omega}_{ex}(a^X_h)\right)^{-2(\Omega_{mo})^\gamma}. \tag{3.67}$$

This overall suppression is due to dynamical dark energy compared to a cosmological constant and here we studied this effect by means of an effective energy density ρ_{ex} defined in eq.(3.60) which takes into account the difference between DE and the cosmological constant.

Let us now study the effect of RDED of ρ_{ex}. In this case we will simplify the analysis and we will consider that ρ_{ex} vanishes at a given scale defined here by the transition scale factor a_T with $\rho^T_{ex} \equiv \rho_{ex}(a_T)$ and $\rho_{ex}(a) = 0$ for $a > a_T$. The transition scale a_T may coincide with a_c but in SEOS model this is not necessarily the case. Let is take the evolution of the perturbations as

$$\tilde{\delta}^X_m(a) = \delta^X_{mi}\left(\frac{a_T}{a^X_h}\right)^{(\Omega^X_m)^\gamma}\left(\frac{a}{a_T}\right)^{(\tilde{\Omega}^X_m)^\gamma} \tag{3.68}$$

$$\delta^X_m(a) = \delta^X_{mi}\left(\frac{a_T}{a^X_h}\right)^{(\Omega^X_m)^\gamma}\left(\frac{a}{a_T}\right)^{(\Omega^X_m)^\gamma}. \tag{3.69}$$

and the power spectrum becomes

$$R^{TX}_L(a) \equiv \frac{\tilde{P}_X(k,a)}{P_X(k,a)} = \left(\frac{a}{a_T}\right)^{2[(\tilde{\Omega}^X_m)^\gamma - (\Omega^X_m)^\gamma]} \tag{3.70}$$

where $\tilde{\Omega}^X_m$ has $\rho_{ex} = 0$ (i.e. $\tilde{\Omega}^X_m = \Omega^\Lambda$) and

$$\chi \equiv (\tilde{\Omega}^X_m)^\gamma - (\Omega^X_m)^\gamma = (\Omega^X_m)^\gamma\left(\left[1+\widetilde{\Omega}_{ex}(a_T)\right]^\gamma - 1\right). \tag{3.71}$$

is evaluated at a_T with $\widetilde{\Omega}_{ex}(a_T) = \rho_{ex}(a_T)/(\rho_m(a_T)+\rho_\Lambda)$. From eq.(3.70) we clearly see that $\chi > 1$ and a bump, an increase in the power spectrum, is indeed generated due to the RDED. We determined the hight of the bump in terms of the extra energy density $\widetilde{\Omega}_{ex}$ and let us know determine the width of the bump. For definiteness will defined the width of the bump from the transition mode k_c to a $k_{max} > k_c$ corresponding to an arbitrary mode where the increase in the power spectrum is only 1% i.e. $\tilde{P}_X(k,a_0)/P_X(k,a_0) = 1.01$.

Following the same steps as in section 3.2.2 we determine the width of the bump $\delta k =$

$k_c - k_{max}$ by taking the ratio k_c/k_{max} is in this case

$$\begin{aligned} \frac{k_{max}}{k_c} &= \frac{a_{max}}{a_c}\frac{H^X_{max}}{H^X_c} = \frac{a_{max}}{a_c}\frac{H^\Lambda_{max}}{H^\Lambda_c}\sqrt{\frac{1+\widetilde{\Omega}_{ex}(a_{max})}{1+\widetilde{\Omega}_{ex}(a_c)}} \\ &\simeq \left(\frac{\widetilde{\Omega}_{ex}(a_{max})}{\widetilde{\Omega}_{ex}(a_c)}\right)^{1/6}\sqrt{\frac{1+\widetilde{\Omega}_{ex}(a_{max})}{1+\widetilde{\Omega}_{ex}(a_c)}} \end{aligned} \tag{3.72}$$

where we have approximated a_{max}/a_c in eq.(3.72)

$$\left(\frac{a_c}{a_{max}}\right)^{1/2} = \frac{a_{max}}{a_c}\frac{H^\Lambda_{max}}{H^\Lambda_c} = \left(\frac{\widetilde{\Omega}_{ex}(a_{max})}{\widetilde{\Omega}_{ex}(a_c)}\right)^{1/6}. \tag{3.73}$$

valid in matter domination. Of course if the transition takes place when Dark Energy is no longer subdominant a numerical estimation of a_c/a_{max} should no be used.

Chapter4

RAPIDLY DILUTED ENERGY DENSITY (RDED) AND ITS IMPACT COSMOLOGICAL IN THE MATTER AND TEMPERATURE POWER SPECTRUM

Abstract

Models beyond of the ΛCDM model that involve a rapid dilution at early times predict observational imprints, such as bump-like features in the power spectrum. These models with a extra energy density ρ_{ex}, motivated by phase transitions of the underlying elementary particles, dilutes at a scale factor a_c with a corresponding mode $k_c = a_c H(a_c)$ crossing the horizon at that time. The effect of such a phase transition leaves characteristic signatures in the Universe both in the expansion history, with a clear impact on the cosmological distances, as matter and CMB power spectra, which can be observed with current and future precision cosmological data. We find a bump in the matter power spectrum compared to the standard ΛCDM. We identify the amplitude, width, and time scale of the bump to the physical properties of the rapidly diluted density energy (RDED). We study these effects with linear theory, standard perturbation theory, and the correlated impact on cosmological distances, allowing for independent measurements of these extensions of the standard ΛCDM model. To generate the distinctive imprint, we use different models that work at early times well inside the radiation domination epoch, during matter domination or at late times when dark energy is the main component.

This chapter is adapted from its corresponding publication, "Cosmological signatures of a rapid diluted energy density. Axel de la Macorra, Dante V. Gomez-Navarro, Jorge Mastache,

Alejandro Aviles, Mariana Jaber, and Erick Almaraz. Phys. Rev. D 104, 023529 – Published 28 July 2021".

4.1 Introduction

Models beyond ΛCDM have been proposed for plausible explanations of the dark sector, both dark matter and dark energy, since the standard model of cosmology suffers theoretical and observational issues. For instance, models that introduces extra particles that modify the background evolution, cosmological distances, and density perturbations with a clear impact on structure formation. In this work, we consider phase transition in the dark sector generating characteristic signatures, from now on "bumps", in the matter power spectrum for modes entering the horizon around the phase transition time. We study the cosmological features of having an extra component in the Universe, $\rho_{ex}(a)$ that rapidly dilutes, faster than radiation components, at a scale factor a_c. We refer to such component as Rapid Diluted Energy Density (RDED). Different cosmological models are characterized by a RDED, like the Bound Dark Energy model (BDE) (Almaraz and de la Macorra, 2019; de la Macorra and Almaraz, 2018), where the original elementary particles (e.g quarks) form neutral massive bound states and the lightest scalar field corresponds to dark energy. We can also study the dynamics of the dark energy with a steep equation of state (SEOS) (Jaber and de la Macorra, 2018). The functional form of SEOS is motivated by the late time evolution of the BDE scalar field. In this work, we use the SEOS model as a parameterization for dark energy evolution. At the background level, the SEOS is characterized by an EoS that is always close to -1, we further assume that its perturbations are adiabatic and do not have anisotropic stresses, so we can safely neglect its perturbations inside the horizon, as it is shown in (de la Macorra and Almaraz, 2018; Almaraz and de la Macorra, 2019).. We consider also the situation when the dilution takes place in matter-dominated era, where we introduce extra cold dark matter $\rho_{ex}(a)$ for $a \leq a_c$ and we implement a RDED transition at a_c rendering $\rho_{ex}(a) \propto 1/a^6$ for $a > a_c$. To generate these distinctive imprints, we use three different transition epochs ($z_c = 10, 100$ and 1000) and with two distinct amount of matter, given by $\rho_{ex}(a_c) = 0.10\,\rho_{cdm}(a_c)$ and $\rho_{ex}(a_c) = 0.05\,\rho_{cdm}(a_c)$ as a fraction of the CDM density. The expansion rate of the Universe is affected by the RDED transition due to the change in the total energy density, consequently modifying the cosmological distances and the evolution of perturbations generating characteristic features in the matter and temperature spectra (Calabrese et al., 2011; Pogosian et al., 2005; Almaraz et al., 2020; Jaber-Bravo et al., 2020). The RDED transition affects the linear density perturbations for modes crossing the horizon just before the dilution takes place. The matter perturbations are enhanced for $k \geq k_c \equiv a_c H(a_c)$, due to the expansion of rate in the RDED-like models is greater than ΛCDM, and consequently is reflected in a higher growth rate of matter perturbations in the radiation-dominated epoch generating a bump in the matter power spectra, when we take the ratio $P_{\rm RDED}(k)/P_{\Lambda\rm CDM}(k)$. We identify the amplitude, width, and timescale of the bump to the physical properties of the transition: the amplitude

becomes related to the amount of extra energy density ρ_{ex} that dilutes, while its width, to the duration of this transition (i.e., how many modes are affected). Timescale becomes related to when the RDED transition takes place in a radiation- matter-, or dark energy-dominated universe. We note that modes with $k < k_c$ do not share this increase since the amount of energy density and background evolution are the same as in ΛCDM. We consider the extra energy density to evolve as the dominant energy density component just before the RDED transition. To study the cosmological signatures, we will consider the effect of RDED at three different epochs: radiation, matter or dark energy domination. We implement these models with the Boltzmann code CAMB[1] (Lewis et al., 2000), varying the abundance of the RDED and duration of the transition to generating bumps with different shapes. We also refer the early times models as BDE-like when the transition takes place in radiation domination epoch, DMx-like when the dilution takes place at matter-dominated era, and as SEOS-like models when they take place at late times. In all the three cases we consider that the extra component redshifts as the leading energy density component at the time of the transition. A similar bump is generated in the three cases. We derive an approximated analytic solution of the RDED bumps in the matter power spectrum and we compare the amplitude and width to the numerical implementation in CAMB. We then follow up on these features through 1-loop Standard perturbation theory (SPT) computations. The bumps in the BDE-like models are located at nonlinear scales, extending at linear scales, hence a treatment within SPT is reliable over a small interval of its full range, and we observe an boost of their amplitude and shift of their peaks toward smaller scales. Otherwise, the transition for the model SEOS-like occurs at very late times and henceforth the signatures are located at very large scales and are not affected by non-linearities. The RDED in matter domination has two different effects in the matter power spectrum. First, the growth rate of matter density increases due to the extra matter component at times before the transition, and, second, we have an increase due to the RDED after the transition. These two features coincide with BAO oscillations but nevertheless we distinguish the growth from all these sources. This chapter is organized as follows: in Sec. 3.1 we present the features to the expansion rate and the cosmological distances due to the extra energy density. In Sec. 3.2 we show how the evolution of energy density perturbations change due to the RDED and how it is reflected in the matter power spectrum $P(k)$. We present our results and details for the different models of study in Sec. 4.2. Finally, the conclusions are in Sec. 4.4.

4.2 Cosmological signatures: Numerical Results

In the previous chapter, we studied analytically cosmological models with a transition. Let us now examine numerically the RDED in radiation domination (BDE-like models), matter domination (DMx models) or dark energy domination (SEOS-like models) epochs as examples to generate bumps at different times and scales. We use a modified version of the code

[1] http://camb.info/

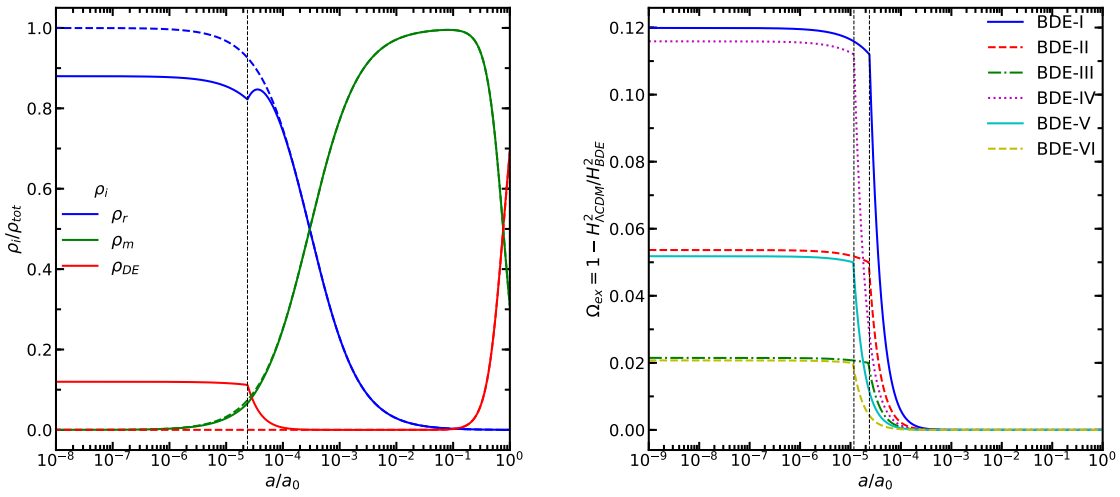

Figure 4.1: **Evolution of densities and their corresponding amount of extra energy density.** Evolution of densities of different components for BDE (solid curves) and the standard ΛCDM model (dashed curves). The left panel shows the dynamical dark energy density (red curve) of BDE-I model with a dilution at $a_c = 2.37 \times 10^{-5}$ when it contributes $\approx 11\%$ to the total density. Its contribution quickly decreases after that. The right panel shows the amount of extra energy density for BDE models described in Table 4.1. Solid blue are for BDE-I; dashed red are for BDE-II; dash-dotted green are for BDE-III; dotted magenta are for BDE-IV; solid cyan are for BDE-V; and dashed yellow are for BDE-VI. The vertical lines represent the transition redshift for each model. We note that in the BDE models we have different transitions for each model (see Table 4.1).

CAMB to produce the linear matter spectra and the different multipoles of the matter power spectrum and CMB power spectrum for transition at early times (radiation domination), matter domination and late time (dark energy domination). For all the runs, we have used a flat Universe with $\Omega_b h^2 = 0.0223$, $\Omega_c h^2 = 0.1188$, $h = 0.6775$, $\tau = 0.066$, $n_s = 0.9667$, and $\ln(10A_s) = 3.0643$, this corresponds to best parameter fit for BDE model using Planck data <. In SEOS-like models we keep the same amount of matter $\Omega_m h^2 = 0.1411$ for all models but we vary $h = 0.80, 0.68, 0.60$ giving the different amounts of $\Omega_m(a_c)$ and $\Omega_\Lambda(a_c)$. However, for models in matter domination we use $\Omega_m h^2 = 0.1434$, $h = 0.6727$ from Planck 2018 (TT,TE,EE+low E).

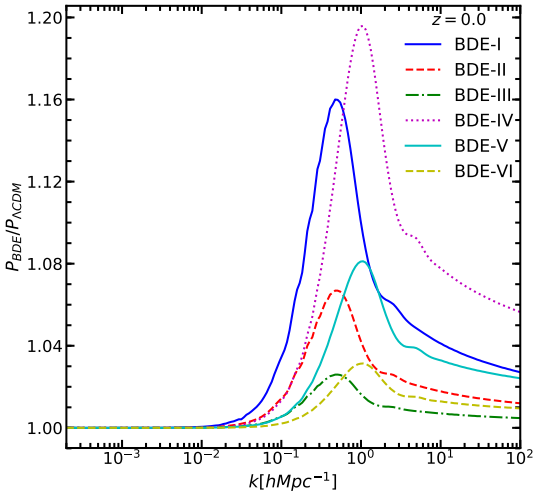

Figure 4.2: **Linear matter power spectrum transition in radiation domination.** The ratio $P_{BDE}/P_{\Lambda CDM}$ for different BDE models at $z = 0$. Solid blue are for BDE-I; dashed red are for BDE-II; dash-dotted green are for BDE-III; dotted magenta are for BDE-IV; solid cyan are for BDE-V; and dashed yellow are for BDE-VI.

4.2.1 Early times Modes: transition in radiation domination

In this section we focus on phase transitions occurring at early times, which are inspired by BDE and EDE models. In this case, the modes affected have wave-vectors $k > k_{eq}$. In table 4.1 we show the models we analyse by specifying them by a choice of $k_c \equiv a_c H(a_c)$, $\Omega^c_{ex} \equiv \Omega_{ex}(a_c)$. The evolution of energy densities of the different components as a function of the scale factor is plotted in the left panel of Figure 4.1. The contribution of extra relativistic energy density $\rho_{ex}(a)$ is indicated by red. We clearly note the transition at $a_c = 2.37 \times 10^{-5}$ and the rapid dilution of Ω_{ex} for $a > a_c$. The right panel shows the six different BDE models given in Table 4.1). We took two different modes k_c with three different abundances Ω_{ex} in each case. The value of k_c and the amount of Ω_{ex} and k_c determines the value of a_c. We notice that Ω_{ex} is constant for $a < a_c$, and after a_c a steep phase transition takes place with ρ_{ex} scaling as $\rho \propto a^{-6}$ and disappears, e.g. by factor of $\Omega_{ex} \propto (a/a_c)^{-2} \sim 1/100$ at $a/a_c = 10$ in all the models. The six BDE models, shown in the right panel, differ from each other by the dilution epoch (a_c) and the amount of extra components at the transition (Ω^c_{ex}). For instance, BDE-I and BDE-IV have the same amount of extra relativistic particles, but dilution occurs at different epoch 2.37×10^{-5} and 1.17×10^{-5}, respectively. Similarly for the BDE-II and BDE V models (both with $\Omega^c_{ex} = 0.05$) but different transition time, $a_c = 2.92 \times 10^{-5}$ and $a_c = 1.13 \times 10^{-5}$, respectively; and for the BDE-III and BDE-VI models with the same amount of extra relativistic particles, $\Omega^c_{ex} = 0.020$, and different $a_c = 2.25 \times 10^{-5}$ and $1.11 \times$

Model	k_c	$a_c[10^{-5}]$	$\Omega_{ex}(a_c)$	$R^N_{\rm L}(k_c)$	k_{min}	k_b	$k_b^{\text{1-loop}}$	$R^{\text{1-loop}}(k_b)$	$R^T_{\rm L}(k_c)$	k^T_{min}
BDE-I	0.148	2.373	0.112	1.160	0.049	0.474	0.917	1.272	1.13	0.042
BDE-II	0.148	2.292	0.050	1.066	0.082	0.474	0.917	1.110	1.05	0.065
BDE-III	0.148	2.255	0.020	1.025	0.147	0.474	0.917	1.041	1.02	0.104
BDE-IV	0.295	1.168	0.112	1.195	0.088	1.061	1.908	1.339	1.13	0.084
BDE-V	0.295	1.129	0.050	1.081	0.136	1.061	1.773	1.134	1.05	0.129
BDE-VI	0.295	1.111	0.020	1.061	1.031	0.264	1.773	1.051	1.02	0.208

Table 4.1: Small Scales - BDE-like cosmologies. We show $k_c = a_c H(a_c)$ (in hMpc^{-1}) and a_c, the mode and scale factor at the transition, $\Omega^c_{ex} \equiv \Omega_{ex}(a_c)$ the energy density ratio of ρ_{ex}. We show $R^T_{\rm L}(k_c)$, $k^T_{min}(k_c)$ the ratio of power spectra eq.(4.2.1) and eq.(3.41), respectively while $R^N_{\rm L}(k_c)$, $k^T_{min}(k_c)$ correspond to the numerical estimation of the same quantities. While $k_b^{\text{1-loop}}$ is the mode at the maximum of the bump at a linear and one-loop level respectively, with $R^N_{\rm L}(k_b)$ and $R^{\text{1-loop}}$ correspond to the ratio of the power spectra. We consider $h = 0.677$, $\Omega_m = 0.307$ for all bumps and a late time ΛCDM cosmology.

10^{-5}, respectively. At late time, the amount of extra relativistic particles is negligible, which reproduces a cosmological constant behaviour. In section 4.3 we present the effects of the extra relativistic particles on the CMB and matter power spectra.

Matter Power Spectrum: transition in radiation domination

In Fig. 4.2, we plot the ratio of the matter power spectra $P_{\rm BDE}/P_{\Lambda\rm CDM}$, where we clearly see a bump corresponding to a wave-number of the order of k_c. We show the six BDE models in Table 4.1 with solid blue for BDE-I; dashed red for BDE-II; dash-dotted green for BDE-III; dotted magenta for BDE-IV; solid cyan for BDE-V; and dashed yellow for BDE-VI.

We see that or small scales, $k > k_c$, the deviation in the matter power spectrum between ΛCDM and BDE is significant, peaking at mode k_b which is of the order of k_c. Although, well after the transition takes place, corresponding to modes $k \ll k_c$, both models (ΛCDM and BDE) have the same H and the ratio $P_{\rm BDE}/P_{\Lambda\rm CDM} \sim 1$.

The dynamics of BDE produces the deviations at scales $k \geq k_c$, and we can see the imprint left by the RDED for modes entering the horizon before a_c. The initial suppression of the linear evolution is even reversed by the RDED and a bump is generated at a linear level. The BDE models in Table 4.1 peak at $k_{b_L} = 0.474\,h$Mpc^{-1} for models BDE I, II and III with a $k_c = 0.148\,h$Mpc^{-1}, while $k_{b_L} = 1.061\,h$Mpc^{-1} for models BDE IV,V and VI, with and $k_c = 0.295\,h$Mpc^{-1}.

The amount of the diluted component Ω_{ex} is correlated to the magnitude of the enhancement. For instance, the case of BDE-I with $\Omega^c_{ex} = 0.112$ has a bump increased at its peak by 16%, while BDE-II (BDE-III) have an enhancement of 6.68% (2.5%), respectively. A similar pattern results for the BDE IV, V, and VI models. Otherwise, the position of the

peak of the bump given by k_{b_L} is shifted to smaller scales, from $k_c = 0.148\,h\mathrm{Mpc}^{-1}$ to $k_{b_L} = 0.917\,h\mathrm{Mpc}^{-1}$ and from $k_c = 0.295\,h\mathrm{Mpc}^{-1}$ to $k_{b_L} = 1.061\,h\mathrm{Mpc}^{-1}$.

Table 4.1 shows the numerical and analytical results of the ratio of power spectra R_L^N at the maximum of the bump and the width of the bump estimated by $\Delta k = k_c - k_{min}$. We note that there is an agreement between the analytic solutions to the bump amplitude given in eq.() and the width determined by $\delta k = k_{max} - k_c$ from eq.(3.41), they differ within a few tens of %. We suggest that the simple analytic scheme encodes the physics of the dilation showing that the bump is a consequence of RDED.

However, the modes are no longer in the linear regime at present time due to these cross the horizon at early times. For this reason, in section 4.2.4 we use non-linear Standard Perturbation Theory (SPT) (see, e.g. (Bernardeau et al., 2002b)) to analyse how much of this discrepancy is expected to be seen when we take into account the quasi-linear effects. Fig. 4.2 shows this last effect in the matter power spectrum.

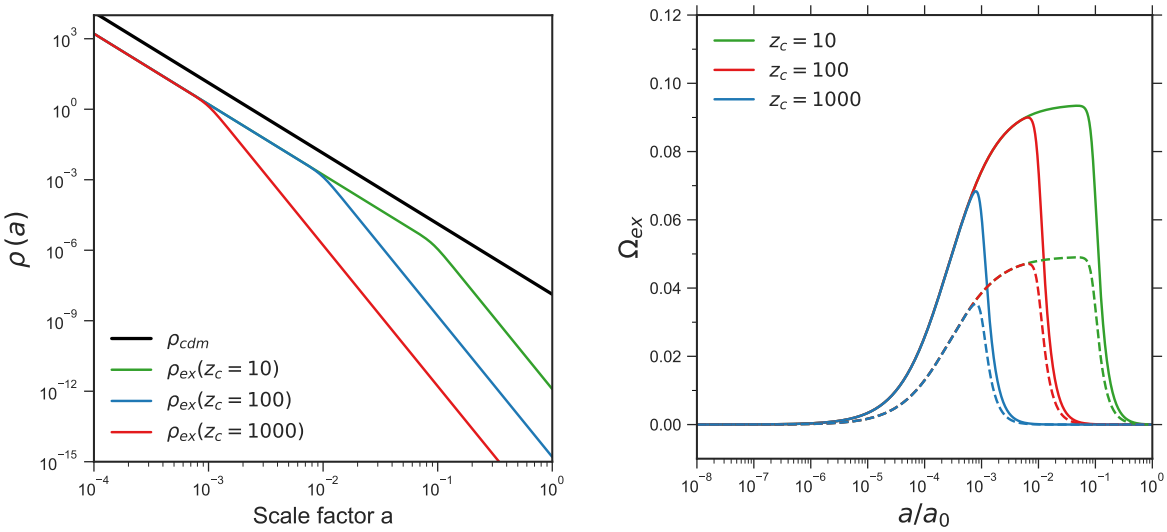

Figure 4.3: **Background evolution of different fluids. Transition in the matter dominated epoch.** The left panel: Plot of the evolution of densities of different components as function of the scale factor, a/a_0, for a model with an extra fluid that dilutes at the mater-dominated epoch (solid lines) and the standard ΛCDM model (dashed lines). The left panel shows the evolution of the Ω_{ex} parameter for the extra fluid for different transitions, $z_c = 10, 100, 1000$ for green, red, and blue lines, respectively. Continuous (dashed) lines corresponds to the case where $\Omega_x(a_c) = 0.1\,\Omega_c(a_c)$ ($\Omega_x(a_c) = 0.05\,\Omega_c(a_c)$).

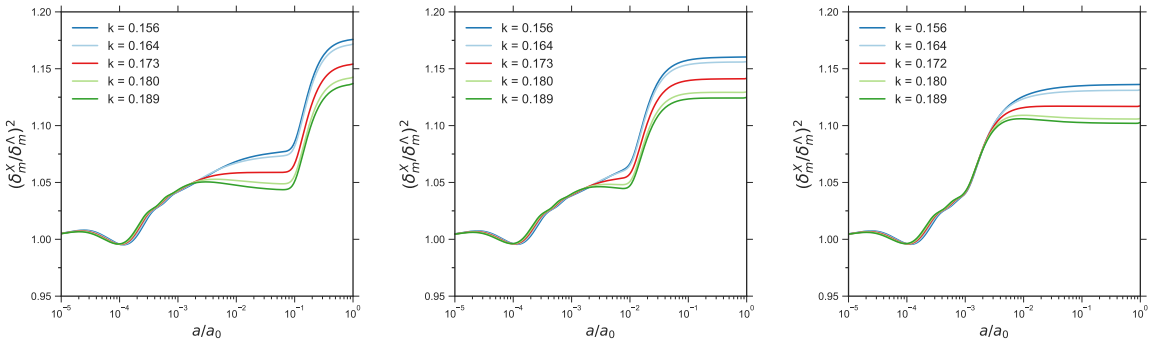

Figure 4.4: **Evolution of matter density perturbation with transition in matter domination.** We show the squared of the ratio of matter perturbations $(\delta_m^X/\delta_m^\Lambda)^2$ for different modes k (in $h\text{Mpc}^{-1}$) with $\Omega_x(a_c) = 0.1\Omega_{\text{cdm}}(a_c)$. Left, middle and right panels corresponds to different transition values $z_c = 10, 100, 1000$, respectively. The ranges of modes are chosen to map a complete baryon acoustic oscillation between the third peak and third trough. We can see two interesting effects. First we see an increase in power due to the extra matter $\Omega_{ex}(a)$ for $a < a_c$ and we also notice the effect of RDED for $a > a_c$ with a steep increase in power in the evolution of $\delta_m^X/\delta_m^\Lambda$ due to the rapid dilution of ρ_{ex}.

4.2.2 Transition in matter domination. Evolution and Matter power spectrum

Here we consider the extra energy density ρ_{ex} as cold dark matter ($\rho_{ex} \propto a^{-3}$ for $z > z_c$) while it dilutes as $\rho_{ex} \propto a^{-6}$ after the transition takes place at $a_c = 1/(1+z_c)$, see Fig.4.3. We consider three different transitions epochs $z_c = 10, 100, 1000$, and in each transition we take two amounts of extra energy density $\Delta\Omega_{ex}^c = 0.1$ and $\Delta\Omega_{ex}^c = 0.05$, with $\Delta\Omega_{ex}^c \equiv \Omega_{ex}(z_c)/\Omega_{cdm}(z_c) = \rho_{ex}(z_c)/\rho_m(z_c)$. We plot in Fig.4.3 the evolution of $\Omega_{ex}(a)$, and for large z (i.e. model with $z_c = 1000$) radiation is no longer subdominant and must be taken into account in determining $\Omega_{ex}(a_c)$.
The ratio of matter perturbations $\delta_m^X/\delta_m^\Lambda$ for different modes are shown in Figs. 4.4 and 4.5 for different modes k with $\Omega_{ex}(a_c) = 0.1\,\Omega_{\text{cdm}}(a_c)$ and $\Omega_{ex}(a_c) = 0.05\,\Omega_{\text{cdm}}(a_c)$, respectively. Left, middle and right panels corresponds to different transition values $z_c = 10, 100, 1000$, respectively.
The ranges of modes are chosen to map a half baryon acoustic oscillation between the third peak and third damp in the power spectrum shown in Fig. 4.6.
Notice that for the cases with $z_c = 10, 100$ in Figs. 4.4 and 4.5 we find a dispersion of the amplitude of the different modes in P_X/P_Λ at a_c. This dispersion is a related to the BAO oscillations and takes place in the range $1000 > z > 100$. In the case $z_c = 1000$ there is no dispersion in P_X/P_Λ at a_c.
We can clearly see two interesting effects in the evolution of $\delta_m^X/\delta_m^\Lambda$. First we notice an

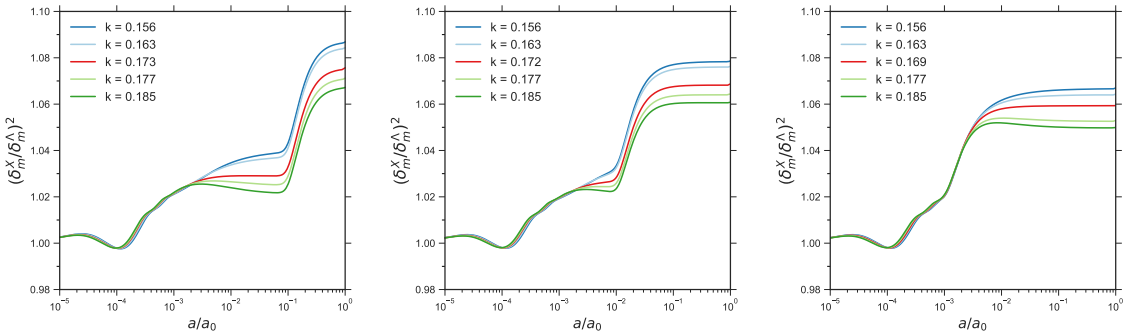

Figure 4.5: **Evolution of matter density perturbation with a RDED transition in matter domination.** Plot of the ratio of the squared of matter perturbations $\delta_m^X/\delta_m^\Lambda$ for different modes k (in $h\mathrm{Mpc}^{-1}$ units) with $\Omega_x(a_c) = 0.05\Omega_{\mathrm{cdm}}(a_c)$. Left, middle and right panels corresponds to different transition values $z_c = 10, 100, 1000$, respectively. The ranges of modes are chosen to map a half baryon acoustic oscillation. The ranges of modes are chosen to map a complete baryon acoustic oscillation between the third peak and third trough. We can see two interesting effects. First we see an increase in power due to the extra matter $\Omega_{ex}(a)$ for $a < a_c$ and second we notice the effect of RDED for $a > a_c$ with a steep increase in power in the evolution of $\delta_m^{/}\delta_m^\Lambda$ due to the rapid dilution of ρ_{ex}.

increase in power due to the extra matter $\Omega_{ex}(a)$ for $a < a_c$ and secondly we have a steep increase in power starting at a_c due to the RDED of ρ_{ex} for $a \geq a_c$. These graphs clearly distinguish the contribution from the extra matter $\rho_{ex}(a)$ for $a < a_c$ and the increase due to RDED for $a > a_c$.

The overall change in the matter power spectrum is shown in Fig. 4.6. Notice that defining a peak of the bump is in this case not trivial due to the presence of the BAO wiggles. We therefore define the bump peak, k_b, as the middle point between the third peak of the oscillation and the third damp. The values k_b are shown in Table 4.2 and corresponds to modes of the order of $k_b \sim 0.173 \times 10^{-3}\, h\mathrm{Mpc}^{-1}$.

Notice that modes $k > k_c$ enter before a_c enter the horizon with $\rho_{ex} > 0$ have an increase in power compared to ΛCDM due to the extra ρ_{ex} and they also undergo the RDED at a_c. Therefore the amplitude of each mode $k > k_c$ in the matter power spectrum is combination of these two effects. The overall effect in the matter power spectrum is an increase in power of 15%, and 8%, for models having a transition at $z_c = 10$, and $\Omega_{ex}(a_c)/\Omega_m(a_c) = 0.1$ or 0.05, respectively. For modes $k > k_c$ the increases due to the rapid dilution is up to 9% (4%) for the case $\Omega_{ex}/\Omega_m = 0.1$ (0.05), the remaining 7% difference corresponds to the existence of the extra matter ρ_{ex} for $a < a_c$. On the other hand modes $k < k_c$ enter the horizon after the transition have no change in the matter power spectrum at those scales and we obtain $P_X/P_\Lambda = 1$ in Fig. 4.6. We show in Table 4.2 the cosmological parameters including the value of $k_c \equiv a_c H(a_c)$, k_b and the ratio of P_X/P_Λ at different relevant epochs, including the

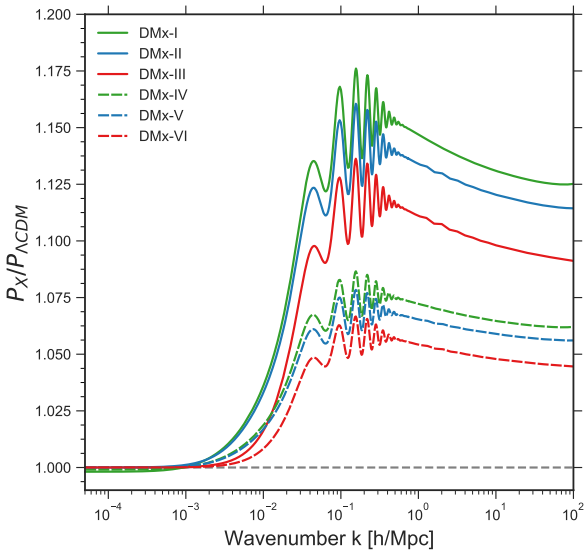

Figure 4.6: **Matter Power Spectrum for DMx. Transition in matter domination.** The matter power spectrum ratio $P_x/P_{\Lambda CDM}$. The transition takes at $0.4 < k_c \times 10^3\, h^{-1}\text{Mpc} < 4$ with a maximum at $k_b \simeq 1.15 k_c$ (c.f. eq.(3.53)).

increase of P_X/P_Λ between a_c and a_o, which is due to the RDED of the extra matter ρ_{ex}, for the different cases.

4.2.3 Late Time Models

Here we present the case where the transition takes place at late times and the dark energy is modelled as a barotropic fluid, where its dynamics is parameterized in terms of an Steep Equation of State ("SEOS") (Jaber and de la Macorra, 2018)), $w(z)$:

$$w(z) = w_0 + (w_i - w_0)\left(\frac{(z/z_c)^q}{1+(z/z_c)^q}\right), \tag{4.1}$$

where w_i, w_0, z_c and q are free parameters, with $z_c > 0$ and a finite value of q. In this case we have a RDED transition occurring at late times given by the redshift z_c and are due to the evolution of the dynamical the dark energy model. The evolution of Dark Energy evolves from w_i for $z \gg z_c$ and has a transition from w_i to $w_0 = w(z=0)$ at a redshift z_c with an EoS $w(z_c) = (w_i - w_0)/2$. A best fit value $w_0 = -0.93$ and was obtained in SEOS (Jaber and de la Macorra, 2018) motivated by BDE (de la Macorra and Almaraz, 2018) model.

A cosmological constant $w \equiv -1$ can be recovered using Eq. (4.1) setting $w_0 = w_i = -1$ for all z and independent of the values of z_t, and q. Left panel in Fig. 4.7 shows the evolution of the energy densities of different components, including the corresponding amount of dark

Model	z_c	$\Delta\Omega^c_{ex}$	$\widetilde{\Omega}^h_{ex}$	$\widetilde{\Omega}^c_{ex}$	$k_c \times 10^3$	$R^T_b(a_0)/R^T_b(a_c)$	$R^N_b(a_0)/R^N_b(a_c)$	k^N_b	$R^N_b(a_0)$	k^{1-loop}_b	R^{1-loop}_b
DMx-I	10	0.10	0.0069	0.0915	0.649	1.07	1.086	0.173	1.154	1.673	1.307
DMx-II	100	0.10	0.0094	0.0817	1.980	1.06	1.079	0.173	1.142	1.673	1.280
DMx-III	1000	0.10	0.0093	0.0647	6.924	1.05	1.073	0.172	1.117	1.673	1.232
DMx-IV	10	0.05	0.0051	0.0461	0.636	1.04	1.044	0.173	1.076	1.673	1.145
DMx-V	100	0.05	0.0046	0.0408	1.942	1.03	1.040	0.172	1.069	1.673	1.131
DMx-VI	1000	0.05	0.0047	0.0324	6.818	1.02	1.038	0.169	1.059	1.673	1.108

Table 4.2: Table with the cosmological parameters of the DMx model. The columns from left to right are: (1) z_c, the redshift when the transition occurs. (2) The amount of extra matter at the moment of the transition $\Delta\Omega^c_{ex} \equiv \Omega_{ex}(a_c)/\Omega_m(a_c)$, (3) and (4) the amount of extra matter $\widetilde{\Omega}_{ex}(a)$ (c.f. eq.(3.7)) $\widetilde{\Omega}^c_{ex} = \widetilde{\Omega}_{ex}(a_c)$ and $\widetilde{\Omega}^h_{ex} = \widetilde{\Omega}_{ex}(a_h)$, respectively. (5) $k_c \equiv a_c H(a_c)$, the mode at the transition. (6) The theoretical estimation of $R^T_b(a_0)/R^T_b(a_c)$ corresponding to the ratio of the density matter perturbation $R(a) = P_X(a)/P_\Lambda(a)$ at a_c and at present time a_0 (c.f. eq.(3.52)), (7) The numerical estimation of (6). (8) k_b the maximum of the bump, defined as the middle point between the third peak and third damp in $R(a_0)$. (9) The ratio of the linear density matter perturbation at present time. (10) and (11) Same as (8) and (9) considering one-loop contribution, respectively.

energy at different redshifts for the SEOS model. The evolution of $\Omega_i = \rho_i/\rho_{tot}$ for SEOS-I model with $q = 2$, $\Omega_{de}(a_0) = 0.78$, $h = 0.80$ and for ΛCDM, are shown in the left panel.

The EoS in Eq. (4.1) allows for a steep transition from w_i to w_0 taking place at a central redshift value z_c with a steepness determined by the parameter q. The effect of the dynamical dark energy in SEOS model is seen in the right panel of Fig. 4.7 where the parameter q modulates the steepness of the transition, a larger q has a steeper transition. We show in table 4.3 and in Fig. 4.7 different SEOS models where we take as examples the values of $q = 2$ and $q = 10$ and we allow for different amount of $\Omega_{de}(a_0)$ at present time. A larger value of q has a steeper transition, originating a narrower bump for $q = 10$ in models SEOS-II, SEOS-IV, and SEOS-VI models, while broader bump is generated for $q = 2$ in SEOS-I, SEOS-III and SEOS-V models. Comparing models with the same amount of $\Omega_{de}(a_0)$ we notice that SEOS-II increases the enhancement of the bump compared to SEOS-I in table 4.3. The same happens when we compare model SEOS-IV with SEOS-III and model SEOS-VI with SEOS-V. To conclude, a steeper bump (larger q) shifts the peak to later times and increases the amount of extra energy density $\Omega_{ex}(a_c)$.

Matter Power Spectrum: transition at late times in Dark Energy domination

We see that SEOS impacts the evolution of matter perturbations mainly at late times when the DE density is non-negligible. We take SEOS as a model-independent smooth DE component, meaning that $\delta\rho_{ex} = 0$, since we are interested in parameterizing the dynamics of DE. We take SEOS as a model for a smooth DE component, meaning that the extra energy density

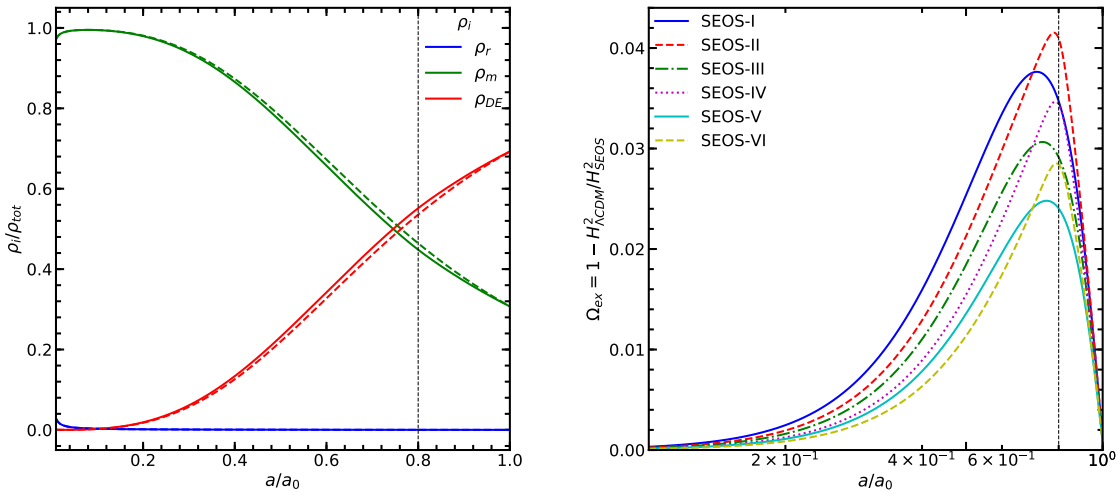

Figure 4.7: **Evolution of densities and their corresponding amount of extra energy density ρ_{ex}.** Left panel: Evolution of densities of different components for SEOS-I model (solid curves) and the standard ΛCDM model (dashed curves) with a dilution at $a_c = 0.8$ ($z_c = 0.25$). Blue curves are for radiation density; green curves are for matter density; and red curves are for dark energy density. The right panel shows the amount of extra energy density for SEOS models described in Table 4.3. Solid blue are for SEOS-I; dashed red are for SEOS-II; dash-dotted green are for SEOS-III; dotted magenta are for SEOS-IV; solid cyan are for SEOS-V; and dashed yellow are for SEOS-VI. The vertical lines represent the transition scale factor $a_c = 1/(1+z_c) = 0.8$.

fluctuations are negligible for modes well inside the horizon, which finds justification if one assumes adiabatic perturbations and no anisotropic stresses, since the EoS parameter always lie in the interval $w \in [-1, -0.9]$. In chapter 3 we present scalar field models which render the SEOS DE dynamics and the perturbations do not cluster. We show in Fig. 4.8 the effects of SEOS in the matter power spectra, where we display the ratio with respect to ΛCDM for the SEOS models presented in table 4.3. We work in all six models with the same amount of matter $\Omega_m h^2 = 0.14$.

In the left panel we show the ratio $P_{\rm SEOS}(k)/P_{\Lambda\rm CDM}(k)$ for different redshift values ($z = 0, 0.1, 0.2, 0.25, \text{and}, 5$) for SEOS-IV model. Blue curves are for $z = 0$; red curves are for $z = 0.1$; green curves are for $z = 0.2$; magenta curves are for $z = 0.25$; and cyan curves are for $z = 5.0$. In the right panel we show the same ratio for different models varying the quantity of matter and rate of expansion (see Table 4.3 IV A 1). Blue curves are for SEOS-I; red curves are for SEOS-II; green curves are for SEOS-III; magenta curves are for SEOSIV; cyan curves are for SEOS-V; and yellow curves are for SEOS-VI.

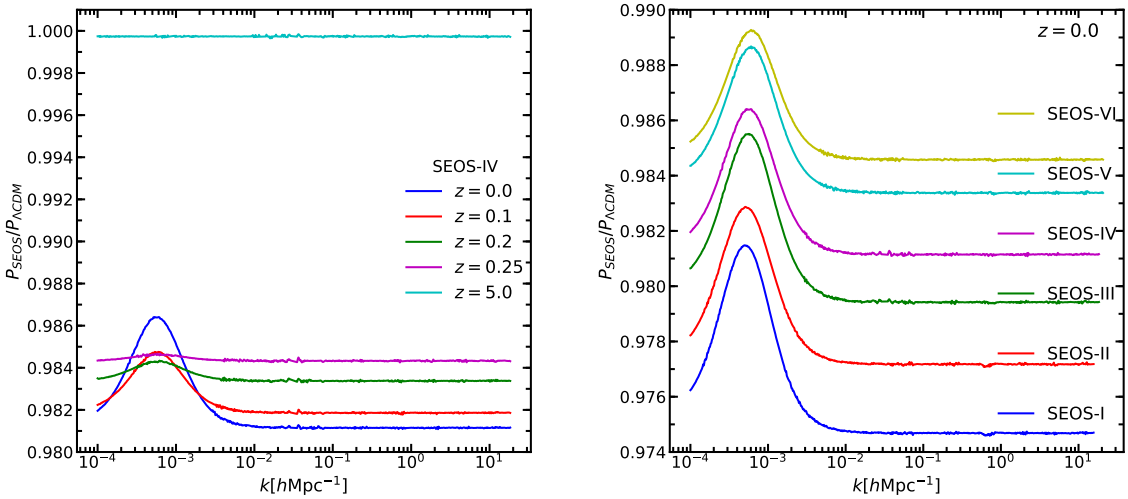

Figure 4.8: **Linear matter power spectrum transition at late times.** The left panel: the ratio $P_{\rm SEOS}/P_{\Lambda\rm CDM}$for model SEOS-IV. Blue curves are for $z = 0.0$; red curves are for $z = 0.1$; green curves are for $z = 0.2$; magenta curves are for $z = 0.25$; and cyan curves are for $z = 5.0$. The right panel: The ratio $P_{\rm SEOS}/P_{\Lambda\rm CDM}$ for different models at $z = 0$. Blue curves are for SEOS-I; red curves are for SEOS-II; green curves are for SEOS-III; magenta curves are for SEOS-IV; cyan curves are for SEOS-V; and yellow curves are for SEOS-VI (see Table4.3).

At redshift $z = 5$, during the Einstein-de Sitter phase, matter perturbations have almost the same amplitude as in ΛCDM at all scales, the overall normalization is due to slight different rate of expansions.

This overall suppression is due to faster expansion rate in ΛCDM than in SEOS since the EoS is always larger than for cosmological constant , i.e $w_{SEOS} > -1$. We also notice that the overall suppression increases with time when DE starts to dominate. However, once the RDED in SEOS takes place at $a_c = 0.8$ $(z_c = 0.25)$ with a corresponding mode $k_c = a_c H(a_c) \simeq 3 \times 10^{-4}\, h\text{Mpc}^{-1}$ it generates bump in the ratio of power spectra with a maximum at sligthly smaller scales at $k_b \simeq 5.5 \times 10^{-4}\, h\text{Mpc}^{-1}$.

In the left panel of fig.(4.8) we see snapshots of the quotient of the matter power spectrum at different values of z. Clearly the bump is generated after the transition takes place at $z_c = 0.25$, i.e for $z \leq z_c$. The evolution of the bump increases as $z \to 0$. While in the right panel of fig.(4.8) we see that the impact of the rapid dilution energy density appears for modes $k \geq k_c$ entering the horizon slightly before the transition occurs at $a_c = 0.8$. with $k_c = a_c H(a_c) = 3.27 \times 10^{-4}\, h\text{Mpc}^{-1} = 2.22 \times 10^{-4}$ Mpc^{-1} for SEOS-IV model.

Notice that the amount of matter $\rho_m(a_0)$ is the same in all models in table 4.3 and it is

Model	w_0	w_i	z_c	q	Ω_{ex}^c	$k_c \times 10^4$	h	Ω_m^0	$k_b \times 10^4$	$R_L^N(k_c)$	$k_{max}^N \times 10^3$	$R_L^T(k_c)$	$k_{max}^T \times 10^4$
SEOS-I	-0.9	-1	0.25	2	0.035	3.19	0.80	022	4.95	1.0059	2.76	1.0048	6.761
SEOS-II	-0.9	-1	0.25	10	0.041	3.21	0.80	0.22	5.15	1.0047	2.71	1.0057	6.250
SEOS-III	-0.9	-1	0.25	2	0.029	3.25	0.68	0.31	5.58	1.0049	2.94	1.0046	6.299
SEOS-IV	-0.9	-1	0.25	10	0.034	3.27	0.68	0.31	6.05	1.0040	2.71	1.0055	5.820
SEOS-V	-0.9	-1	0.25	2	0.024	3.32	0.60	0.39	6.05	1.0041	2.82	1.0042	5.927
SEOS-VI	-0.9	-1	0.25	10	0.028	3.33	0.60	0.39	6.05	1.0034	2.61	1.0050	5.474

Table 4.3: Large Scales - SEOS cosmology. We present the values of the EoS parameters w_0, w_i z_c, q, with $\Omega_{ex}^c \equiv \Omega_{ex}(a_c)$ for a transition mode $k_c \equiv a_c H(a_c)$ in $h\text{Mpc}^{-1}$ at a scale factor $a_c = 0.8$ with k_b in $[h\text{Mpc}^{-1}]$ is the mode at the maximum of the bump, $R_L^N(k_c) = P_{\text{SEOS}}(k_c)/P_{\text{SEOS}}(\text{base})$, k_{max}^N corresponds to the numerical estimation $R_L^N(k_c)$ and the theoretical estimation $R_L^T(k_c)$ (c.f. eq.(3.70)) of the amplitude at the mode k_c, while k_{max}^N k_{max}^T correspond with an of 1% amplitude of the mode k_c, allowing us to have a model independent measurement of the width of the bump. In all models we considered the same amount of matter $\Omega_m h^2 = 0.141$.

the dynamics of the DE component what decreases the amplitude by the same amount for all modes, as compared to a ΛCDM model.

However, the impact on the evolution of the matter perturbations due to the RDED generates the bump seen at $k \sim 5\,h\text{Mpc}^{-1}$. In fact, we can isolate the effects of the background expansion and growth of fluctuations by looking at the spectra at late times, when DE is dominant. For instance, at $z = 0.25$ the spectrum in SEOS is suppressed by 1.6% on all scales due to the late-time dynamics of DE, but this suppression is overwhelmed on large scales by the enhancement effect due to SEOS rapid dilution at $z_c = 0.25$, which lead to a small excess of power at $k_b = 6.049 \times 10^{-4}\,h\text{Mpc}^{-1}$. At smaller redshifts, the spectra continue to decline overall, but increasing at the bump location.

We see in table (4.3) the analytic solutions to the bump amplitude given in eq.(3.70) has an excellent agreement with the numerical calculations (below 1%) while the estimation of the width determined by $\delta k = k_{max} - k_c$ and determined by eq.(3.72) agrees with the order of magnitude.

Finally it is worth remarking that SEOS and ΛCDM share the same set of cosmological parameters $h, \Omega_m h^2$ at present time, however the evolution differs due to the EoS in eq.(4.1). Higher values of q enhanced slightly the amplitude of bump and increases the value of $k_{b,L}$. Finally we remark that $k_{b,L}$ is of the same order as k_c but slightly shifted to smaller scales, as described in the analytic presentation in section 3.2.

The cosmic microwave background spectra for BDE cosmologies, with transition in radiation domination. The ratio $\mathscr{C}_{l,\text{BDE}^{TT}}/\mathscr{C}_{l,\Lambda\text{CDM}}$.

Model	k_c	$a_c[10^{-5}]$	Ω^c_{ex}	$z_\star$	$r_s(z_\star)$	$D_A(z_\star)$	$100\times\theta(z_\star)$
BDE-I	0.148	2.373	0.112	1089.68	144.16	13.928	1.03499
BDE-II	0.148	2.292	0.050	1089.68	144.54	13.928	1.03776
BDE-III	0.148	2.255	0.020	1089.68	144.71	13.928	1.03898
BDE-IV	0.295	1.168	0.112	1089.69	144.48	13.928	1.03730
BDE-V	0.295	1.129	0.050	1089.69	144.68	13.928	1.03873
BDE-VI	0.295	1.111	0.020	1089.68	144.77	13.928	1.03936

Table 4.4: We show the values of the acoustic scale $r(z_\star)$, angular diameter distance $D_A(z_\star)$ (in hMpc^{-1}) and angle $\theta(z_\star)$ for the different BDE-like models. Since in these cases $\Omega_{ex}=0$ for $z<z_\star$ the angular diameter distance is the same while we have a small deviations in $\theta(z_\star)$ and $r_s(z_\star)$.

Model	z_c	$\Omega_{ex}(a_c)$	$k_c\times10^3$	$z_\star$	$r_s(z_\star)$	$D_A(z_\star)$	$100\times\theta(z_\star)$
DMx-I	10	0.061	0.441	1090.02	140.59	12.495	1.03128
DMx-II	100	0.076	1.348	1089.94	140.90	12.680	1.01853
DMx-III	1000	0.084	4.718	1089.83	140.95	12.733	1.01479
DMx-IV	10	0.031	0.432	1090.02	142.49	12.616	1.03574
DMx-V	100	0.039	1.323	1089.94	142.67	12.713	1.02916
DMx-VI	1000	0.044	4.645	1089.83	142.70	12.740	1.02722

Table 4.5: We show the values of the acoustic scale $r(z_\star)$, angular diameter distance $D_A(z_\star)$ (in hMpc^{-1}) and angle $\theta(z_\star)$ for the different DMx with a transition in matter domination.

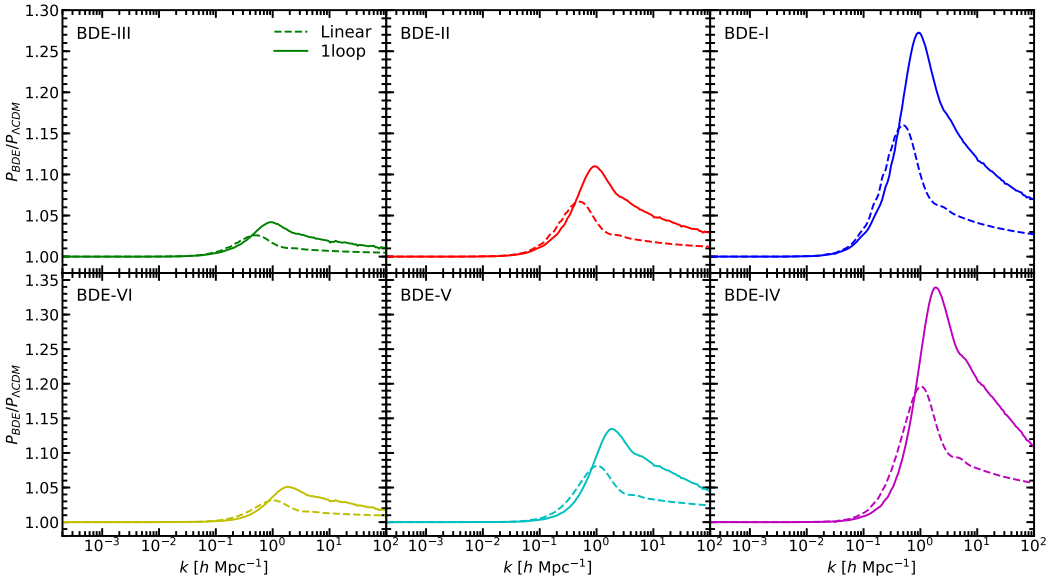

Figure 4.9: **The 1-loop and linear power spectrum for BDE cosmologies with a transition at early times.** We show the ratio $R(k) = P(k)_{\rm BDE}/P(k)_{\Lambda\rm CDM}$ at $z = 0$ at a linear (dashed) and one-loop level (solid). Top left: the BDE-III model; top middle: the BDE-II model; top right: the BDE-I model; bottom left: the BDE-VI model; bottom middle: the BDE-V model; bottom right: the BDE-IV model. Full curves are for 1-loop power spectrum; and dashed curves are for linear theory.

Solid blue curves are for BDE-I; dashed red curves are for BDE-II; dashed-dotted green curves are for BDE-III; dotted magenta curves are for BDE-IV; solid cyan are for BDE V; and dashed yellow are for BDE-VI.

4.2.4 Nonlinear evolution in SPT

In this section we compute the non-linearities in the power spectrum for BDE and DMx models using 1-loop SPT. For this we use the publicly available code `MGPT`[2] (Aviles and Cervantes-Cota, 2017; Aviles et al., 2018) that accounts for a background evolution different than ΛCDM.

We work out only the BDE and DM-x models since these have the bumps located at quasi-linear and non-linear scales. In turn, the SEOS the transition modes enter at very late times and henceforth the signatures are located at very large scales and are not affected by non-

[2]https://github.com/cosmoinin/MGPT

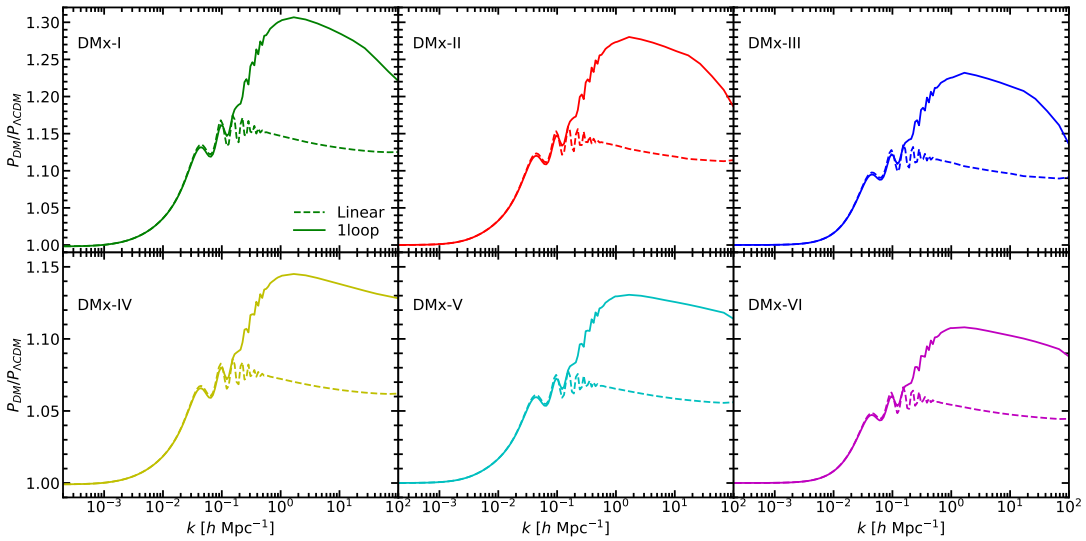

Figure 4.10: **The 1-loop and linear power spectrum for DMx cosmologies with a transition at intermediate times.** We show the ratio $R(k) = P(k)_{\rm BDE}/P(k)_{\Lambda\rm CDM}$ at $z = 0$ at a linear (dashed) and one-loop level (solid). Top left: the DMx-I model; top middle: the DMx-II model; top right: the DMx-III model; bottom left: the DMx-IV model; bottom middle: the DMx-V model; bottom right: the DMx-VI model. Full curves are for 1-loop power spectrum; and dashed curves are for linear theory.

linearities. In Fig. 4.9 and Fig. 4.10 we show the ratios $R(k) = P(k)_{\rm BDE}/P(k)_{\Lambda\rm CDM}$ for the different models. Solid curves are for 1-loop power spectrum and dashed curves are for linear theory. We show that the perturbative 1-loop affects the intermediate scales and small scales.

The 1-loop power spectrum of BDE-I, BDE-II, and BDE-III has a bump contributing 27.2%, 11.0%, and 4.10% to the power spectrum at $k = 1.67\,h\mathrm{Mpc}^{-1}$, respectively. A similar pattern of results was obtained for the BDE-IV, BDE-V, and BDE VI models whose contribute 33.9%, 13.4%, and 5.10% to the power at $1.908\,h\mathrm{Mpc}^{-1}$, $1.773\,h\mathrm{Mpc}^{-1}$, and $1.773\,h\mathrm{Mpc}^{-1}$, respectively. On the other hand, the 1-loop power spectrum of DMx-I, DMx-II, DMx-III, DMx-IV, DMx-V, and DMx-VI has a bump contributing 30.7%, 28.0%, 23.2%, 14.5%, 13.06%, and 10.8% to the power spectrum at $k = 1.673\,h\mathrm{Mpc}^{-1}$, respectively.

The behavior of the nonlinear features are not directly related to the physics of the BDE-like models, but to the linear power spectra themselves. To explore it, we choose to use the BDE-I model since as shown in Fig. 4.2, this is the model that has the bump at more yet linear scales, showing differences with the ΛCDM even at very large scales. In Fig. 4.11 we plot the linear and non-linear spectra of both BDE-I and ΛCDM. We notice that loop corrections continue to enhance the SPT power spectrum beyond the scale $k_b \simeq 0.474\,h\,\mathrm{Mpc}^{-1}$, which is

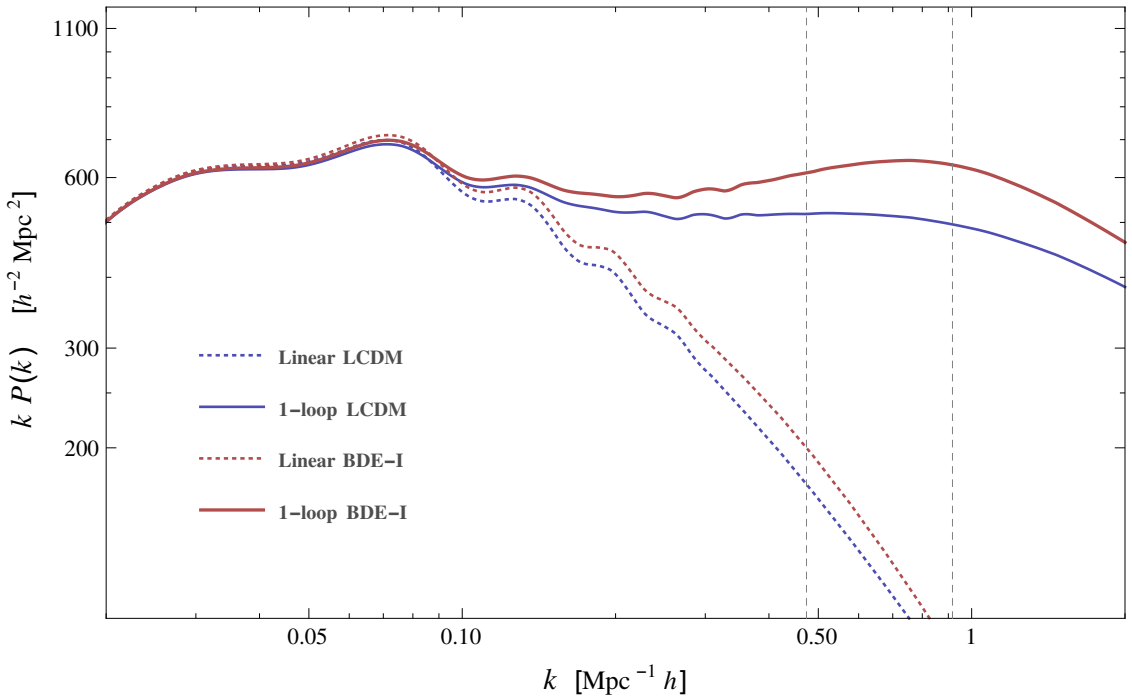

Figure 4.11: Linear and non-linear power spectra for models BDE-I and ΛCDM. Vertical dashed lines denote the location of the maximum amplitude of the bumps in linear ($k_b = 0.474\,h\,\mathrm{Mpc}^{-1}$) and non-linear ($k_b = 0.917\,h\,\mathrm{Mpc}^{-1}$) spectra, as reported in Table 4.1. The net effect of non-linearities is a larger enhancement of the 1-loop power spectrum of the BDE model compared to ΛCDM and a shift of the maximum of the bump.

the maximum of the bump in the linear power spectra ratio as reported in Table 4.1, because the power of BDE-I is always greater than in ΛCDM and nonlinar corrections goes as $\mathscr{O}(P_L^2)$. This cannot continue indefinitely since eventually, at sufficiently small scales, the power on the two models are small enough and have no influence in loop integrals, which happens at the turnaround of the non-linear bump. As a result, we notice that nonlinearities tend to shift the peak of the bumps to smaller scales and enhance their amplitudes with respect to the linear theory.

4.3 CMB Power Spectrum

We present the impact of RDED in the CMB power spectrum with a RDED transition in radiation domination (BDE-like), matter domination and dark energy domination (SEOS-like) epochs.

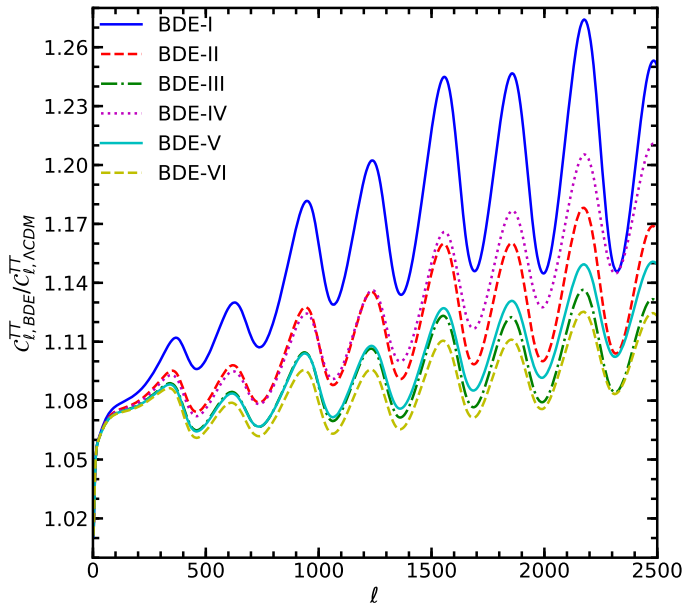

Figure 4.12: **The cosmic microwave background spectra for BDE cosmologies. Transition in radiation domination**. The ratio $\mathscr{C}_{l,\mathrm{BDE}}^{TT}/\mathscr{C}_{l,\Lambda\mathrm{CDM}}$. Solid blue curves are for BDE-I; dashed red curves are for BDE-II; dashed-dotted green curves are for BDE-III; dotted magenta curves are for BDE-IV; solid cyan are for BDE V; and dashed yellow are for BDE-VI.

4.3.1 CMB Power Spectrum

We show the temperature power spectrum of the CMB for different BDE cosmologies in Fig. 4.12, where we plot the ratio $C_{\ell,BDE}^{TT}/C_{\Lambda CDM}^{TT}$. An increase in the amount of radiation at early times, before recombination, can be seen to affect the CMB: an angular shift to higher ℓs, an enhancement in the amplitude, and a change in the damping scale.

Having an extra radiation term in this model shifts the CMB peaks. It is well known (Hu et al., 1995) that the angular position of the oscillations peaks are located at the extrema of the oscillations given by $kr_s(a_*)$, where $r_s(a_\star)$ is the sound horizon at last scattering, given in Eq. (3.9), which depends on the expansion rate H. Because we increase the radiation content before the last scattering, for $a < a_c < a_*$, the expansion rate is increased (see Eq. (3.28)) making the scattering surface thinner in BDE cosmologies than in ΛCDM. Thus, slightly shifting the peaks of the oscillation to higher ℓs.

The amplitude of the CMB peaks depends on the matter-radiation ratio, therefore it relies

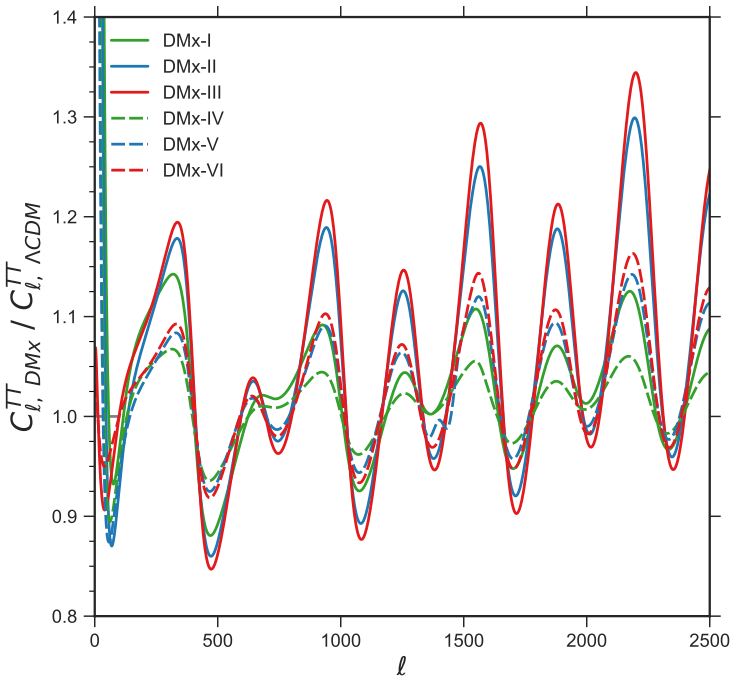

Figure 4.13: **The cosmic microwave background spectra for DMx. Transition in matter domination.**.The ratio $C^{TT}_{l,DMx}/C^{TT}_{l,\Lambda CDM}$, at small ℓs a larger deviation can be noticed as expected for models with extra matter. Difference in the amplitudes of the oscillation and subtle deviation because a change in damping scale are observed. In both panels $z_c = \{10, 100, 1000\}$ corresponds green, blue, and red colors, respectively; straight (dash) lines corresponds to the case $\Omega_x(a_c) = 0.1\Omega_c(a_c)$ ($\Omega_x(a_c) = 0.05\Omega_c(a_c)$).

on the scale parameter a_c, and Ω_{ex}. A change in the diffusion damping scale, given by

$$r_d^2 = (2\pi)^2 \int_0^{a_\star} \frac{da}{a^3 H n_e \sigma_T} \left(\frac{R^2 + \frac{16}{15}(1+R)}{6(1+R^2)} \right) \tag{4.2}$$

with $R = (3\rho_b)/(4\rho_\gamma)$, n_e the number density of free electron and σ_T the Thompson cross-section, is also noticeable, where all oscillation modes are larger than in ΛCDM. The damping factor at last scattering depends on two things, first the visibility function that remains independent of cosmological parameters before the transition a_c, and second, the behavior of the damping scale k_D through last scattering. The last one depends on the acoustic scale and, on a smaller degree, on the Hubble rate (Hu et al., 1995). Since the extra radiation term ρ_{ex} changes both of these parameters, it is expected to have a smaller damping factor than in ΛCDM.

The overall change can be noticed in Fig. 4.12. In particular, for the mode at $k =$

Model	w_0	w_i	q	$k_c \times 10^4$	Ω^c_{ex}	$z_\star$	$r_s(z_\star)$	$100 \times \theta^X_s(z_\star)$	$D^\Lambda_A/D^X_A(z_\star)$
SEOS-I	-0.9	-1	2	3.19	0.035	1089.9	144.93	1.04155	1.00028
SEOS-II	-0.9	-1	10	3.21	0.041	1089.9	144.93	1.04152	1.00025
SEOS-III	-0.9	-1	2	3.25	0.029	1089.9	144.93	1.04147	1.00021
SEOS-IV	-0.9	-1	10	3.27	0.034	1089.9	144.93	1.04145	1.00019
SEOS-V	-0.9	-1	2	3.32	0.024	1089.9	144.93	1.04143	1.00017
SEOS-VI	-0.9	-1	10	3.33	0.028	1089.9	144.93	1.04142	1.00015

Table 4.6: Large Scales - SEOS cosmology. We present the SEOS parameters w_0, w_i z_c, q, with $\Omega^c_{ex} \equiv \Omega_{ex}(a_c)$. We show the values of the acoustic scale $r(z_\star)$, angular diameter distance $D_A(z_\star)$ (in hMpc^{-1}) and angle $\theta(z_\star)$ for the different SEOS-like models. In these cases $\Omega_{ex} = 0$ for $z < z_\star$ the angular diameter distance and the angle $\theta(z_\star)$ have a small deviations while $r_s(z_\star)$ remains the same. In these examples we took the same amount of matter $\Omega_m h^2 = 0.141$ in all models with $100\theta^\Lambda = 1.04126$ in ΛCDM model.

$0.148\,h$Mpc^{-1} we obtain an increment in power compared to ΛCDM. The increment in power becomes larger with increasing ℓ. For example, taking the multipole $\ell \sim 2000$ we find on average an enhancement close to 20%, 14% and 10% for models BDE-I, BDE-II, and BDE-III, respectively, compared to ΛCDM. In turn, the increase for the mode $k = 0.295\,h$Mpc^{-1} is slightly smaller with 17%, 13%, and 10% for BDE-IV, BDE-V, and BDE-VI models, respectively.

For the BDE models, the value of the angular scale of sound at reoinization (z_*), $\theta_s \approx r_s(z_*)/D_A(z_*)$ change due to the change in radiation, where r_s is the sound horizon and D_A is the distance to the surface of last scattering, z_*. For instance, for BDE comparing models with the same $k_c = 0.295$ we obtain $\theta_s = 1.0373, 1.038432, 1.039061$ for BDE-IV, V, and VI, respectively. We notice that for larger Ω^c_{ex} the smaller is θ_s and bigger is the amplitude of the bump. The same can be say for $k_c = 0.15\,h$Mpc^{-1}, where we obtain $\theta_s = 1.03499, 1.037459, 1.038683$ for BDE-I, II, and III, see table below. Notice that we have used the same $z_* = 1089.68$, therefore the same $D_A(z_*) = 13.9284$ is obtained, it is the sound horizon $r_s(z_*) = r_z(z_*; \Omega_b, \Omega_r)$ that change because the dependence on the amount of radiation before the transition of the BDE model, $r_s \approx \int_0^{t_*} c_s dt$ with $c_s \approx [1 + 3\Omega_b/\Omega_r]^{-1/2}$.

In the case of a transition in matter domination, we show the temperature power spectrum of the CMB for different cases from Table 4.2 and we plot the ratio $C^{TT}_{\ell,X}/C^{TT}_\Lambda$ in Fig. 4.13 and the values of the acoustic scale $r_s(z_*)$ and angular distance $D_A(z_*)$ in Table 4.5. Both $r_s(z_*)$ and $D_A(z_*)$ are slightly increased for larger ρ_{ex} or z_c. For example taking as reference the multipole $\ell \sim 2000$ we find on average an enhancement close to 35%, 27% and 10% for models DMx-I, DMx-II, and DMx-III, respectively, compared to ΛCDM for the case $\Omega_{ex}/\Omega_m = 0.1$. The difference diminishes for $\Omega_{ex}/\Omega_m = 0.05$ in which case we have a 11%, 9%, and 5% increase for DMx-IV, DMx-V and DMx-VI, respectively.

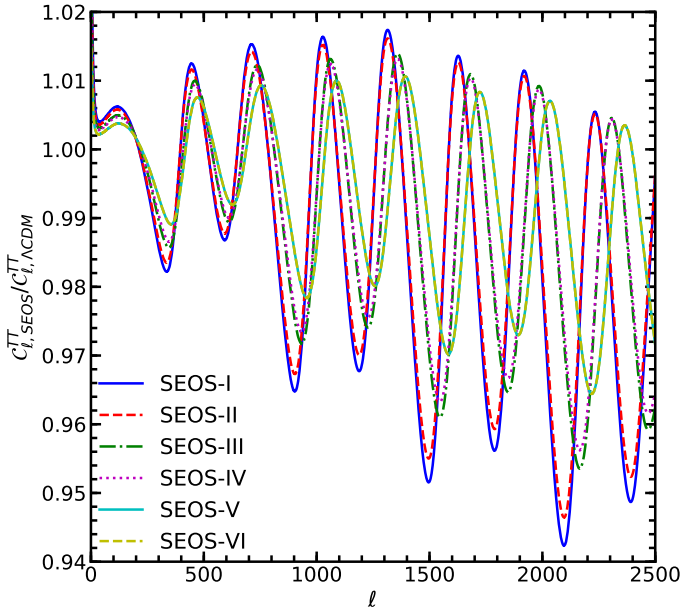

Figure 4.14: **The cosmic microwave background spectra for SEOS cosmologies.Transition at late times.** The ratio $\mathscr{C}_{l,SEOS}^{TT}/\mathscr{C}_{l,\Lambda CDM}$. Solid blue curves are for SEOS-I; dashed red curves are for SEOS-II; dashed-dotted green curves are for SEOS-III; dotted magenta curves are for SEOS-IV.

Here, we show how the dark energy parametrization, SEOS, affects the CMB TT anisotropies. In Fig. 4.14 we show $\mathscr{C}_{l,SEOS}^{TT}/\mathscr{C}_{l,\Lambda CDM}^{TT}$ for different combinations of parameters in the SEOS model, varying the quantity of matter and rate of expansion. We see that SEOS impacts the temperature field not only by changing the amount of matter, but there is also a distinctive imprint left by the steepness parameter q. Similar as in the BDE model, see sub-section 4.3, the SEOS model introduces the same three characteristics in the CMB due to ρ_{ex}. First, the shift to larger ℓs of the wiggles due to the change of the expansion rate caused by the increase of radiation content before the last scattering, and therefore, changing the extrema position of each oscillation as seen in Fig. 4.14. Larger values of the steepness q of the dark energy parametrization decreases the amplitude of the oscillations as we can see in the solid blue and dashed red curves, while smaller amount of DE also reduces the amplitude. In the SEOS model, in contrast with BDE model, the value of $r_s(z_*)$ is not affected by the transition at late times see Table 4.4. It is the value of $D_A(z_*)$ in Eq.(3.22) that changes in SEOS with the late-time transition and is consistent with previous results (Hou et al., 2013; Menegoni et al., 2012). It is worth keeping in mind that all six SEOS models have the same amount of matter and radiation.

4.4 Remarks and Conclusions

In this work, we studied cosmological implications of introducing an extra energy density ρ_{ex} to a ΛCDM model that dilutes rapidly at given scale factor a_c and corresponding wave-vector amplitude $k_c = a_c H(a_c)$. This RDED transition affects the background evolution, and hence the cosmological distances, such as the comoving angular distance D_A, the angular diameter D_M, the acoustic scale at recombination r_s and the diffusion damping scale r_d. Furthermore, the rapid dilution of ρ_{ex} also impacts the evolution of the matter perturbations and CMB power spectrum. This RDED leaves distinctive features in the matter power spectrum. In particular, it generates a bump in the matter power spectrum, more visible once we compare to ΛCDM. The bump is generated because the linear growth of $\delta_m(k)$ has a higher increase rate for larger H in radiation domination (c.f. Eq. (3.29)). This increase takes place only for modes $k \geq k_c$ when $\rho_{ex} > 0$ while for mode $k < k_c$ both models have the same expansion rate and the evolution of $\delta_m(k)$ is the same for both cases. The amplitude of the bump is related to the amount of the diluted energy density ρ_{ex}, while the mode is located about $k \sim k_c$. We study these bumps in the linear regime and also apply one-loop corrections using SPT.

We concentrated here in two different models, one located at large scales and the others at small scales. Both cases are inspired by the BDE model (Almaraz and de la Macorra, 2019; de la Macorra and Almaraz, 2018), where an RDED phase transition takes place in the radiation dominated epoch with $a_c \sim 10^{-6}$, affecting modes entering the horizon at early times. The corresponding mode is $k_c \sim 1\, h\text{Mpc}^{-1}$ and a bump is generated for modes $k \geq k_c$. Interestingly the BDE model also shows a RDED with a steep transition centered at a redshift $z_c \approx 0.625$ resulting in second bump located at large scales.

We also studied models (DMx) with extra matter, diluting in matter dominated epoch. In this case the growth of structure has two effects. The first one is due to having extra matter ρ_{ex} for $a < a_c$, affecting all modes ($k > k_c$) entering the horizon before a_c, while the second effect is due to the RDED at a_c. We study and distinguish the increase of amplitude in the linear evolution of the matter density perturbation of these two different sources. We obtain an increment around 8% in the power spectrum P_X/P_Λ due to the rapid dilution at the maximum of the bump at k_b. On the other hand we find a plateau for modes $k > k_c$ due to the extra matter. For modes entering the horizon after the transition $a < a_c$ we obtain no increase in the evolution of the matter density perturbations and we get $P_X/P_\Lambda = 1$ for modes $k < k_c$.

To study the imprints of dark energy, we considered a model-independent analysis and we parameterized the dynamics of dark energy using asteep equation of state (SEOS) (Jaber and de la Macorra, 2018). In the SEOS model the EoS w has a transition at $z_c = 0.28$. Here we studied two extreme cases, with soft and steep transitions, to observe different impacts on the CMB and matter power spectra.

We computed the position and amplitude of the peaks of the bumps in the matter power spectrum through the one-loop correction analysis using the code `MGPT`, taking into account the background evolutions with and without ρ_{ex}. We conclude that the non-linear effects shift the peak of the bumps to smaller modes and enhance their amplitudes in comparison to linear

computations.

We took different values of cosmological parameters for our two models shown in Table 4.1 for small scales, and 4.3 for large scales. In the linear regime, we see the bump imprint left by the rapid dilution of BDE on modes $k > k_c$, entering the horizon before a_c, as a peaked bump centered at $k = 0.47\,h\mathrm{Mpc}^{-1}$ for BDE-I,BDE-II,BDE-III ($k = 1.06\,h\mathrm{Mpc}^{-1}$ for BDE-IV,BDE-V, BDE-VI), where the enhancement of power in BDE is about 16% (19.58%), respectively. We see deviations at larger scales e.g. $k \geq 0.05\,h\mathrm{Mpc}^{-1}$ and $k \geq 0.5\,h\mathrm{Mpc}^{-1}$ respectively, due to the width of the bump in each case. The scale of the bump is mainly located at non-linear scales, although covering also quasi-linear scales, and once we determine the one-loop power spectra we find that BDE-III (BDE-VI) provides an enhancement of 4% (5%) at $k = 0.9\,h\mathrm{Mpc}^{-1}$ ($1.8\,h\mathrm{Mpc}^{-1}$), respectively. Nevertheless, these results should be taken as indicative since the high-k tails of the bumps are out of the reach of perturbation theory.

The late time dark energy transitions impacts the evolution of matter perturbations mainly at late times during the Einstein-de Sitter phase, matter perturbations have the same amplitude as in ΛCDM at all scales, the overall normalization is due to a slightly different rate of expansion in ΛCDM and SEOS models. Here we studied the same mode $k = 8.37 \times 10^{-5}\,h\mathrm{Mpc}^{-1}$ but different amounts of matter and steepness of the transition.

As time increases, the effect of the dynamical dark energy of the SEOS model is altered decreasing the amplitude for all Fourier modes and originating a bump at $k \approx 5 \times 10^{-3}$; that is, the power spectrum of ΛCDM is always larger than the power spectrum of SEOS model originating a bump at lower redshift.

Summarizing, this distinctive signature, named as bump, has been studied at a linear and one-loop level in perturbation theory. We have theoretically study the evolution of linear matter perturbations and showed that a bump is indeed generated in the matter power spectrum and we estimated the amplitude and width of the bumps in early and late times by means of BDE-like and SEOS-like models. We compared our results with a full implementation in the numerical Boltzmann code CAMB and found that our theoretical results are within a few percentage difference of the numerical results. This demonstrates that the origin of the bump, observed in matter power spectrum using the numerical simulations, is indeed due to a RDED.

To conclude, a small amount of extra energy density that dilutes rapidly is consistent with present-day cosmological measurements and may solve tensions in cosmology leaving distinctive detectable signatures.

Chapter5

STUDYING PARAMETRIC FAMILY OF GAUSSIAN BUMPS BEYOND THE LINEAR REGIME

Abstract

Some beyond ΛCDM cosmological models have dark-sector energy densities that suffer phase transitions. Fluctuations entering the horizon during such a transition can receive enhancements that ultimately show up as a distinctive bump in the power spectrum relative to a model with no phase transition. In this work, we study the non-linear evolution of such signatures in the matter power spectrum and correlation function using *N*-body simulations, perturbation theory and HMCODE- a halo-model based method. We focus on modelling the response, computed as the ratio of statistics between a model containing a bump and one without it, rather than in the statistics themselves. Instead of working with a specific theoretical model, we inject a parametric family of Gaussian bumps into otherwise standard ΛCDM spectra. We find that even when the primordial bump is located at linear scales, non-linearities tend to produce a second bump at smaller scales. This effect is understood within the halo model due to a more efficient halo formation. In redshift space these nonlinear signatures are partially erased because of the damping along the line-of-sight direction produced by non-coherent motions of particles at small scales. In configuration space, the bump modulates the correlation function reflecting as oscillations in the response, as it is clear in linear Eulerian theory; however, they become damped because large scale coherent flows have some tendency to occupy regions more depleted of particles. This mechanism is explained within Lagrangian Perturbation Theory and well captured by our simulations.

This chapter is adapted from its corresponding publication, D V Gomez-Navarro, A J

Mead, A Aviles, A de la Macorra, Impact of cosmological signatures in two-point statistics beyond the linear regime, Monthly Notices of the Royal Astronomical Society, Volume 504, Issue 3, July 2021, Pages 3284–3297, https://doi.org/10.1093/mnras/staa3393.

5.1 Introduction

In recent years the standard cosmological model know as ΛCDM has come under careful examination due to there exist some observational problems within the model. For instance, the H_0 and σ_8 (or equivalently $S_8 = \sigma_8(\Omega_m/0.3)^{0.5}$) tensions. The first one is based on a discrepancy of the estimated value of the rate expansion of the Universe between early- and late-time observations (e.g., Verde et al., 2019), while latter one refers to a disagreement of the amplitude of the variance of the matter density field between weak gravitational lensing studies (e.g., Abbott et al., 2018; Hikage et al., 2019; Heymans et al., 2020) and CMB observations (Planck Collaboration, 2018b). Both tensions may indicate the need to extend the ΛCDM model. However, there are high-precision measurements, such as those of the CMB from *Planck* (Planck Collaboration, 2018b) and large-scale structure in SDSS-IV (collaboration, 2020), including Baryon Acoustic Oscillations (BAO) and Lyman-Alpha forest observations, can individually be well understood within ΛCDM.

Some of the models beyond of ΛCDM are based on extensions of the standard model of particle physics (Zyla et al., 2020), which can describe dark-sector of the Universe. For instance, the Bound Dark Energy (BDE) cosmology (de la Macorra and Almaraz, 2018; Almaraz and de la Macorra, 2019) introduces massless particles, which they decay like radiation at early times. However, some time latter the elementary particles form massive bound states due to a phase transition taking place at a scale factor a_c and the energy density of BDE dilutes as $\rho \sim a^{-6}$ at the phase transition scale factor a_c. The lightest scalar field ϕ corresponds to dark energy and remains subdominant for a long period of time. At present time BDE behaves dynamically accelerating the expansion of the Cosmos. This behaviour leaves imprints in two point statistics (Almaraz et al., 2020) – for a model independent analysis see (Jaber-Bravo et al., 2020) – generating a bump in the matter power spectrum at a scale k_T entering the horizon about the phase-transition time. We call models that generate features through phase transitions Rapid Diluted Energy Density (RDED) (de la Macorra et al., 2021), and BDE is one such example. Studying the impact of cosmological signatures in the two point statistics may help in explaining the nature of dark-sector components beyond ΛCDM.

In this work we are motivated by RDED effects in the linear matter power spectrum. However, we will work in a model-independent way by introducing a parametrized bump to the linear matter power spectrum that will vary in position and width. We study the signatures imprinted in the linear matter power spectrum and we follow them beyond the linear regime using different, but complementary, tools.

There are different perturbative schemes, know as Higher-order Perturbation theory (e.g., Bernardeau et al., 2002b) (PT), to describe the intermediate, quasi-linear scales of the matter

clustering having different advantages. For example, Lagrangian Perturbation Theory (LPT) is very accurate in modelling the two-point correlation function, particularly the smearing and shift of the Baryon Acoustic Oscillation (BAO) peak located at a large scale ($\sim 100\,h^{-1}$Mpc). Otherwise, Standard (Eulerian) Perturbation Theory (SPT) is more successful in describing the broadband power spectrum, but poorly models the BAO (e.g., Tassev, 2014a; Baldauf et al., 2015). As soon as fluctuations become large, perturbative approaches break down and PT become meaningless. At this scenario, the dark matter particles can be described accurately by N-body simulations, although these have the disadvantage of being computationally expensive. However, the large scale structure statistics can be elucidated by halo models (e.g., Seljak, 2000; Peacock and Smith, 2000; Cooray and Sheth, 2002).

The two-point statistics has been studied in detail for standard ΛCDM cosmologies. For instance, PT provides high accuracy at large scales or high redshifts (Bernardeau et al., 2002b), while at non-linear scales one can either use fitting functions (e.g., Smith et al., 2003; Takahashi et al., 2012), halo-model based methods (e.g., HMCODE: Mead et al., 2015, 2016; Mead et al., 2020) or emulators (e.g., Lawrence et al., 2010, 2017), all of which have been tuned to reproduce the power spectra measured in high-resolution N-body simulations. Recent studies has been focused on modelling the power spectrum 'response', which is the ratio of two power spectra, with the numerator typically the cosmology of interest and the denominator typically a cosmology whose power spectrum is well known. The response function has the virtue of being both easier to simulate, requiring only moderate resolution simulations, and easier to model and it has been successfully studied for dark-energy cosmologies (Casarini et al., 2016; Mead, 2017), modified gravity (Cataneo et al., 2019), massive neutrinos (Cataneo et al., 2020) and for the effects of baryonic feedback (Mead et al., 2020).

In this work we study the non-linear impact of cosmological signatures in two-point statistics that can be approximated by a bump in the linear power spectrum, with our bump cosmology parametrized as in equation (5.1). We compare the bump cosmology with standard ΛCDM cosmology with no bump via the response function, which is constructed by taking the ratio of non-linear statistic of cosmology with bump to a standard ΛCDM cosmology with no bump. We use complementary approaches to model non-linearities, for the real space power spectrum, we use 1-loop SPT, the HMCODE model[1], and low-resolution N-body simulations. We further consider the effect of redshift space distortions in the power spectrum using the TNS model (Taruya et al., 2010) and the model of (Scoccimarro, 2004). The non-linear correlation function is obtained through the Convolution-LPT (CLPT) of (Carlson et al., 2012b; Vlah et al., 2015b).

This chapter is organized as follows. In Section 5.2 we introduce the parametric bump cosmology to be used in the rest of the work and we present specifications of our N-body simulations suite employed to test the analytical methods. We also review different analytical models to describe the redshift and real space matter power spectrum, as well as the correlation function. In Section 5.3, we present the numerical and analytical results for the

[1]https://github.com/alexander-mead/HMcode

response functions. Finally we conclude in Section 5.4.

5.2 Modelling the matter power spectrum

Let us study the RDED effect choosing a parametrization that we refer throughout as the 'bump cosmology', where the linear power spectrum is given by a modification to that of a standard ΛCDM cosmology:

$$P_{\rm bump}(k,z) = \left[1+F(k)\right]P_{\Lambda\rm CDM}(k,z)\ , \tag{5.1}$$

with

$$F(k) = A\exp\left(-\frac{[\ln(k/k_{\rm T})]^2}{\sigma^2}\right)\ . \tag{5.2}$$

A, k_T and σ are the amplitude, scale, and width of the bump, respectively. We considered other choices for the function $F(k)$, such as a Gaussian in k-space, and found qualitatively similar results.

We consider nine different bump cosmologies, in each case we fix the amplitude $A = 0.15$. This amplitude is motivated by BDE-like models, where the dark energy density $\Omega_{\rm BDE}(a_c) = 0.11$ suffers a phase transition taking place at $a_c = 2.48\times10^{-6}$ with $\Omega_{\rm BDE} \ll 1$ at scales $a > a_c$. Otherwise, we choose three different widths of the bump $\sigma = 1.0$, 0.3, and 0.1, and place the bump at three different scales: $k_T = 0.05$, 0.1, and $1\,h$Mpc^{-1} (see Table 5.1). The width of the bump corresponds to how fast the rapid diluted energy density takes place, whereas k_T represents mode entering the horizon about the phase transition time. We investigate structure formation in these bump cosmologies at the redshifts $z = 0$, 0.5, 1, 2, 3, and 4. To generate the ΛCDM power spectrum we use the cosmological parameters reporting in Section 5.2.2, which are the same in both the bump and standard cosmologies, so that the *only* difference between the models is the presence of the bump.

Let us study the response of the real-space matter power spectra and correlation functions together with the redshift-space multipole power spectra. The response is constructed by computing the ratio of the measurement or prediction between a bump and ΛCDM cosmology. To study the two-point statistics at non-linear scales we take into account different schemes: moderate-resolution N-body simulations, and HMCODE. In addition, for the real-space power spectra we also consider one-loop SPT, for the redshift-space multipole power spectra we use the TNS and Scoccimarro models and finally, for the real-space correlation function we use CLPT.

5.2.1 HMCODE

We will use the HMCODE (Mead et al., 2015) model in order to compute the non-linear matter power spectrum, which takes as input the linear power spectrum of the cosmology in question,

and then uses some information about the background cosmological parameters and power-spectrum shape and amplitude in order to make its predictions. We expected that HMCODE will make reasonable predictions on the bump cosmologies investigated in this work due to HMCODE has been tested for a variety dark energy models. We will see that the bump cosmologies will affect the HMCODE predictions in two ways. One of them is trivial since that the HMCODE prediction at large scales is essentially linear theory and because linear theory contains the bump then so will HMCODE. The second, is that within HMCODE the one-halo power is determined by the halo mass function, which itself depends on the linear power spectrum via the variance in the power spectrum as a function of scale. The bump will therefore affect the halo mass function and we expect that it will boost the predicted numbers of haloes in certain mass ranges.

Before running HMCODE, we can make the prediction that it should generally boost power in the one-halo term for a bump cosmology compared to a cosmological model that lacks a bump. The traditional halo model calculation has a problem in the transition region between the two- and one-halo terms ($k \sim 0.05\,h\mathrm{Mpc}^{-1}$ at $z = 0$), and generically underestimates the true non-linear power spectrum in this region; this probably arises due to an improper treatment of non-linear halo bias (Smith et al., 2007). The solution to this problem in HMCODE is a smoothing of the transition region. Based on this discussion, we could predict that the HMCODE predictions for the bump cosmologies may be better in the deeply one-halo regime ($k > 1\,h\mathrm{Mpc}^{-1}$), and that they may be less impressive in the transition region. In the linear region they should be perfect, given that the HMCODE prediction is identical to linear theory at large scales. In the quasi-linear regime ($k \sim 0.1\,h\mathrm{Mpc}^{-1}$ at $z = 0$) we would expect perturbation theory to perform better than HMCODE since the latter lacks any formal grounding in analytical perturbation theory.

5.2.2 N-body simulations

We ran 12 N-body simulations using the cosmological simulation code GADGET-2 (Springel, 2005), one each for the cosmologies detailed in Table 5.1. We choose a background ΛCDM cosmology with total matter density $\Omega_m = 0.3$, baryon density $\Omega_b = 0.05$, dark energy density $\Omega_\Lambda = 0.7$, amplitude of the matter power spectrum $\sigma_8 = 0.8$, spectral index $n_s = 0.96$, and dimensionless Hubble constant $h = 0.7$. We use the Zeldovich approximation, based on the idea to displace particles from an initially Cartesian mesh and assign them velocities, to generate initial conditions at $z = 99$ using NGENIC,[2]. We considered to run simulations with different box sizes for the different k_T values, to ensure that there was always a good sampling of modes around k_T. The box sizes of the simulations are $L_{box} = 256$, 512 and $1024\,h^{-1}\mathrm{Mpc}$, for $k_T = 0.05$, 0.1 and $1\,h\mathrm{Mpc}^{-1}$ respectively. Each simulation uses 512^3 particles to approximate the density field. The low particle number of the N-body simulations can bias measurements. To check this systematic effect we study the convergence of our modest-

[2]https://www.h-its.org/2014/11/05/ngenic-code/

Name	A	σ	k_T $[h\mathrm{Mpc}^{-1}]$	L_{box} $[h^{-1}\mathrm{Mpc}]$
FATBUMP-K1	0.15	1.0	1.0	256
MEDBUMP-K1	0.15	0.3	1.0	256
THINBUMP-K1	0.15	0.1	1.0	256
ΛCDM-K1	–	–	–	256
FATBUMP-K0P1	0.15	1.0	0.1	512
MEDBUMP-K0P1	0.15	0.3	0.1	512
THINBUMP-K0P1	0.15	0.1	0.1	512
ΛCDM-K0P1	–	–	–	512
FATBUMP-K0P05	0.15	1.0	0.05	1024
MEDBUMP-K0P05	0.15	0.3	0.05	1024
THINBUMP-K0P05	0.15	0.1	0.05	1024
ΛCDM-K0P05	–	–	–	1024

Table 5.1: Specifications of our N-body simulation suite. The background cosmological parameters are the same for all the simulations: $\Omega_m = 0.3$, $\Omega_b = 0.05$, $\Omega_\Lambda = 0.7$, $\Omega_\nu = 0$, $h = 0.7$, $n_s = 0.96$, $\sigma_8 = 0.8$. Each simulation uses 512^3 particles distributed over $N_{grid} = 512^3$ cells. We consider the redshifts $z = 0, 0.5, 1, 2, 3, 4$.

resolution 512^3 particles simulations with respect to low-resolution 256^3 particle simulations and found that our results for the power spectrum *response* were only significantly affected (> 1 per cent) on scales smaller than half of the particle Nyquist frequency, although there were some noticeable, sub per-cent differences for scales as large as one tenth of the particle Nyquist frequency. However, the bias that arises when using a low mass resolution cancels when constructing a response; so the same (or a similar) bias must occur in the cosmologies of both the numerator and denominator that make up the response.

5.3 Results and analysis

The evolution, dilution and shift of the bump is studied via the different approaches, such as N-body simulations, HMCODE and PT methods, as complementary tools. The response functions are given by

$$R(k) = \frac{P_{\rm bump}(k)}{P_{\Lambda{\rm CDM}}(k)}. \tag{5.3}$$

The results are contrasted with the linear theory, for which the response in the power spectrum is simply $R_L(k) = 1 + F(k)$ at all z because linear growth is scale independent.

5.3.1 Real-space matter power spectrum

We use cloud-in-cell mass-assignment scheme to extract the power spectra data. The grid is divided into $N_{grid} = 512^3$ cells. The power spectra are binned in 100 evenly log-spaced k-points over a range $[k_{min}, k_{\rm Ny}]$, where $k_{\rm Ny} = N_{grid}\pi/L$ is the Nyquist frequency, and $k_{min} = 2\pi/L$. L is the size of the box, which is given in Table 5.1 for the different simulations. Usually power spectra in CIC approach are considered to be accurate up to half of the Nyquist frequency. In our plots we consider all measured scales, up to $k_{\rm Ny}$, and the reader should keep this in mind.

Figs. 5.1, 5.2, and 5.3 show the responses using the bump cosmology from equation (5.1) located at the scales $k_T = 0.05$, 0.1, and, $1\,h{\rm Mpc}^{-1}$, respectively. The matter power spectra are computed using our different approaches and then divided by their counterparts in ΛCDM to create the response function. This analysis compares how the bump cosmologies are modified by non-linearities within the different schemes.

At higher redshifts non-linear effects are smaller and the responses of all approaches are very similar. In Fig. 5.1, corresponding to $\sigma = 1$, as z decreases we observe two things in the simulated measurements:

1.- At the small-scale edge of the bump we see the power grow above the bump, an effect that is captured extremely well by SPT and less well by HMCODE.

2.- We see the generation of a second bump at much smaller scales, with a peak $k \sim 1\,h{\rm Mpc}^{-1}$.

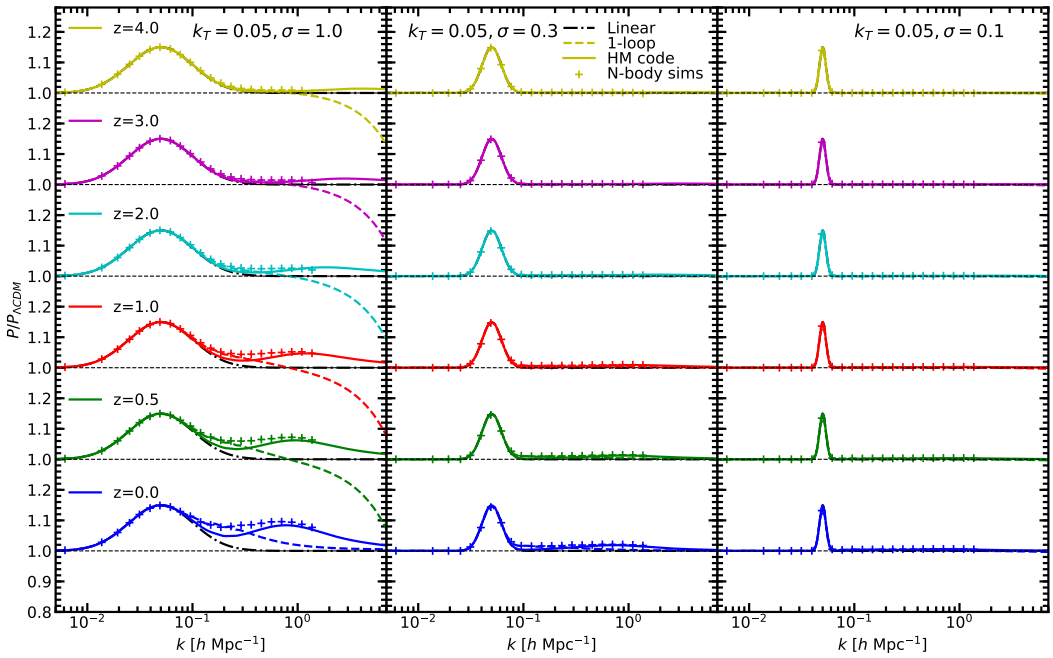

Figure 5.1: Response functions for the bump cosmologies at $k_T = 0.05\,h\mathrm{Mpc}^{-1}$. From top to bottom, yellow curves are for redshift $z = 4$; magenta for $z = 3$; cyan for $z = 2$; red for $z = 1$; green for $z = 0.5$; and blue for $z = 0$. The left panel shows the bump cosmology for $\sigma = 1$; middle panel for $\sigma = 0.3$; and right panel for $\sigma = 0.1$. Dash-dotted (black) curves are for the linear theory; dashed (color) are for 1-loop SPT; solid for HMCODE model; and crosses are for the measurement from N-body simulations.

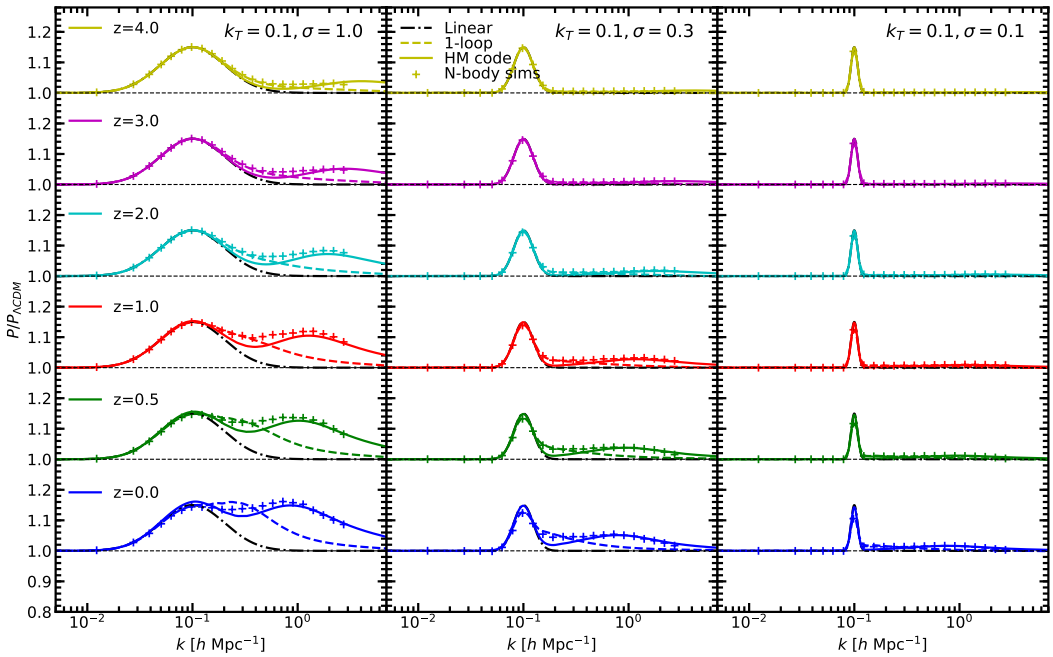

Figure 5.2: Same as Fig. 5.1 but for the bump cosmologies with $k_T = 0.1\,h\mathrm{Mpc}^{-1}$.

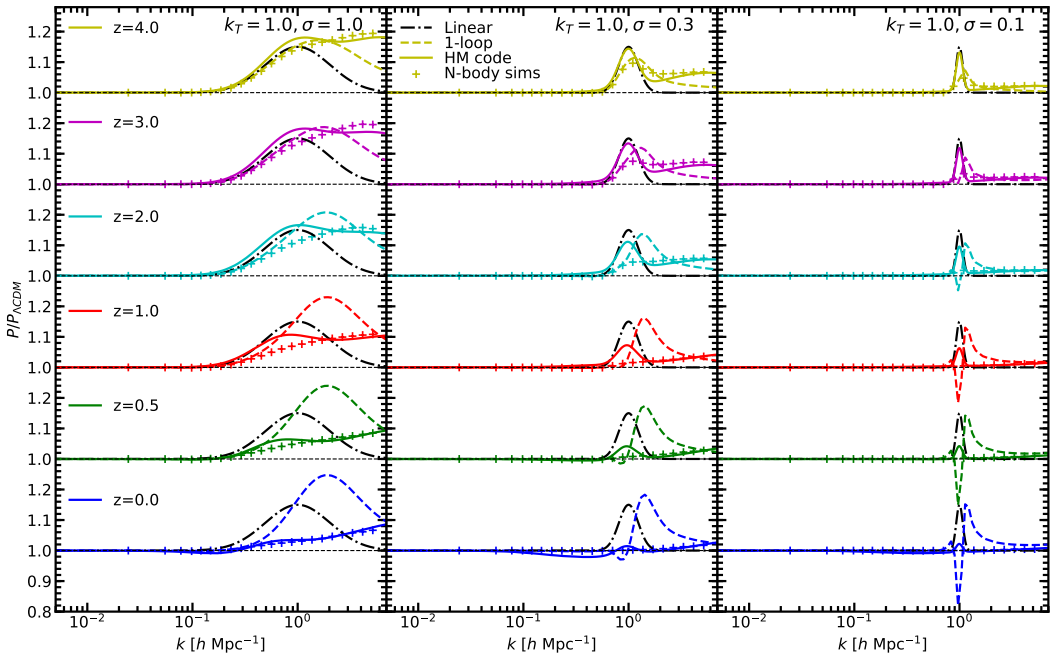

Figure 5.3: Same as Fig. 5.1 but for the bump cosmologies with $k_T = 1\,h\mathrm{Mpc}^{-1}$.

As expected, this second bump is not captured at all by SPT (which even predicts a decrease in the response at higher z) due to it being far out of the reach of its regime of validity. However, this second non-linear bump is well modelled by HMCODE, which peaks at $k \approx 1\,h\mathrm{Mpc}^{-1}$ and reaches a maximum at $z = 0$, peaking in amplitude at ~ 10, 2, and 1 per cent for the $\sigma = 1$, 0.3, and 0.1 cases respectively. In the $k_T = 0.1$ case, shown in Fig. 5.2, this second non-linear bump is even clearer, peaking at $k \approx 1\,h\mathrm{Mpc}^{-1}$ for $z \simeq 0$, but at smaller scales for higher redshifts. For some of our cosmologies, this second non-linear bump is even larger than the primordial bump. For instance, it is larger for $\sigma = 1$ at both redshifts $z = 0.0$ and $z = 0.5$, contributing ≈ 18 and 16 per cent to the whole response respectively. Notice that as the width of primordial bump decreases, the second, non-linear bump amplitude decreases. Also, the location and amplitude of the non-linear bump as seen in the simulated data is in agreement with the predictions from HMCODE in all cases. In Figs. 5.1 and 5.2, corresponding to $k_T = 0.05$ and $0.1\,h\mathrm{Mpc}^{-1}$ respectively, HMCODE and the simulation response provide similar results at lower redshifts and in the non-linear regime. Conversely, 1-loop SPT gives results closer to those obtained from simulated data at higher redshifts and in the mildly non-linear regime ($k \lesssim 0.2\,h\mathrm{Mpc}^{-1}$).

Why do these non-linear bumps appear in the response functions? The non-linear bumps emerge due to interaction between the primordial bump and the one-halo term, being highly enhanced for the wider bumps simply because these provide a greater enhancement of linear power. This can be understood via two ways: First, within the halo model (and therefore within HMCODE), where the one-halo term is given by the integral of the halo mass function multiplied by the squared Fourier-space halo profile. The halo mass function itself is related to the standard-deviation in the density field when smoothed over the Lagrangian radius of the halo, σ_R. The bump cosmology increases the power over a certain range of scales, such that σ_R will also increase, and therefore so will the mass function. Hence, halo formation for the bump cosmology will be larger than cosmology with no bump. The second way to think about this is via the increased amplitude of some modes, given here by our bump cosmology, is helping more small scale fluctuations to cross over the critical threshold to collapse. This (Press and Schechter, 1974) type argument occurs even when the bump is at very linear scales as long as the width is sufficiently large, because those long wavelength modes exist underneath small scale fluctuations enhancing the collapse to form the actual haloes. We note that this is a highly non-linear effect, such that the second bump is not well described by PT, where the main effect is the spreading and enhancement of the primordial bump.

In the $k_T = 1\,h\mathrm{Mpc}^{-1}$ bump cosmologies, shown in Fig. 5.3, the simulation response demonstrate that the primordial bump become erased due to the non-linear evolution. Such effect is well modelled by the HMCODE but not captured by PT since these scales are far beyond its reach, although at the highest redshifts it works moderately well. The non presence of the second bump is surprising, given that the primordial bump and the 1-halo term are located about the same scale.

Perturbation theory provides an accurate model for the power spectrum response at large scales, with the accuracy extending to smaller scales at higher redshift as is demonstrated

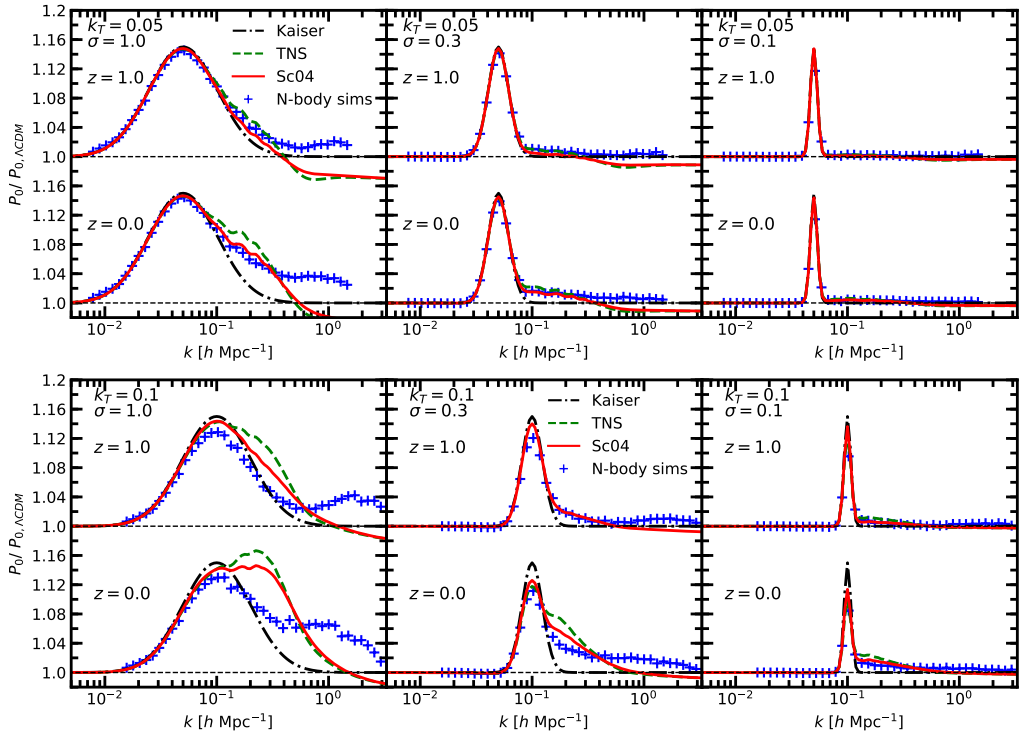

Figure 5.4: Responses of the monopole power spectrum at $z = 0$ and 1 for the bump cosmologies at $k_T = 0.05$ (top panel) and $0.1\,h\mathrm{Mpc}^{-1}$ (bottom panel), with different widths $\sigma = 1, 0.3, 0.1$ (from left to right). Dashed black shows the Kaiser linear theory; dashed green is for the TNS model; solid red for Sc04 model; and the blue crosses show the simulated data.

in Figs 5.1, 5.2 and 5.3. Otherwise, HMCODE provides a reasonable (though less perfect) model for the response at the smaller scales, those usually associated with halo formation. The combination of these two methods could provide an accurate model for the response that would be valid across a wider range of scales. This novel scheme has been studied in the literature previously (e.g., Mohammed and Seljak, 2014; Seljak and Vlah, 2015; Philcox et al., 2020), but has never been applied to the bump cosmology specifically.

5.3.2 Redshift-space matter power spectrum multipoles

In this Section, let us explore the responses of the redshift-space monopole and quadrupole power spectra using the non-linear models Sc04 and TNS. For comparison we also use Kaiser linear theory. For the multipole power spectra we use a triangular-shaped-cloud mass-assignment function, on a grid with $N_{grid} = 512^3$ cells, computing via the N-BODYKIT pack-

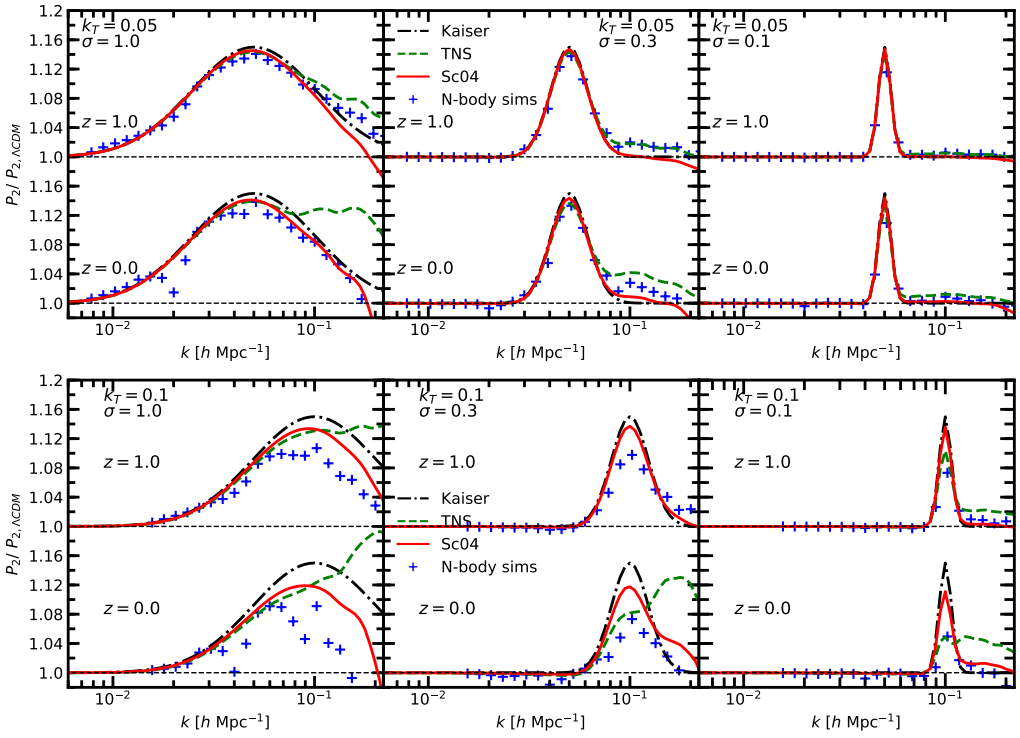

Figure 5.5: As Fig. 5.4 but for the quadrupole response.

age[3]of (Hand et al., 2018).

The response functions in the monopole P_0 at redshifts $z = 0$ and $z = 1$ for the bump cosmologies with $k_T = 0.05\,h\text{Mpc}^{-1}$ are shown in the top panel of Fig. 5.4. Theoretical models perform closer to the simulation response than the linear theory in the quasi-linear regime is not surprising, in the sense that the responses are closer to those from N-body simulations. However, for $k > 0.2\,h\text{Mpc}^{-1}$ both non-linear models make deviations from the simulated data. The response functions for the bump cosmologies located at $k_T = 0.1\,h\text{Mpc}^{-1}$ are shown in the bottom panel of Fig. 5.4. As in the case of $k_T = 0.05\,h\text{Mpc}^{-1}$, the response is well captured by the PT approaches in the quasi-linear regime, although the non-linear signatures of the bump are less well captured when comparing to the simulations since the scale of the bump is located at the edge of the perturbative regime of validity. On the other hand, the linear theory provides a better match to the simulation responses for some non-linear scales, obviously the good performance of linear theory here is only a lucky coincidence. The behaviour of the second non-linear bump at $\approx 1\,h\text{Mpc}^{-1}$ is similar to the case in real space, but is not present in the $k_T = 0.05\,h\text{Mpc}^{-1}$ case, even though in real space this non-linear bump was visible in both cases. (Gomez-Navarro et al., 2020) suggest that this effect is because the damping along the line-of-sight direction of the redshift-space power spectrum, which ultimately comes from the highly oscillatory behavior of the correlator inside the integral of equation (2.58) at large k. This redshift-space behaviour damps the multipoles in all bump cosmologies, but since the second (real space) bump is larger for the case of $k_T = 0.1\,h\text{Mpc}^{-1}$, it can overcome the damping and it still appears in the redshift-space responses.

In Fig. 5.5, we show the quadrupole redshift-space power spectra for $k_T = 0.05\,h\text{Mpc}^{-1}$ and $k_T = 0.1\,h\text{Mpc}^{-1}$. Although the simulated quadrupole measurements are noisier than for the monopole, we obtain a similar result to that predicted by the PT methods, most obviously for the case of $k_T = 0.05\,h\text{Mpc}^{-1}$ at $z = 1$. We also see that the non-linear, second bumps do not show up in the quadrupole. (Gomez-Navarro et al., 2020) suggest that this is due to the multipole gives maximum weight to the line-of-sight direction where the damping effect occurs, while the monopole gives equal weight to all directions.

5.3.3 Real-space matter correlation function

We study the measured real-space correlation function responses, defined as $\xi_{\text{bump}}(r)/\xi_{\Lambda\text{CDM}}(r)$, from both the simulated data and the analytical correlation function calculated according to the CLPT method. All simulated correlation functions have been measured by employing the N-BODYKIT code, using 60 linearly spaced bins in the range 1–121 h^{-1}Mpc for the bump cosmologies at $k_T = 0.05\,h\text{Mpc}^{-1}$, 30 bins in the range 1–61 h^{-1}Mpc for models at $k_T = 0.01$, and 15 bins in the range 1–31 h^{-1}Mpc for models at $k_T = 1.0\,h\text{Mpc}^{-1}$.

In Fig. 5.6, we show the response functions for the bump at $k_T = 0.05\,h\text{Mpc}^{-1}$ for four different redshifts $z = 2$, 1, 0.5, and 0 and the bump cosmologies with widths $\sigma = 1$, 0.3,

[3]https://nbodykit.readthedocs.io

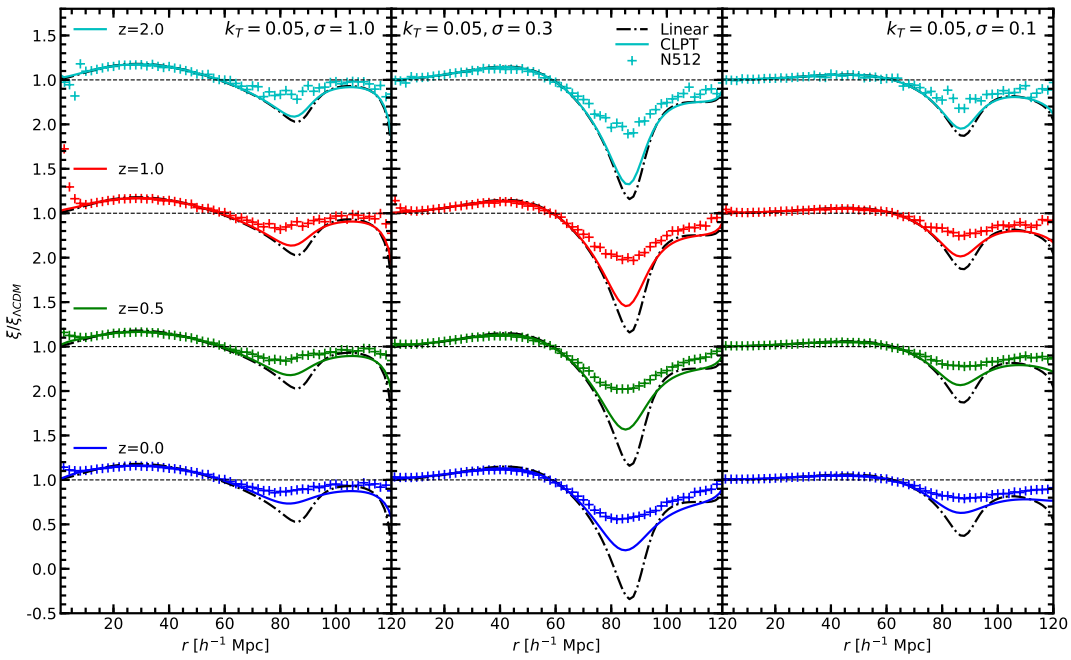

Figure 5.6: The real-space correlation function response: We plot $\xi/\xi_{\Lambda CDM}$ for bump cosmologies at $k_T = 0.05$ in units $h\mathrm{Mpc}^{-1}$ for different redshifts ($z = 0.0, 0.5, 1.0, 2.0$). From top to bottom, cyan curves are for $z = 2$; red for $z = 1$; green for $z = 0.5$; and blue for $z = 0$. Right: Bumps with $\sigma = 1.0$. Middle: Bumps with $\sigma = 0.3$. Left: Bumps with $\sigma = 0.1$. The CLPT correlations are represented by the solid lines. The plus markers denote the N-body simulations. The black dash-dotted lines denote the linear correlation function.

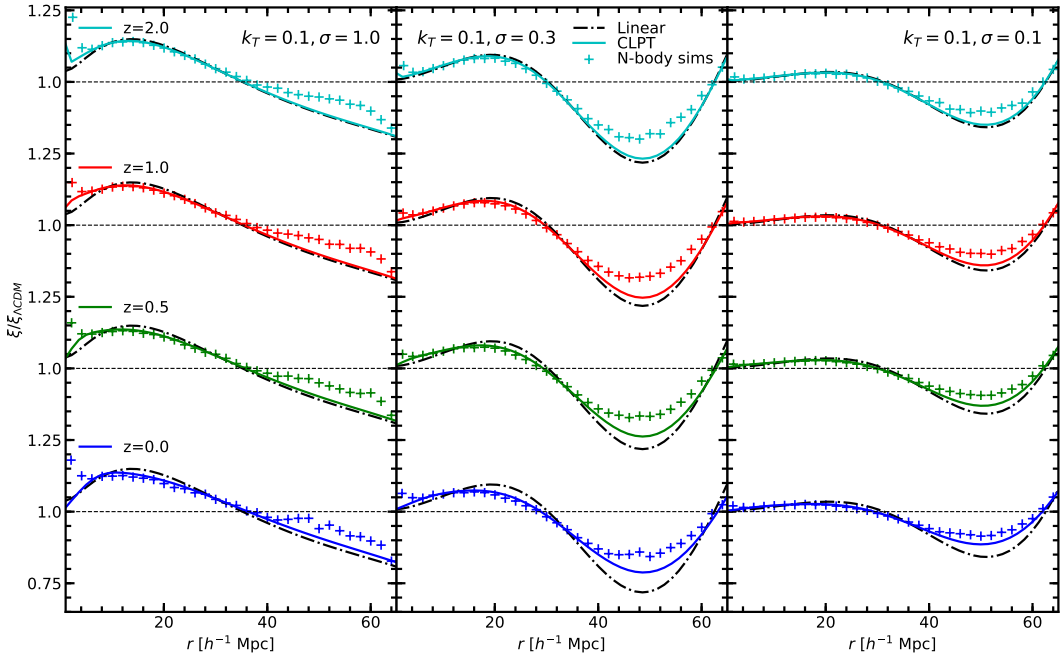

Figure 5.7: As Fig. 5.6 but for the bump cosmologies with $k_T = 0.1\,h\mathrm{Mpc}^{-1}$.

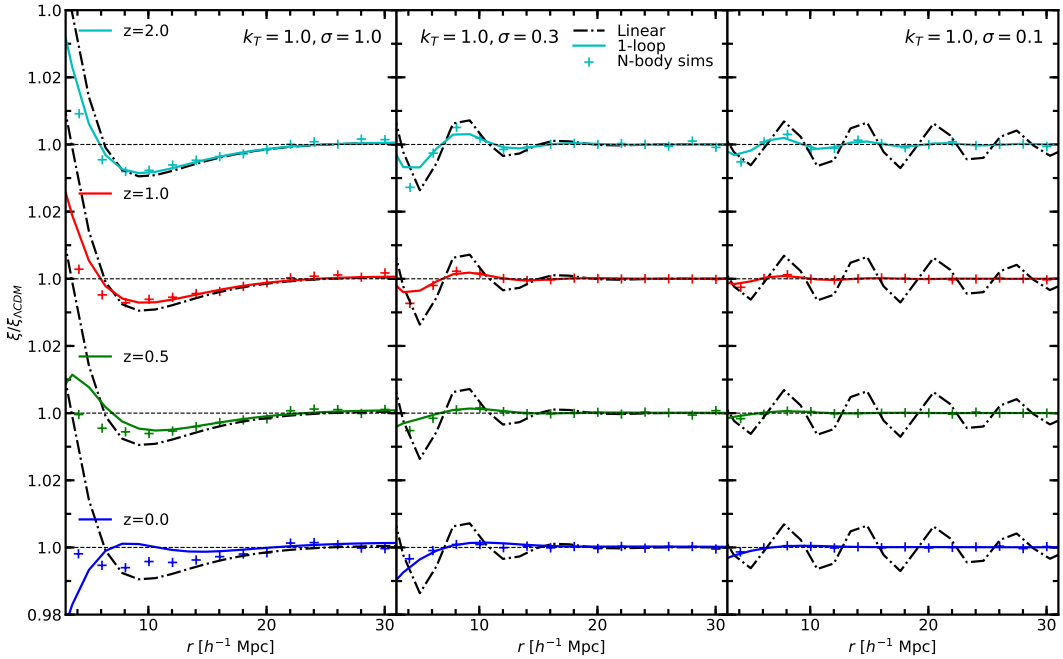

Figure 5.8: As Fig. 5.1 but for the bump cosmologies with $k_T = 1\,h\mathrm{Mpc}^{-1}$.

and 0.1. We find a dip in the response around $85\,h^{-1}$Mpc. We suggest that this is because a long wavelength modulation of the whole correlation function because of the localized bump feature in the corresponding power spectrum. By considering equation (5.1), the linear correlation function response is given by

$$R_L(r) = 1 + \frac{1}{\xi_L^{\Lambda\mathrm{CDM}}(r)} \int_0^\infty d^3r' \xi_L^{\Lambda\mathrm{CDM}}(r') \tilde{F}(|\mathbf{r} - \mathbf{r}'|), \tag{5.4}$$

with

$$\tilde{F}(r) = \int_0^\infty \frac{dk}{2\pi^2} k^2 F(k) j_0(kr), \tag{5.5}$$

where j_0 is the zero-order spherical Bessel function. Physically, the dip can be understood as follows: for scales $r \gg k_T^{-1}$ we have that $\tilde{F}(r) \to 0$ because of large cancellations provided by $j_0(kr)$; while as $r \to 0$, $\tilde{F}(r) \to (2\pi^2)^{-1} \int dk k^2 F(k)$, a constant that when computed turns out to be much smaller than the correlation function at those small scales; such that the linear response goes to unity at both large scales and small scales limits. On the other hand, $k^2F(k)$ reaches its maximum at scales $k_{max} > k_T$, the larger the width σ, the bigger are k_{max} and the maximum values $k_{max}^2 F(k_{max})$; however for larger widths, the function $k^2F(k)$ overlaps with more oscillations and $\tilde{F}(r)$ is suppressed. The inverse transformed bump feature, $\tilde{F}(r)$, turns out to be a sinc-like function in real space with amplitude proportional to the σ and first trough around $r_T \lesssim (3/2)\pi/k_T$. Moreover, the aforementioned effects compete and this becomes more pronounced for the width $\sigma = 0.3$ case. Coincidentally, for the case $k_T = 0.05$, this trough is located at about the same scale as the dip, at about $87\,h^{-1}$Mpc, in the correlation function, and both reinforce each other to produce the large dip observed in Fig. 5.6.

More generally, for the different choices of k_T the changes in the correlation-function response will follow a similar pattern, but the wave-length modulations will be related to the characteristic scales: For larger k_T and smaller σ, the oscillations in the correlation function have higher frequency and are damped at smaller scales. This can be seen in Figs. 5.7 and 5.8, for the cases $k_T = 0.1$ and $1\,h\mathrm{Mpc}^{-1}$, respectively. The main qualitative difference compared to the $k_T = 0.05\,h\mathrm{Mpc}^{-1}$ case is that the reinforcement with the BAO characteristic dip is not present in these cases.

The peaks and troughs are more pronounced in the linear theory since the correlation function scales simply with the scale-independent linear growth function. On the other hand for CLPT, even in the Zeldovich approximation, overdense regions are partially depleted, while underdense regions populated, due to the free-streaming of coherent matter flows over a scale settled by the Lagrangian displacements 1-dimensional variance $\sigma_\Psi^2 = \int_0^\infty dk P_L(k)/(6\pi^2)$.[4] This effect is captured very well by our numerical results, and the damping in the responses become very similar for simulated data and CLPT. More remarkably for the cases of $k_T = 1\,h\mathrm{Mpc}^{-1}$ with $\sigma = 0.3$ and 0.1, corresponding to middle and right panels of fig. 5.8, where

[4]This effect has the same origin as the smearing of the BAO peak observed in LPT and simulations (see, e.g. Tassev 2014a).

the oscillations in the power spectrum are practically erased. The reason for this is, of course, that the peaks and troughs are more closer to each other and the free-streaming of particles can cover such distances. Indeed, particles travel, on average, a distance settled by the standard deviation of the displacement field $\sigma_\Psi(z) \sim 6 \times D_+(z)\, h^{-1}$Mpc with $D_+(z)$ the linear growth function, so the process of particles moving out from more dense regions becomes very efficient.

5.4 Remarks and conclusions

Phase transitions in the dark sector are common in theories of cosmology beyond ΛCDM, and these leave fingerprints that are potentially detectable by current and future surveys. One of these signatures is the creation of enhanced features in the power spectrum at scales where otherwise the power would be smooth. The generation of these can be understood since all k-modes entering the horizon during the time elapsed by the phase transition suffer an enhancement on their amplitude since adding an extra ρ_{ex} increase the growth rate of the linear matter perturbations impacting modes $k \geq k_c$ entering the horizon for $a < a_c$. In this work we have focused on bumps generated in the power spectrum, motivated by the recently proposed BDE model of (de la Macorra and Almaraz, 2018) and SEOS (Jaber-Bravo et al., 2020).

We have studied non-linear evolution of parametric *bump cosmologies*. We have chosen to be as model independent as possible, instead of considering bumps generated by any specific BDE model, since we are interested in a wider range of theoretical models. We have also fixed the background cosmology to be ΛCDM to allow us to investigate the phenomenology of bumps in isolation. In order to do so, we have run modest-resolution N-body simulations, which are complemented by perturbation theory models and non-linear halo-model calculations from the HMCODE model of (Mead et al., 2015). We expect the different methods used to work over different ranges of scales, and this complementarity is important, since although bumps can be localized at a given scale, these are naturally spread by non-linear evolution, typically covering scales that may be outside the range of validity of some particular method. Bearing in mind that non-linear ΛCDM is well studied, we have put attention to the power spectrum response, constructed as the ratio of the power in a bump cosmology to a cosmology with no bump, instead than on the power spectrum itself. Once an accurate model for the response is at hand, this can be converted into an accurate model for the power spectrum by multiplying by an accurate model for the ΛCDM non-linear power spectrum. We have studied the non-linearities in both real and redshift space for the power spectrum and how these fingerprints are translated to configuration space in the correlation function.

Much of the non-linear physics is understood within the HMCODE method in the real space power spectrum. Of particular importance is the appearance of a second bump feature in the response generated at smaller scales than the first, primordial bump. The reason for this is a non-linear coupling of the bump and one-halo term in the following simple mechanism:

long wave-length density fluctuations are enhanced to form the bump, but at the same time, small-scale fluctuations in regions located inside these overdensities, corresponding to 1-halo regions in halo models, are further amplified and can cross-over the threshold density for collapse more easily, leading to a more efficient halo formation than in a model without a bump. PT, on the other hand successfully follow the data at quasilinear scales, though it fails to model the second, non-linear bump, which is out of its reach. In redshift space this second, non-linear bump is partially erased because of the damping along the line-of-sight direction that is provided by the random motion of virialized regions that generate the "Fingers-of-God". Such effect is more clear in the quadrupole, for which the second bump is almost completely erased, since this multipole gives more weight to the line-of-sight direction. The monopole, on the other hand, still shows the second bump since it gives equal weight to all directions. This redshift-space effect, being highly non-linear, is not captured by perturbation theory, however at quasi-linear scales the simulated data and theory predicted by using the two popular methods of (Taruya et al., 2010) and (Scoccimarro, 2004) behave similarly.

A localized bump in the power spectrum corresponds to oscillations in the correlation function with amplitude proportional to its width and a frequency governed by its position. The effect is to modulate the response about unity: higher wavenumbers at which the bump is located translate to higher oscillation frequencies; and wider bumps enhance the modulation, but are also more rapidly damped. This basic picture is explained well within linear Eulerian theory. By moving to Lagrangian space, we find that the signatures in the correlation function become even more damped since coherent flows have a finite probability to leave overdense regions and populate underdense regions. This effect has the same origin as the smearing of the BAO peak, that is well captured in LPT; and in the bump cosmology is much more evident for large-k located bumps with small widths, since in these cases linear theory shows up rapid oscillations, and the displacement fields sizes, typically given by their standard deviations, are large enough, such that particles find the time to deplete the overpopulated regions.

In the future it would be interesting to investigate the phenomenology of the bump cosmology for different bump amplitudes, which is fixed at 0.15 in this paper, somewhat arbitrarily. One could also investigate more physical examples of 'bump' cosmology, such as that generated by the physical BDE model, where the background expansion is also changed relative to ΛCDM and where the bump shape will not necessarily be Gaussian. Since this was our first investigation, in this paper we focused on modelling statistics of the matter field, which unfortunately are not direct observables. In future, it would be fruitful to consider how the statistics of biased tracers of the density, such as haloes or galaxies, were affected by bump cosmologies. Specifically, we suspect that there may be interesting signatures generated in the halo bias and that these could be understood using (Press and Schechter, 1974) arguments in a similar way to how we could explain the generation of the 'second bump' feature in the matter power spectrum. Of course, one could also investigate higher-order statistics, or statistics of transformed versions of the density fields (e.g., Simpson et al., 2011; White, 2016). On the theory side, it may be interesting to see if Effective Field Theory (EFT) (Baumann et al., 2012) could be used to extend the reach of perturbation theory. Compared to SPT, EFT

simply adds a term $-c_s^2 k^2 P_L(k)$ to the power spectrum, with fitted effective speed of sound c_s^2, and this extra freedom may allow for a joint EFT-halo model approach to accurately model the response across all scales.

Summarizing, in this work we have used non-linear methods to study the fingerprints that may be left by cosmological models on which the dark energy suffers phase transitions, and have the potential to be detectable by current and future galaxy surveys.

Chapter6

SUMMARY AND OUTLOOKS

In this thesis we have studied models beyond ΛCDM, which are characterised by a rapidly diluted energy density (RDED) that dilutes at given scale factor a_c and corresponding wave-vector amplitude $k_c = a_c H(a_c)$. This signature is motivated by the recently proposed BDE model of (de la Macorra and Almaraz, 2018) and SEOS (Jaber-Bravo et al., 2020). The background evolution and therefore the cosmological distances such as the comoving angular distance D_A, the angular diameter D_M, the acoustic scale at recombination r_s and the diffusion damping scale r_d are affected by the RDED transition. Also, this RDED leaves distinctive features in the matter and CMB power spectrum. In particular, it generates a bump in the matter power spectrum, more visible once we compare to ΛCDM, due to the linear growth of density field $\delta_m(k)$ has a higher increase rate for larger H in radiation-dominated epoch (c.f. Eq. (3.29)). The increase takes place only for modes $k \geq k_c$ when $\rho_{ex} > 0$ while for mode $k < k_c$ both models have the same expansion rate and the evolution of $\delta_m(k)$ is the same for both cases. The amplitude of the bump is related to the amount of the diluted energy density ρ_{ex}, while the mode is located about $k \sim k_c$. We study these bumps in the linear regime and also apply one-loop corrections using SPT.

We consider here two different models, one located at large scales, the other at small scales. Both methodologies are inspired by the EDE-like model <. In this EDE-like model, also called BDE model, an RDED phase transition takes place in the radiation dominated epoch with $a_c \sim 10^{-6}$, affecting modes entering the horizon at early times, where the corresponding mode is $k_c \sim 1\,h\text{Mpc}^{-1}$ and a bump is generated for modes $k \geq k_c$. The BDE model also shows a RDED with a steep transition centered at a redshift $z_c \approx 0.625$ resulting in second bump located at large scales.

We also studied models (DMx) with extra matter, diluting in matter dominated epoch, where the growth of structure has two effects. The first one is due to having extra matter ρ_{ex} for $a < a_c$, affecting all modes ($k > k_c$) entering the horizon before a_c, while the second effect is due to the RDED at a_c. We study the increase of amplitude in the linear evolution of the

matter density perturbation of these two different sources, obtaining an increment around 8% in the power spectrum P_X/P_Λ due to the rapid dilution at the maximum of the bump at k_b. Otherwise, we find a plateau for modes $k > k_c$ due to the extra matter, meanwhile for modes entering the horizon after the transition $a < a_c$ we obtain no increase in the evolution of the matter density perturbations and we get $P_X/P_\Lambda = 1$ for modes $k < k_c$.

We concentrated also in a model-independent analysis and we parameterized the dynamics of dark energy using a steep equation of state (SEOS) (Jaber and de la Macorra, 2018) in order to study the imprints of dark energy at late times. In the SEOS model the EoS w has a transition at $z_c = 0.28$. Here we studied two extreme cases, with soft and steep transitions, to observe different impacts on the CMB and matter power spectra.

We used the one-loop correction analysis using the code `MGPT` (Aviles et al., 2018) in order to compute the position and amplitude of the peaks of the bumps in the matter power spectrum, taking into account the background evolutions with and without ρ_{ex}. We find that the non-linear effects shift the peak of the bumps to smaller modes and enhance their amplitudes in comparison to linear computations.

In Table 4.1 and 4.3 are shown different values of cosmological parameters for our two models: for small scales and for large scales, respectively. In the linear regime, we see the bump imprint left by the rapid dilution of BDE on modes $k > k_c$, entering the horizon before a_c, as a peaked bump centered at $k = 0.47\,h\text{Mpc}^{-1}$ for BDE-I,BDE-II,BDE-III ($k = 1.06\,h\text{Mpc}^{-1}$ for BDE-IV,BDE-V, BDE-VI), where the enhancement of power in BDE is about 16% (19.58%), respectively. We notice deviations at larger scales e.g. $k \geq 0.05\,h\text{Mpc}^{-1}$ and $k \geq 0.5\,h\text{Mpc}^{-1}$ respectively, due to the width of the bump in each case. The scale of the bump is mainly located at non-linear scales, although covering also quasi-linear scales, and once we determine the one-loop power spectra we find that BDE-III (BDE-VI) provides an enhancement of 4% (5%) at $k = 0.9\,h\text{Mpc}^{-1}$ ($1.8\,h\text{Mpc}^{-1}$), respectively. Nevertheless, these results should be taken as indicative since the high-k tails of the bumps are out of the reach of perturbation theory.

For late times, the RDED affects the evolution of matter fluctuations mainly at late times during the Einstein-de Sitter phase, matter perturbations have the same amplitude as in ΛCDM at all scales, the overall normalization is due to a slightly different rate of expansion in ΛCDM and SEOS models. Here we studied the same mode $k = 8.37 \times 10^{-5}\,h\text{Mpc}^{-1}$ but different amounts of matter and steepness of the transition.

As time increases, the effect of the dynamical dark energy of the SEOS model is altered decreasing the amplitude for all Fourier modes and originating a bump at $k \approx 5 \times 10^{-3}$; that is, the power spectrum of ΛCDM is always larger than the power spectrum of SEOS model originating a bump at lower redshift.

Summarizing, this distinctive signature, named as bump, has been studied at a linear and one-loop level in perturbation theory. We have theoretically study the evolution of linear matter perturbations and showed that a bump is indeed generated in the matter power spectrum and we estimated the amplitude and width of the bumps in early and late times by means of BDE-like and SEOS-like models. We compared our results with a full implementation

in the numerical Boltzmann code CAMB and found that our theoretical results are within a few percentage difference of the numerical results. This demonstrates that the origin of the bump, observed in matter power spectrum using the numerical simulations, is indeed due to a RDED.

We have also studied non-linear evolution of parametric *bump cosmologies*. In this thesis we have chosen to be as model independent as possible, instead of considering bumps generated by any specific BDE model, since we are interested in a wider range of theoretical models. We fixed the background cosmology to be ΛCDM to allow us to investigate the phenomenology of bumps in isolation. In order to do so, we have run modest-resolution *N*-body simulations, which are complemented by perturbation theory models and non-linear halo-model calculations from the HMCODE model of (Mead et al., 2015). In order to cover over different ranges of scales we work with different methods. This complementary is essential, since although bumps can be localized at a given scale, these are naturally spread by non-linear evolution, typically covering scales that may be outside the range of validity of some particular method.

We expect the different methods used to work over different ranges of scales, and this complementarity is important, since although bumps can be localized at a given scale, these are naturally spread by non-linear evolution, typically covering scales that may be outside the range of validity of some particular method. Bearing in mind that non-linear ΛCDM is well studied, we have put attention to the power spectrum response, constructed as the ratio of the power in a bump cosmology to a cosmology with no bump, instead than on the power spectrum itself. Once an accurate model for the response is at hand, this can be converted into an accurate model for the power spectrum by multiplying by an accurate model for the ΛCDM non-linear power spectrum. We have studied the non-linearities in both real and redshift space for the power spectrum and how these fingerprints are translated to configuration space in the correlation function.

The non-linear physics is well understood within the HMCODE scheme, particularly in the second bump in the response generated at smaller scales than the first, primordial bump. This second bump feature is due to non-linear coupling of the bump and one-halo term in the following mechanism: long wave-length density fluctuations are enhanced to form the bump, but at the same time, small-scale fluctuations in regions located inside these overdensities, corresponding to 1-halo regions in halo models, are further amplified and can cross-over the threshold density for collapse more easily, leading to a more efficient halo formation than in a model without a bump. On the other hand, perturbative scheme successfully follow the data at quasilinear scales, though it fails to model the second, non-linear bump, which is out of its reach. In redshift space this second, non-linear bump is partially erased because of the damping along the line-of-sight direction that is provided by the random motion of virialized regions that generate the "Fingers-of-God". Such effect is more clear in the quadrupole, for which the second bump is almost completely erased, since this multipole gives more weight to the line-of-sight direction. Otherwise, the monopole still shows the second bump since it gives equal weight to all directions. The redshift-space effect, being highly non-linear, is not

captured by perturbation theory, however at quasi-linear scales the simulated data and theory predicted by using the two popular methods of (Taruya et al., 2010) and (Scoccimarro, 2004) behave similarly.

A localized bump in the power spectrum corresponds to oscillations in the correlation function with amplitude proportional to its width and a frequency governed by its position. The effect is to modulate the response about unity: higher wavenumbers at which the bump is located translate to higher oscillation frequencies; and wider bumps enhance the modulation, but are also more rapidly damped. This basic picture is explained well within linear Eulerian theory. By moving to Lagrangian space, we find that the signatures in the correlation function become even more damped since coherent flows have a finite probability to leave overdense regions and populate underdense regions. This effect has the same origin as the smearing of the BAO peak, that is well captured in LPT; and in the bump cosmology is much more evident for large-k located bumps with small widths, since in these cases linear theory shows up rapid oscillations, and the displacement fields sizes, typically given by their standard deviations, are large enough, such that particles find the time to deplete the overpopulated regions.

In the future it would be interesting to investigate the phenomenology of the bump cosmology for different bump amplitudes, which is fixed at 0.15 in this paper, somewhat arbitrarily. One could also investigate more physical examples of 'bump' cosmology, such as that generated by the physical BDE model, where the background expansion is also changed relative to ΛCDM and where the bump shape will not necessarily be Gaussian. Since this was our first investigation, in this paper we focused on modelling statistics of the matter field, which unfortunately are not direct observables. In future, it would be fruitful to consider how the statistics of biased tracers of the density, such as haloes or galaxies, were affected by bump cosmologies. Specifically, we suspect that there may be interesting signatures generated in the halo bias and that these could be understood using (Press and Schechter, 1974) arguments in a similar way to how we could explain the generation of the 'second bump' feature in the matter power spectrum. Of course, one could also investigate higher-order statistics, or statistics of transformed versions of the density fields (e.g., Simpson et al., 2011; White, 2016). On the theory side, it may be interesting to see if Effective Field Theory (EFT) (Baumann et al., 2012) could be used to extend the reach of perturbation theory. Compared to SPT, EFT simply adds a term $-c_s^2 k^2 P_L(k)$ to the power spectrum, with fitted effective speed of sound c_s^2, and this extra freedom may allow for a joint EFT-halo model approach to accurately model the response across all scales.

Summarizing, in this work we have used non-linear methods to study the fingerprints that may be left by cosmological models on which the dark energy suffers phase transitions, and have the potential to be detectable by current and future galaxy surveys.

References

Abazajian, K. et al. (2019). CMB-S4 Science Case, Reference Design, and Project Plan.

Abbott, T. M. C., Abdalla, F. B., Alarcon, A., Aleksić, J., Allam, S., Allen, S., Amara, A., Annis, J., Asorey, J., Avila, S., Bacon, D., Balbinot, E., Banerji, M., Banik, N., Barkhouse, W., Baumer, M., Baxter, E., Bechtol, K., Becker, M. R., Benoit-Lévy, A., Benson, B. A., Bernstein, G. M., Bertin, E., Blazek, J., Bridle, S. L., Brooks, D., Brout, D., Buckley-Geer, E., Burke, D. L., Busha, M. T., Campos, A., Capozzi, D., Carnero Rosell, A., Carrasco Kind, M., Carretero, J., Castander, F. J., Cawthon, R., Chang, C., Chen, N., Childress, M., Choi, A., Conselice, C., Crittenden, R., Crocce, M., Cunha, C. E., D'Andrea, C. B., da Costa, L. N., Das, R., Davis, T. M., Davis, C., De Vicente, J., DePoy, D. L., DeRose, J., Desai, S., Diehl, H. T., Dietrich, J. P., Dodelson, S., Doel, P., Drlica-Wagner, A., Eifler, T. F., Elliott, A. E., Elsner, F., Elvin-Poole, J., Estrada, J., Evrard, A. E., Fang, Y., Fernandez, E., Ferté, A., Finley, D. A., Flaugher, B., Fosalba, P., Friedrich, O., Frieman, J., García-Bellido, J., Garcia-Fernandez, M., Gatti, M., Gaztanaga, E., Gerdes, D. W., Giannantonio, T., Gill, M. S. S., Glazebrook, K., Goldstein, D. A., Gruen, D., Gruendl, R. A., Gschwend, J., Gutierrez, G., Hamilton, S., Hartley, W. G., Hinton, S. R., Honscheid, K., Hoyle, B., Huterer, D., Jain, B., James, D. J., Jarvis, M., Jeltema, T., Johnson, M. D., Johnson, M. W. G., Kacprzak, T., Kent, S., Kim, A. G., King, A., Kirk, D., Kokron, N., Kovacs, A., Krause, E., Krawiec, C., Kremin, A., Kuehn, K., Kuhlmann, S., Kuropatkin, N., Lacasa, F., Lahav, O., Li, T. S., Liddle, A. R., Lidman, C., Lima, M., Lin, H., MacCrann, N., Maia, M. A. G., Makler, M., Manera, M., March, M., Marshall, J. L., Martini, P., McMahon, R. G., Melchior, P., Menanteau, F., Miquel, R., Miranda, V., Mudd, D., Muir, J., Möller, A., Neilsen, E., Nichol, R. C., Nord, B., Nugent, P., Ogando, R. L. C., Palmese, A., Peacock, J., Peiris, H. V., Peoples, J., Percival, W. J., Petravick, D., Plazas, A. A., Porredon, A., Prat, J., Pujol, A., Rau, M. M., Refregier, A., Ricker, P. M., Roe, N., Rollins, R. P., Romer, A. K., Roodman, A., Rosenfeld, R., Ross, A. J., Rozo, E., Rykoff, E. S., Sako, M., Salvador, A. I., Samuroff, S., Sánchez, C., Sanchez, E., Santiago, B., Scarpine, V., Schindler, R., Scolnic, D., Secco, L. F., Serrano, S., Sevilla-Noarbe, I., Sheldon, E., Smith, R. C., Smith, M., Smith, J., Soares-Santos, M., Sobreira, F., Suchyta, E., Tarle, G., Thomas, D., Troxel, M. A., Tucker, D. L., Tucker, B. E., Uddin, S. A., Varga, T. N., Vielzeuf, P., Vikram, V., Vivas, A. K., Walker, A. R., Wang, M., Wechsler, R. H., Weller, J., Wester, W., Wolf, R. C., Yanny, B., Yuan, F., Zenteno, A., Zhang, B., Zhang, Y., Zuntz,

J., and Dark Energy Survey Collaboration (2018). Dark Energy Survey year 1 results: Cosmological constraints from galaxy clustering and weak lensing. , 98(4):043526.

Acquaviva, V., Hajian, A., Spergel, D. N., and Das, S. (2008). Next Generation Redshift Surveys and the Origin of Cosmic Acceleration. *Phys. Rev.*, D78:043514.

Ade, P. et al. (2019). The Simons Observatory: Science goals and forecasts. *JCAP*, 02:056.

Alam, S. et al. (2016). The clustering of galaxies in the completed SDSS-III Baryon Oscillation Spectroscopic Survey: cosmological analysis of the DR12 galaxy sample. *Submitted to: Mon. Not. Roy. Astron. Soc.*

Alam, S. et al. (2020). The Completed SDSS-IV extended Baryon Oscillation Spectroscopic Survey: Cosmological Implications from two Decades of Spectroscopic Surveys at the Apache Point observatory.

Almaraz, E. and de la Macorra, A. (2019). Bound dark energy: Towards understanding the nature of dark energy. *Phys. Rev.*, D99(10):103504.

Almaraz, E., Li, B., and de la Macorra, A. (2020). Nonlinear structure formation in Bound Dark Energy. *JCAP*, 03:016.

Alonso, D. (2013). Cute solutions for two-point correlation functions from large cosmological datasets.

Anderson, L. et al. (2014). The clustering of galaxies in the SDSS-III Baryon Oscillation Spectroscopic Survey: Baryon acoustic oscillations in the Data Releases 10 and 11 galaxy samples. *Mon. Not. Roy. Astron. Soc.*, 441(1):24.

Arun, K., Gudennavar, S., and Sivaram, C. (2017). Dark matter, dark energy, and alternate models: A review. *Advances in Space Research*, 60(1):166–186.

Aviles, A. (2016). Dark matter dispersion tensor in perturbation theory. *Phys. Rev. D*, 93:063517.

Aviles, A. and Cervantes-Cota, J. L. (2017). Lagrangian perturbation theory for modified gravity. *Phys. Rev.*, D96(12):123526.

Aviles, A., Rodriguez-Meza, M. A., De-Santiago, J., and Cervantes-Cota, J. L. (2018). Nonlinear evolution of initially biased tracers in modified gravity. *JCAP*, 11:013.

Baldauf, T., Mirbabayi, M., Simonović, M., and Zaldarriaga, M. (2015). Equivalence principle and the baryon acoustic peak. *Physical Review D*, 92(4).

Barnes, J. and Hut, P. (1986). A hierarchical O(N log N) force-calculation algorithm. , 324(6096):446–449.

Bassett, B. A. and Hlozek, R. (2009). Baryon Acoustic Oscillations.

Baugh, C. (2000). Correlation Function and Power Spectra in Cosmology. page 2136.

Baumann, D., Nicolis, A., Senatore, L., and Zaldarriaga, M. (2012). Cosmological Non-Linearities as an Effective Fluid. *JCAP*, 07:051.

Bernardeau, F., Colombi, S., Gaztanaga, E., and Scoccimarro, R. (2002a). Large scale structure of the universe and cosmological perturbation theory. *Phys. Rept.*, 367:1–248.

Bernardeau, F., Colombi, S., Gaztañaga, E., and Scoccimarro, R. (2002b). Large-scale structure of the universe and cosmological perturbation theory. *Physics Reports*, 367(1-3):1–248.

Berti, E., Barausse, E., Cardoso, V., Gualtieri, L., Pani, P., Sperhake, U., Stein, L. C., Wex, N., Yagi, K., Baker, T., Burgess, C. P., Coelho, F. S., Doneva, D., Felice, A. D., Ferreira, P. G., Freire, P. C. C., Healy, J., Herdeiro, C., Horbatsch, M., Kleihaus, B., Klein, A., Kokkotas, K., Kunz, J., Laguna, P., Lang, R. N., Li, T. G. F., Littenberg, T., Matas, A., Mirshekari, S., Okawa, H., Radu, E., O'Shaughnessy, R., Sathyaprakash, B. S., Broeck, C. V. D., Winther, H. A., Witek, H., Aghili, M. E., Alsing, J., Bolen, B., Bombelli, L., Caudill, S., Chen, L., Degollado, J. C., Fujita, R., Gao, C., Gerosa, D., Kamali, S., Silva, H. O., Rosa, J. G., Sadeghian, L., Sampaio, M., Sotani, H., and Zilhao, M. (2015). Testing general relativity with present and future astrophysical observations. *Classical and Quantum Gravity*, 32(24):243001.

Bond, J. R., Kofman, L., and Pogosyan, D. (1996). How filaments are woven into the cosmic web. *Nature*, 380:603–606.

Brax, P. (2017). What makes the universe accelerate? a review on what dark energy could be and how to test it. *Reports on Progress in Physics*, 81(1):016902.

Bullock, J. S., Kolatt, T. S., Sigad, Y., Somerville, R. S., Kravtsov, A. V., Klypin, A. A., Primack, J. R., and Dekel, A. (2001). Profiles of dark haloes: evolution, scatter and environment. *Monthly Notices of the Royal Astronomical Society*, 321(3):559–575.

Calabrese, E., de Putter, R., Huterer, D., Linder, E. V., and Melchiorri, A. (2011). Future CMB Constraints on Early, Cold, or Stressed Dark Energy. *Phys. Rev. D*, 83:023011.

Carlson, J., Reid, B., and White, M. (2012a). Convolution Lagrangian perturbation theory for biased tracers. *Monthly Notices of the Royal Astronomical Society*, 429(2):1674–1685.

Carlson, J., Reid, B., and White, M. (2012b). Convolution lagrangian perturbation theory for biased tracers. *Monthly Notices of the Royal Astronomical Society*, 429(2):1674–1685.

Casarini, L., Bonometto, S. A., Tessarotto, E., and Corasaniti, P.-S. (2016). Extending the Coyote emulator to dark energy models with standard w_0-w_a parametrization of the equation of state. , 8:008.

Cataneo, M., Emberson, J. D., Inman, D., Harnois-Déraps, J., and Heymans, C. (2020). On the road to per cent accuracy - III. Non-linear reaction of the matter power spectrum to massive neutrinos. , 491(3):3101–3107.

Cataneo, M., Lombriser, L., Heymans, C., Mead, A. J., Barreira, A., Bose, S., and Li, B. (2019). On the road to percent accuracy: non-linear reaction of the matter power spectrum to dark energy and modified gravity. , 488(2):2121–2142.

Chevallier, M. and Polarski, D. (2001). Accelerating universes with scaling dark matter. *Int. J. Mod. Phys.*, D10:213–224.

Collaboration, D. (2016). The DESI Experiment Part I: Science,Targeting, and Survey Design.

Collaboration, E. (2013). Cosmology and fundamental physics with the Euclid satellite. *Living Rev. Rel.*, 16:6.

Collaboration, J.-P. (2014). J-PAS: The Javalambre-Physics of the Accelerated Universe Astrophysical Survey.

collaboration, S. (2020). The 16th Data Release of the Sloan Digital Sky Surveys: First Release from the APOGEE-2 Southern Survey and Full Release of eBOSS Spectra. , 249(1):3.

Cooray, A. and Sheth, R. (2002). Halo models of large scale structure. *Physics Reports*, 372(1):1–129.

Copeland, E. J., Sami, M., and Tsujikawa, S. (2006). Dynamics of dark energy. *Int. J. Mod. Phys.*, D15:1753–1936.

Crocce, M., Pueblas, S., and Scoccimarro, R. (2006). Transients from initial conditions in cosmological simulations. *Monthly Notices of the Royal Astronomical Society*, 373(1):369–381.

Crocce, M. and Scoccimarro, R. (2006). Memory of initial conditions in gravitational clustering. *Phys. Rev. D*, 73:063520.

De la Macorra, A. (2003). Quintessence unification models from nonAbelian gauge dynamics. *JHEP*, 01:033.

de la Macorra, A. (2005). A Realistic particle physics dark energy model. *Phys. Rev. D*, 72:043508.

de la Macorra, A. and Almaraz, E. (2018). Theoretical and Observational Constraints of Bound Dark Energy with Precision Cosmological Data. *Phys. Rev. Lett.*, 121(16):161303.

de la Macorra, A., Gomez-Navarro, D. V., Mastache, J., Aviles, A., Jaber, M., and Almaraz, E. (2021). Cosmological signatures of a rapid diluted energy density. *Phys. Rev. D*, 104:023529.

de la Macorra, A. and Piccinelli, G. (2000). General scalar fields as quintessence. *Phys. Rev. D*, 61:123503.

de la Macorra, A. and Stephan-Otto, C. (2002). Quintessence restrictions on negative power and condensate potentials. *Phys. Rev. D*, 65:083520.

Dekker, A., Ando, S., Correa, C. A., and Ng, K. C. Y. (2021). Warm Dark Matter Constraints Using Milky-Way Satellite Observations and Subhalo Evolution Modeling.

Di Valentino, E., Melchiorri, A., and Silk, J. (2019). Planck evidence for a closed universe and a possible crisis for cosmology. *Nature Astronomy*, 4(2):196–203.

Dodelson, S., Heitmann, K., Hirata, C., Honscheid, K., Roodman, A., Seljak, U., Slosar, A., and Trodden, M. (2016). Cosmic Visions Dark Energy: Science.

Einasto, J., Hutsi, G., Saar, E., Suhhonenko, I., Liivamagi, L. J., Einasto, M., Muller, V., Tago, A. A. S. E., and Tempel, E. (2011). Wavelet analysis of the formation of the cosmic web. *Astron. Astrophys.*, 531:A75.

Eisenstein, D. J. et al. (2005). Detection of the Baryon Acoustic Peak in the Large-Scale Correlation Function of SDSS Luminous Red Galaxies. *Astrophys. J.*, 633:560–574.

Falk, T., Rangarajan, R., and Srednicki, M. (1993). The Angular Dependence of the Three-Point Correlation Function of the Cosmic Microwave Background Radiation as Predicted by Inflationary Cosmologies. , 403:L1.

Frusciante, N. and Perenon, L. (2020). Effective field theory of dark energy: A review. *Physics Reports*, 857:1–63. Effective field theory of dark energy: A review.

Gil-Marín, H., Percival, W. J., Verde, L., Brownstein, J. R., Chuang, C.-H., Kitaura, F.-S., Rodríguez-Torres, S. A., and Olmstead, M. D. (2017). The clustering of galaxies in the SDSS-III Baryon Oscillation Spectroscopic Survey: RSD measurement from the power spectrum and bispectrum of the DR12 BOSS galaxies. *Mon. Not. Roy. Astron. Soc.*, 465(2):1757–1788.

Gomez-Navarro, D. V., Mead, A. J., Aviles, A., and de la Macorra, A. (2020). Impact of cosmological signatures in two-point statistics beyond the linear regime. *Monthly Notices of the Royal Astronomical Society*, 504(3):3284–3297.

Grossi, M. and Springel, V. (2009). The impact of early dark energy on non-linear structure formation. *Monthly Notices of the Royal Astronomical Society*, 394(3):1559–1574.

Gunn, J. E. and Gott, III, J. R. (1972). On the Infall of Matter into Clusters of Galaxies and Some Effects on Their Evolution. *Astrophys. J.*, 176:1–19.

Guth, A. H. (1981). Inflationary universe: A possible solution to the horizon and flatness problems. *Phys. Rev. D*, 23:347–356.

Guth, A. H., Kaiser, D. I., and Nomura, Y. (2014). Inflationary paradigm after planck 2013. *Physics Letters B*, 733:112 – 119.

Hahn, O. and Abel, T. (2011). Multi-scale initial conditions for cosmological simulations. *Monthly Notices of the Royal Astronomical Society*, 415(3):2101–2121.

Hand, N., Feng, Y., Beutler, F., Li, Y., Modi, C., Seljak, U., and Slepian, Z. (2018). nbodykit: an open-source, massively parallel toolkit for large-scale structure. *Astron. J.*, 156(4):160.

Heymans, C., Tröster, T., Asgari, M., Blake, C., Hildebrandt, H., Joachimi, B., Kuijken, K., Lin, C.-A., Sánchez, A. G., van den Busch, J. L., Wright, A. H., Amon, A., Bilicki, M., de Jong, J., Crocce, M., Dvornik, A., Erben, T., Getman, F., Giblin, B., Glazebrook, K., Hoekstra, H., Joudaki, S., Kannawadi, A., Lidman, C., Köhlinger, F., Miller, L., Napolitano, N. R., Parkinson, D., Schneider, P., Shan, H., and Wolf, C. (2020). KiDS-1000 Cosmology: Multi-probe weak gravitational lensing and spectroscopic galaxy clustering constraints. *arXiv e-prints*, page arXiv:2007.15632.

Hikage, C., Oguri, M., Hamana, T., More, S., Mandelbaum, R., Takada, M., Köhlinger, F., Miyatake, H., Nishizawa, A. J., Aihara, H., Armstrong, R., Bosch, J., Coupon, J., Ducout, A., Ho, P., Hsieh, B.-C., Komiyama, Y., Lanusse, F., Leauthaud, A., Lupton, R. H., Medezinski, E., Mineo, S., Miyama, S., Miyazaki, S., Murata, R., Murayama, H., Shirasaki, M., Sifón, C., Simet, M., Speagle, J., Spergel, D. N., Strauss, M. A., Sugiyama, N., Tanaka, M., Utsumi, Y., Wang, S.-Y., and Yamada, Y. (2019). Cosmology from cosmic shear power spectra with Subaru Hyper Suprime-Cam first-year data. , 71(2):43.

Hou, Z., Keisler, R., Knox, L., Millea, M., and Reichardt, C. (2013). How Massless Neutrinos Affect the Cosmic Microwave Background Damping Tail. *Phys. Rev. D*, 87:083008.

Hu, W., Scott, D., Sugiyama, N., and White, M. J. (1995). The Effect of physical assumptions on the calculation of microwave background anisotropies. *Phys. Rev. D*, 52:5498–5515.

Hunt, P. and Sarkar, S. (2009). Constraints on large-scale inhomogeneities from WMAP5 and SDSS: confrontation with recent observations. *Monthly Notices of the Royal Astronomical Society*, 401(1):547–558.

Huterer, D. and Shafer, D. L. (2017). Dark energy two decades after: observables, probes, consistency tests. *Reports on Progress in Physics*, 81(1):016901.

Ishak, M. (2018). Testing general relativity in cosmology. *Living Reviews in Relativity*, 22(1).

Jaber, M. and de la Macorra, A. (2018). Probing a Steep EoS for Dark Energy with latest observations. *Astropart. Phys.*, 97:130–135.

Jaber-Bravo, M., Almaraz, E., and de la Macorra, A. (2020). Imprint of a Steep Equation of State in the growth of structure. *Astropart. Phys.*, 115:102388.

Jing, Y. P. (2005). Correcting for the alias effect when measuring the power spectrum using a fast fourier transform. *The Astrophysical Journal*, 620(2):559–563.

Kaiser, N. (1987). Clustering in real space and in redshift space. *Monthly Notices of the Royal Astronomical Society*, 227(1):1–21.

Koyama, K. (2016). Cosmological tests of modified gravity. *Reports on Progress in Physics*, 79(4):046902.

Kuhlen, M., Vogelsberger, M., and Angulo, R. (2012). Numerical Simulations of the Dark Universe: State of the Art and the Next Decade. *Phys. Dark Univ.*, 1:50–93.

Landau, L. D., . L. E. M. (1959). *Fluid mechanics*. Pergamon press edition.

Lawrence, E., Heitmann, K., Kwan, J., Upadhye, A., Bingham, D., Habib, S., Higdon, D., Pope, A., Finkel, H., and Frontiere, N. (2017). The Mira-Titan Universe. II. Matter Power Spectrum Emulation. , 847:50.

Lawrence, E., Heitmann, K., White, M., Higdon, D., Wagner, C., Habib, S., and Williams, B. (2010). The Coyote Universe. III. Simulation Suite and Precision Emulator for the Nonlinear Matter Power Spectrum. , 713:1322–1331.

Lewis, A., Challinor, A., and Lasenby, A. (2000). Efficient computation of CMB anisotropies in closed FRW models. , 538:473–476.

Linder, E. V. (2003). Exploring the expansion history of the universe. *Phys. Rev. Lett.*, 90:091301.

Linder, E. V. (2019). Developments in Cosmic Growth and Gravitation.

Linder, E. V. (2021). The rise of dark energy.

Ma, C.-P. and Bertschinger, E. (1995). Cosmological perturbation theory in the synchronous and conformal Newtonian gauges. *Astrophys. J.*, 455:7–25.

Maldacena, J. (2003). Non-gaussian features of primordial fluctuations in single field inflationary models. *Journal of High Energy Physics*, 2003(05):013–013.

Martinelli, M. and Casas, S. (2021). Cosmological tests of gravity: A future perspective. *Universe*, 7(12).

Matsubara, T. (2008a). Nonlinear perturbation theory with halo bias and redshift-space distortions via the lagrangian picture. *Phys. Rev. D*, 78:083519.

Matsubara, T. (2008b). Resumming Cosmological Perturbations via the Lagrangian Picture: One-loop Results in Real Space and in Redshift Space. *Phys. Rev.*, D77:063530.

Matsubara, T. (2015). Recursive Solutions of Lagrangian Perturbation Theory. *Phys. Rev.*, D92(2):023534.

McDonald, P. and Roy, A. (2009). Clustering of dark matter tracers: generalizing bias for the coming era of precision LSS. *Journal of Cosmology and Astroparticle Physics*, 2009(08):020–020.

Mead, A., Brieden, S., Tröster, T., and Heymans, C. (2020). HMcode-2020: Improved modelling of non-linear cosmological power spectra with baryonic feedback. *arXiv e-prints*, page arXiv:2009.01858.

Mead, A. J. (2017). Spherical collapse, formation hysteresis and the deeply non-linear cosmological power spectrum. , 464:1282–1293.

Mead, A. J., Heymans, C., Lombriser, L., Peacock, J. A., Steele, O. I., and Winther, H. A. (2016). Accurate halo-model matter power spectra with dark energy, massive neutrinos and modified gravitational forces. , 459:1468–1488.

Mead, A. J., Peacock, J. A., Heymans, C., Joudaki, S., and Heavens, A. F. (2015). An accurate halo model for fitting non-linear cosmological power spectra and baryonic feedback models. , 454:1958–1975.

Mead, A. J., Tröster, T., Heymans, C., Van Waerbeke, L., and McCarthy, I. G. (2020). A hydrodynamical halo model for weak-lensing cross correlations. *arXiv e-prints*, page arXiv:2005.00009.

Menegoni, E., Archidiacono, M., Calabrese, E., Galli, S., Martins, C., and Melchiorri, A. (2012). The Fine Structure Constant and the CMB Damping Scale. *Phys. Rev. D*, 85:107301.

Mohammed, I. and Seljak, U. (2014). Analytic model for the matter power spectrum, its covariance matrix, and baryonic effects. *Mon. Not. Roy. Astron. Soc.*, 445(4):3382–3400.

Mohammed, I. and Seljak, U. (2014). Analytic model for the matter power spectrum, its covariance matrix and baryonic effects. , 445(4):3382–3400.

Mukherjee, S., Wandelt, B. D., and Silk, J. (2021). Testing the general theory of relativity using gravitational wave propagation from dark standard sirens. *Monthly Notices of the Royal Astronomical Society*, 502(1):1136–1144.

Nakamura, T. T. and Suto, Y. (1997). Strong Gravitational Lensing and Velocity Function as Tools to Probe Cosmological Parameters: Current Constraints and Future Predictions. *Progress of Theoretical Physics*, 97(1):49–81.

Navarro, J. F., Frenk, C. S., and White, S. D. M. (1997). A universal density profile from hierarchical clustering. *The Astrophysical Journal*, 490(2):493–508.

Peacock, J. A. et al. (2001). A Measurement of the cosmological mass density from clustering in the 2dF Galaxy Redshift Survey. *Nature*, 410:169–173.

Peacock, J. A. and Smith, R. E. (2000). Halo occupation numbers and galaxy bias. , 318:1144–1156.

Peebles, P. J. E. (1980). *The large-scale structure of the universe*.

Percival, W. J., Baugh, C. M., Bland-Hawthorn, J., Bridges, T., Cannon, R., Cole, S., Colless, M., Collins, C., Couch, W., Dalton, G., De Propris, R., Driver, S. P., Efstathiou, G., Ellis, R. S., Frenk, C. S., Glazebrook, K., Jackson, C., Lahav, O., Lewis, I., Lumsden, S., Maddox, S., Moody, S., Norberg, P., Peacock, J. A., Peterson, B. A., Sutherland, W., and Taylor, K. (2001). The 2dF Galaxy Redshift Survey: the power spectrum and the matter content of the Universe. *Monthly Notices of the Royal Astronomical Society*, 327(4):1297–1306.

Percival, W. J. and White, M. (2009). Testing cosmological structure formation using redshift-space distortions. *Monthly Notices of the Royal Astronomical Society*, 393(1):297–308.

Perlmutter, S. et al. (1999). Measurements of Omega and Lambda from 42 high redshift supernovae. *Astrophys. J.*, 517:565–586.

Persic, M., Salucci, P., and Stel, F. (1996). The universal rotation curve of spiral galaxies — I. The dark matter connection. *Monthly Notices of the Royal Astronomical Society*, 281(1):27–47.

Philcox, O. H., Spergel, D. N., and Villaescusa-Navarro, F. (2020). Effective halo model: Creating a physical and accurate model of the matter power spectrum and cluster counts. *Phys. Rev. D*, 101(12):123520.

Piña, P. E. M., Fraternali, F., Oosterloo, T., Adams, E. A. K., Oman, K. A., and Leisman, L. (2021). No need for dark matter: resolved kinematics of the ultra-diffuse galaxy AGC 114905. *Monthly Notices of the Royal Astronomical Society*. stab3491.

Planck Collaboration (2018a). Planck 2018 results. VI. Cosmological parameters. *arXiv e-prints*, page arXiv:1807.06209.

Planck Collaboration (2018b). Planck 2018 results. VI. Cosmological parameters. *arXiv e-prints*, page arXiv:1807.06209.

Planck Collaboration, Ade, P. A. R., Aghanim, N., Arnaud, M., Ashdown, M., Aumont, J., Baccigalupi, C., Banday, A. J., Barreiro, R. B., Bartlett, J. G., Bartolo, N., Battaner, E., Battye, R., Benabed, K., Benoît, A., Benoit-Lévy, A., Bernard, J.-P., Bersanelli, M., Bielewicz, P., Bock, J. J., Bonaldi, A., Bonavera, L., Bond, J. R., Borrill, J., Bouchet, F. R., Boulanger, F., Bucher, M., Burigana, C., Butler, R. C., Calabrese, E., Cardoso, J.-F., Catalano, A., Challinor, A., Chamballu, A., Chary, R.-R., Chiang, H. C., Chluba, J., Christensen, P. R., Church, S., Clements, D. L., Colombi, S., Colombo, L. P. L., Combet, C., Coulais, A., Crill, B. P., Curto, A., Cuttaia, F., Danese, L., Davies, R. D., Davis, R. J., de Bernardis, P., de Rosa, A., de Zotti, G., Delabrouille, J., Désert, F.-X., Di Valentino, E., Dickinson, C., Diego, J. M., Dolag, K., Dole, H., Donzelli, S., Doré, O., Douspis, M., Ducout, A., Dunkley, J., Dupac, X., Efstathiou, G., Elsner, F., Enßlin, T. A., Eriksen, H. K., Farhang, M., Fergusson, J., Finelli, F., Forni, O., Frailis, M., Fraisse, A. A., Franceschi, E., Frejsel, A., Galeotta, S., Galli, S., Ganga, K., Gauthier, C., Gerbino, M., Ghosh, T., Giard, M., Giraud-Héraud, Y., Giusarma, E., Gjerløw, E., González-Nuevo, J., Górski, K. M., Gratton, S., Gregorio, A., Gruppuso, A., Gudmundsson, J. E., Hamann, J., Hansen, F. K., Hanson, D., Harrison, D. L., Helou, G., Henrot-Versillé, S., Hernández-Monteagudo, C., Herranz, D., Hildebrandt, S. R., Hivon, E., Hobson, M., Holmes, W. A., Hornstrup, A., Hovest, W., Huang, Z., Huffenberger, K. M., Hurier, G., Jaffe, A. H., Jaffe, T. R., Jones, W. C., Juvela, M., Keihänen, E., Keskitalo, R., Kisner, T. S., Kneissl, R., Knoche, J., Knox, L., Kunz, M., Kurki-Suonio, H., Lagache, G., Lähteenmäki, A., Lamarre, J.-M., Lasenby, A., Lattanzi, M., Lawrence, C. R., Leahy, J. P., Leonardi, R., Lesgourgues, J., Levrier, F., Lewis, A., Liguori, M., Lilje, P. B., Linden-Vørnle, M., López-Caniego, M., Lubin, P. M., Macías-Pérez, J. F., Maggio, G., Maino, D., Mandolesi, N., Mangilli, A., Marchini, A., Maris, M., Martin, P. G., Martinelli, M., Martínez-González, E., Masi, S., Matarrese, S., McGehee, P., Meinhold, P. R., Melchiorri, A., Melin, J.-B., Mendes, L., Mennella, A., Migliaccio, M., Millea, M., Mitra, S., Miville-Deschênes, M.-A., Moneti, A., Montier, L., Morgante, G., Mortlock, D., Moss, A., Munshi, D., Murphy, J. A., Naselsky, P., Nati, F., Natoli, P., Netterfield, C. B., Nørgaard-Nielsen, H. U., Noviello, F., Novikov, D., Novikov, I., Oxborrow, C. A., Paci, F., Pagano, L., Pajot, F., Paladini, R., Paoletti, D., Partridge, B., Pasian, F., Patanchon, G., Pearson, T. J., Perdereau, O., Perotto, L., Perrotta, F., Pettorino, V., Piacentini, F., Piat, M., Pierpaoli, E., Pietrobon, D., Plaszczynski, S., Pointecouteau, E., Polenta, G., Popa, L., Pratt, G. W., Prézeau, G., Prunet, S., Puget, J.-L., Rachen, J.

P., Reach, W. T., Rebolo, R., Reinecke, M., Remazeilles, M., Renault, C., Renzi, A., Ristorcelli, I., Rocha, G., Rosset, C., Rossetti, M., Roudier, G., Rouillé d´Orfeuil, B., Rowan-Robinson, M., Rubiño-Martín, J. A., Rusholme, B., Said, N., Salvatelli, V., Salvati, L., Sandri, M., Santos, D., Savelainen, M., Savini, G., Scott, D., Seiffert, M. D., Serra, P., Shellard, E. P. S., Spencer, L. D., Spinelli, M., Stolyarov, V., Stompor, R., Sudiwala, R., Sunyaev, R., Sutton, D., Suur-Uski, A.-S., Sygnet, J.-F., Tauber, J. A., Terenzi, L., Toffolatti, L., Tomasi, M., Tristram, M., Trombetti, T., Tucci, M., Tuovinen, J., Türler, M., Umana, G., Valenziano, L., Valiviita, J., Van Tent, F., Vielva, P., Villa, F., Wade, L. A., Wandelt, B. D., Wehus, I. K., White, M., White, S. D. M., Wilkinson, A., Yvon, D., Zacchei, A., and Zonca, A. (2016). Planck 2015 results - xiii. cosmological parameters. *A&A*, 594:A13.

Pogosian, L., Corasaniti, P. S., Stephan-Otto, C., Crittenden, R., and Nichol, R. (2005). Tracking dark energy with the ISW effect: Short and long-term predictions. *Phys. Rev. D*, 72:103519.

Press, W. H. and Schechter, P. (1974). Formation of Galaxies and Clusters of Galaxies by Self-Similar Gravitational Condensation. , 187:425–438.

Press, W. H. and Schechter, P. (1974). Formation of Galaxies and Clusters of Galaxies by Self-Similar Gravitational Condensation. , 187:425.

Psaltis, D. (2008). Probes and Tests of Strong-Field Gravity with Observations in the Electromagnetic Spectrum. *Living Rev. Rel.*, 11:9.

Psaltis, D. (2019). Testing general relativity with the event horizon telescope. *General Relativity and Gravitation*, 51(10).

Raccanelli, A., Bertacca, D., Pietrobon, D., Schmidt, F., Samushia, L., Bartolo, N., Doré, O., Matarrese, S., and Percival, W. J. (2013). Testing gravity using large-scale redshift-space distortions. *Monthly Notices of the Royal Astronomical Society*, 436(1):89–100.

Rampf, C. and Buchert, T. (2012). Lagrangian perturbations and the matter bispectrum i: fourth-order model for non-linear clustering. *Journal of Cosmology and Astroparticle Physics*, 2012(06):021–021.

Riess, A. G. et al. (1998). Observational evidence from supernovae for an accelerating universe and a cosmological constant. *Astron. J.*, 116:1009–1038.

Schutz, B. F. (2009). *A first course in general relativity*. New york, cambridge university press edition.

Scoccimarro, R. (2004). Redshift-space distortions, pairwise velocities and nonlinearities. *Phys. Rev. D*, 70:083007.

Scolnic, D. et al. (2018). The Complete Light-curve Sample of Spectroscopically Confirmed SNe Ia from Pan-STARRS1 and Cosmological Constraints from the Combined Pantheon Sample. *Astrophys. J.*, 859(2):101.

Sefusatti, E., Crocce, M., Scoccimarro, R., and Couchman, H. M. P. (2016). Accurate estimators of correlation functions in fourier space. *Monthly Notices of the Royal Astronomical Society*, 460(4):3624–3636.

Seljak, U. (2000). Analytic model for galaxy and dark matter clustering. , 318:203–213.

Seljak, U. and Vlah, Z. (2015). Halo Zel'dovich model and perturbation theory: Dark matter power spectrum and correlation function. , 91(12):123516.

Seljak, U. and Vlah, Z. (2015). Halo Zel'dovich model and perturbation theory: Dark matter power spectrum and correlation function. *Phys. Rev.*, D91(12):123516.

Sheth, R. K., Mo, H. J., and Tormen, G. (2001). Ellipsoidal collapse and an improved model for the number and spatial distribution of dark matter haloes. *Monthly Notices of the Royal Astronomical Society*, 323(1):1–12.

Simpson, F., James, J. B., Heavens, A. F., and Heymans, C. (2011). Clipping the Cosmos: The Bias and Bispectrum of Large Scale Structure. , 107(27):271301.

Smith, R. E., Peacock, J. A., Jenkins, A., White, S. D. M., Frenk, C. S., Pearce, F. R., Thomas, P. A., Efstathiou, G., and Couchman, H. M. P. (2003). Stable clustering, the halo model and non-linear cosmological power spectra. , 341:1311–1332.

Smith, R. E., Scoccimarro, R., and Sheth, R. K. (2007). Scale dependence of halo and galaxy bias: Effects in real space. , 75(6):063512.

Spergel, D. et al. (2015). Wide-Field InfrarRed Survey Telescope-Astrophysics Focused Telescope Assets WFIRST-AFTA 2015 Report.

Springel, V. (2005). The cosmological simulation code GADGET-2. , 364:1105–1134.

Springel, V., White, S., Jenkins, A., Frenk, C., Yoshida, N., Gao, L., Navarro, J., Thacker, R., Croton, D., Helly, J., Peacock, J., Cole, S., Thomas, P., Couchman, H., Evrard, A., Colberg, J., and Pearce, F. (2005). Simulations of the formation, evolution and clustering of galaxies and quasars. *Nature*, 435.

Steinhardt, P. J., Wang, L.-M., and Zlatev, I. (1999). Cosmological tracking solutions. *Phys. Rev. D*, 59:123504.

Sugiyama, N. S. (2014). Using Lagrangian perturbation theory for precision cosmology. *Astrophys. J.*, 788:63.

Takahashi, R., Sato, M., Nishimichi, T., Taruya, A., and Oguri, M. (2012). Revising the Halofit Model for the Nonlinear Matter Power Spectrum. , 761:152.

Taruya, A., Nishimichi, T., and Saito, S. (2010). Baryon Acoustic Oscillations in 2D: Modeling Redshift-space Power Spectrum from Perturbation Theory. *Phys. Rev. D*, 82:063522.

Tassev, S. (2014a). Lagrangian or Eulerian; Real or Fourier? Not All Approaches to Large-Scale Structure Are Created Equal. *JCAP*, 06:008.

Tassev, S. (2014b). N-point Statistics of Large-Scale Structure in the Zel'dovich Approximation. *JCAP*, 1406:012.

Tassev, S. and Zaldarriaga, M. (2012). The mildly non-linear regime of structure formation. *Journal of Cosmology and Astroparticle Physics*, 2012(04):013–013.

Taylor, A. N. and Hamilton, A. J. S. (1996). Non-linear cosmological power spectra in real and redshift space. *Monthly Notices of the Royal Astronomical Society*, 282(3):767–778.

The Atacama Cosmology Telescope Collaboration (2021). The Atacama Cosmology Telescope: Constraints on Pre-Recombination Early Dark Energy.

Verde, L., Treu, T., and Riess, A. G. (2019). Tensions between the early and late Universe. *Nature Astronomy*, 3:891–895.

Vlah, Z., Castorina, E., and White, M. (2016). The gaussian streaming model and convolution lagrangian effective field theory. *Journal of Cosmology and Astroparticle Physics*, 2016(12):007–007.

Vlah, Z., Seljak, U., and Baldauf, T. (2015a). Lagrangian perturbation theory at one loop order: successes, failures, and improvements. *Phys. Rev.*, D91:023508.

Vlah, Z. and White, M. (2019). Exploring redshift-space distortions in large-scale structure. *JCAP*, 03:007.

Vlah, Z., White, M., and Aviles, A. (2015b). A lagrangian effective field theory. *Journal of Cosmology and Astroparticle Physics*, 2015(09):014–014.

Weinberg, S. (2008). *Cosmology*.

Weltman, A. et al. (2020). Fundamental physics with the Square Kilometre Array. *Publ. Astron. Soc. Austral.*, 37:e002.

White, M. (2016). A marked correlation function for constraining modified gravity models. , 2016(11):057.

Will, C. M. (2014). The confrontation between general relativity and experiment. *Living Reviews in Relativity*, 17(1).

Yu, B., Ferraro, S., Knight, Z. R., Knox, L., and Sherwin, B. D. (2021). The Physical Origin of Dark Energy Constraints from Rubin Observatory and CMB-S4 Lensing Tomography.

Yurin, D. and Springel, V. (2014). An iterative method for the construction of N-body galaxy models in collisionless equilibrium. *Monthly Notices of the Royal Astronomical Society*, 444(1):62–79.

Zel'Dovich, Y. B. (1970). Reprint of 1970A&A.....5...84Z. Gravitational instability: an approximate theory for large density perturbations. , 500:13–18.

Zeldovich, Ya. B. (1970). Gravitational instability: An Approximate theory for large density perturbations. *Astron. Astrophys.*, 5:84–89.

Zhan, H. and Tyson, J. A. (2018). Cosmology with the Large Synoptic Survey Telescope: an Overview. *Rept. Prog. Phys.*, 81(6):066901.

Zlatev, I., Wang, L.-M., and Steinhardt, P. J. (1999). Quintessence, cosmic coincidence, and the cosmological constant. *Phys. Rev. Lett.*, 82:896–899.

Zyla et al. (2020). The Review of Particle Physics (2020). *Prog. Theor. Exp. Phys.*, 083C01.